

An Underwater Surface Pressure Measurement Technique based on Compliant Coatings

Madeline Zhang

Delft University of Technology



An Underwater Surface Pressure Measurement Technique based on Compliant Coatings

MASTER THESIS

by

Madeline (Xiaoxiao) Zhang

Student number: 5217172
Daily supervisors: Dr.ir. AJ Greidanus, Dr. A Laskari
AE supervisor: Dr.ir. BW van Oudheusden
Project Duration: Jan 2022 - Aug 2022
Defense date: August 29, 2022
Specialization: Aerodynamics
Faculty: Faculty of Aerospace Engineering

Acknowledgements

The past 8 months were one of the most challenging times of my life. After sustaining two concussions in the lab due to my clumsiness and struggling with many health issues for months until the end, I am relieved to have completed my master thesis on time.

However, I would not have been able to accomplish this without full financial support from the Justus en Louise van Effen scholarship for the last two years and the ones who made my thesis project a valuable learning experience.

I would like to thank my daily supervisor Arnoud for his advice and empathetic discussions about both work and life and for introducing me to the field of compliant coating which I knew nothing about before. I am thankful to my other daily supervisor Angeliki for her guidance on the research process from the beginning to the end. I would like to thank my aerospace supervisor Bas for providing insightful comments on my written reports.

Many technicians helped with my experimental campaign. I would like to thank Edwin for making sure I have the equipment I need and his expertise on PIV experiments, Jan and Jasper for assisting me with electrical and mechanical manufacturing whenever I needed them, and Bart for fixing things in my new lab unprompted to ensure I have a safer work environment.

As I was new to the faculty of 3me, I was glad I met fellow masters student Kavya and my lab neighbours Luuk and Ilam who made me feel less alone while I was at the faculty. I am beyond grateful to my friends Nadine, Paul, Shibo, Milan, Stavros and Agnieszka for reminding me of who I am and cheering me on when I was not feeling like myself.

Last but not least, I would like to thank my parents for supporting me remotely as they have been for the past seven years, and my boyfriend Philipp for being a constant source of love and support, always staying by my side and helping me carry on in the less brilliant days. I am also grateful to Philipp's parents for caring for me when I was sick in Germany during the week I finalized this thesis.

I look forward to starting my PhD in Amsterdam and continuing my journey in fluid research with what I have learned in the past eight months. So long and thanks for all the fish!

Madeline Zhang

Oberbrüden, Aug 2022

Abstract

Surface pressure measurements are a crucial part of aerodynamic/hydrodynamic analysis and are essential when studying complex flow phenomena. Although pressure-sensitive paint (PSP) has become established as a non-intrusive field measurement technique for high-speed applications in air, a comparable method does not yet exist for usage underwater.

In this exploratory study, a novel compliant coating-based pressure measurement (CCPM) technique is developed and tested using a submerged impinging jet setup. The technique utilizes the compliant coating's ability to deform according to flow perturbations. Although the initial motive for studying the interactions between compliant coatings and turbulent flow is towards reducing drag using the two-way coupling regime where the coating deformation modifies boundary layer properties [1], past studies have shown that a one-way coupling regime exists where the coating has no significant effect on the surrounding flow [2] [3], making it ideal for a non-intrusive measurement technique.

Towards the realization of the new measurement system, free surface synthetic schlieren (FSSS) is used to extract the coating deformation from which the pressure fluctuations on the coating surface are obtained through a pressure-deformation scaling extracted from turbulent boundary layer (TBL) flows by Greidanus [3]. Although the results using the TBL scaling show a linear trend matching the pressure sensor measurements, they overestimate the magnitude of the pressure fluctuations. Therefore, a new scaling factor is proposed which shows a better alignment. In addition, particle image velocimetry (PIV) is used to quantify the impact of coating deformation on the surrounding flow. The effect on the mean and RMS velocity profiles is localized around the region within a 1 mm distance from the impinging plate and is shown to be <5 % at distances more than 1 mm from the coating.

Overall, the CCPM technique is able to extract surface pressure fluctuations from compliant coating deformations induced by a submerged impinging jet. Once fully validated, it has the potential to benefit hydrodynamic flow analysis by serving as a low-cost, high-resolution replacement for pressure sensor arrays as well as an experimental alternative for testing scenarios that currently rely on simulations to obtain surface pressure fields.

Contents

Acknowledgement	i
Abstract	ii
Contents	iii
List of Figures	vi
List of Tables	x
Nomenclature	xi
1 Introduction	1
1.1 Existing surface pressure measurement techniques	1
1.2 Research questions	2
1.3 Research objectives	3
1.4 Thesis outline	4
2 Background	5
2.1 Compliant coatings	5
2.2 Measurement of surface deformation	10
2.2.1 Densitometry	11
2.2.2 Surface measurement	12
3 Experimental design of a CCPM system	19
3.1 Requirements	19
3.2 System overview	20
3.3 Test flow	21
3.4 Compliant coatings	23
3.4.1 Material properties	23
3.4.2 Casting and maintenance	24

3.5	Measurement of coating deformation with FSSS	25
3.5.1	Optics selection and placement	26
3.5.2	Background dot pattern	27
3.5.3	Calibration	28
3.5.4	Image acquisition	29
3.6	FSSS Processing and post processing	30
3.6.1	From dot patterns to displacement field	31
3.6.2	Cleaning up the displacement field	32
3.6.3	From displacement to pressure	34
3.7	FSSS validity	35
3.7.1	Ray crossing	35
3.7.2	Image strain	35
3.7.3	Uncertainties	36
3.7.4	Maximum deformation vs coating thickness	37
3.8	PIV	38
3.9	Pressure sensors	41
4	Results	44
4.1	Effect of jet velocity on coating deformation	44
4.2	Wave characteristics	46
4.2.1	Propagating wavefronts	46
4.2.2	Wavelength and wave amplitude	47
4.2.3	Wave speed	50
4.3	Validation with pressure sensors	51
4.3.1	Resolution	51
4.3.2	Symmetry	52
4.3.3	Scaling	52
4.4	Flow characterization	55
4.4.1	Velocity contours	56
4.4.2	Profiles along jet centreline	57
4.4.3	Radial profiles	60
4.5	Coupling regime	63

5	Conclusions and Recommendations	65
5.1	Conclusions	65
5.2	Future recommendations	66
A	Additional plots and analysis	68
A.1	Additional steps in post-processing	68
A.2	Pressure sensor calibration curves	75
A.3	Frequency analysis	75
	References	79

List of Figures

1.1	A polymer-based PSP setup. From Quinn et al. [5]	2
2.1	Wavelike folds appearing in the compliant skin of a Delphinidae during rapid swimming. From Gad-El-Hak [11]	5
2.2	Static divergence waves under a turbulent boundary layer. From Gad-El-Hak et al. [7]	6
2.3	Response of an incompressible viscoelastic coating, where δ^* is the displacement thickness of the boundary layer, d is the coating thickness and τ_t is the shear relaxation time of the coating. From Duncan 1986 [19].	7
2.4	The measured and modelled vertical surface displacement $\zeta_{c,rms}^+$ as functions of the Reynolds number for three different coatings. From Benschop et al. [8]	8
2.5	<i>a)</i> The measured vertical surface displacement for all three coatings as a function of the normalized stress. <i>b) – d)</i> The measured and modelled point spectra of the vertical surface displacement as functions of the angular frequency in outer units for coating 1,2,3, where the vertical displacement spectra are normalized in outer units $E_{\zeta_{c+}}^o = E_{\zeta_{c+}} U_\infty / \delta_{bl}$. From Benschop et al. [8]	9
2.6	Surface height variation of the three coatings: <i>a)</i> Root-mean-square values as a function of the bulk velocity. <i>b)</i> RMS-values scaled with coating thickness in relation to the pressure fluctuations scaled with coating shear modulus. From Greidanus [3]	10
2.7	A high amplitude wave train first appearing in the instantaneous surface height field at the transitional velocity of 4.5 m/s (left) and more wave trains appearing at a higher velocity of 5.0 m/s (right). From Greidanus [3]	10
2.8	BOS imaging configuration. From Raffel [26]	11
2.9	Location of components of the grating-based optical system. From Kurata et al. [28]	12
2.10	<i>a)</i> 3D ray geometry of an arbitrary surface showing the incidence plane CAM, defined by the dot pattern point M, the camera location C, and the unit normal vector \hat{n} at the point I where the light ray MIC intercepts the interface. <i>b)</i> 2D view of the incidence plane illustrating the ray principle. From Moisy et al. [29]	13
2.11	Apparent dot pattern displacement due to multiple layers of materials with different refractive indices. From Moisy et al. [29]	14
2.12	2D view of the vertical incidence plane showing camera location C, camera-pattern distance h_{cp} and paraxial angle β . From Moisy et al. [29]	15

2.13	Ray crossing phenomenon when h_0 is larger than the focal length EF of the wave crest. In this case, the sequence of points 2'3'4' on the pattern will be seen as reversed, where 2' and 4' have multiple images. From Moisy et al. [29]	15
2.14	FSSS setup for performing surface deformation measurements. From Greidanus [3]	17
2.15	Example image of a deformed dot-pattern (left) and the corresponding computed displacement vector field (arrows) and reconstructed surface height field (colour) (right). From Greidanus [3]	17
2.16	Histogram of the maximum correlation peaks when computing the cross-correlation between the reference undeformed image and the deformed image. The contour plots represent the normalized cross-correlation maps. From Charruault et al. [31]	18
3.1	A sketch of the experimental setup, note that the coating plate is exchangeable with the validation sensor array plate	21
3.2	Configuration of the recirculating water tank setup	22
3.3	Illustration of a turbulent jet. From Cushman-Roisin [33]	23
3.4	Coating casting process showing the solidified coating in a beaker and the melted coating in a polycarbonate plate mould inside the metal tray	24
3.5	Damaged coating surface before and after remelting	25
3.6	Experimental setup for the FSSS experiments	26
3.7	Locations of key components and important dimensions	26
3.8	Example instantaneous displacement fields obtained using the dot patterns in Table 3.3.	28
3.9	FSSS calibration target and its position in the flow facility	29
3.10	Convergence of the horizontal displacement V at a location near the jet impact point	30
3.11	Flow chart of processing and post-processing steps	31
3.12	Surface height fields showing the effect of processing the entire FOV compared to processing the half without jet shadow. The jet shadow is shown in grey	33
3.13	Effect of the LINSUB and MSUB operation on P_{rms} on a vertical line extending from the jet impact point to the bottom edge of the field of view	33
3.14	σ_{rms}^* values of each test case for all snapshots	36
3.15	H_{rms} at jet impact point scaled with coating thickness for all jet velocity cases	38
3.16	PIV setup showing camera and laser sheet positions and key dimensions	39
3.17	PIV u_{rms} convergence with the number of snapshots	40
3.18	PIV w_{rms} convergence with the number of snapshots	41
3.19	Physical locations of the pressure sensors and the locations at which the pressure data was extracted from FSSS, sensors corresponded by colours	42

3.20	Convergence of P_{rms} with the number of samples for all three sensors, plotted in increments of 10 samples	42
3.21	Pressure distribution histograms for the three sensors	43
4.1	Example displacement fields from selected cases of increasing jet velocity	45
4.2	Example instantaneous surface height fields from selected cases of increasing jet velocity.	46
4.3	Horizontal displacement fields showing a propagating wavefront. The jet impact point and the plate boundaries are marked in red	47
4.4	Wave characteristics quantification method	48
4.5	Distribution of $V(r)$ peak-to-peak distances for the first three peaks for all jet velocity cases	49
4.6	Distribution of $V(r)$ peak amplitudes for the first and second peak for all jet velocity cases	50
4.7	Extraction of temporal information from $V(r)$ for the case of $u_e = 3.87$ m/s	51
4.8	Comparison of P_{rms} at different azimuthal angles	52
4.9	Comparison between sensor and CCPM results using the pressure scaling factor of 0.031 from Greidanus [3]	53
4.10	Comparison between the sensor and FSSS results using a new pressure scaling in Equation 4.2	55
4.11	Mean velocity profiles for the streamwise and radial velocity components for case $u_e = 4.58$ m/s with the coating plate. The dotted lines at $d = 1$ mm (green), $d = 2$ mm (yellow) and $d = 5$ mm (black) indicate locations along which analysis is performed	56
4.12	RMS velocity profiles for the streamwise and radial velocity components. The dotted lines at $d = 1$ mm (green), $d = 2$ mm (yellow) and $d = 5$ mm (black) indicate locations along which analysis is performed.	57
4.13	Comparison of the streamwise and radial turbulence intensity between the coating and rigid wall cases. Δ refers to the coating plate value subtracted by the rigid plate value	58
4.14	u_m, w_m as a function of distance from the impinging plate along the jet centreline	59
4.15	u_{rms} and w_{rms} as a function of distance from plate along the jet centreline	60
4.16	u_m and w_m as a function of radial distance from jet impact point at a fixed distance d from the impinging plane. (For ease of visualization, every 5 grid point was plotted)	62
4.17	u_{rms} and w_{rms} as a function of radial distance from jet impact point at a fixed distance d from the impinging plane. (For ease of visualization, every 5 grid point was plotted)	63
A.1	FSSS processing and post-processing flow chart with extended steps	69
A.2	Displacement field of several subsequent snapshots demonstrating background gradient varying in time, duration between two snapshots $\Delta T = 0.02$ s	70
A.3	Example of displacement vectors with background gradient	71

A.4	Geometry of a plate swinging backward around a pivot point, α equals to β as the dot pattern can be assumed to be in the same plane as the aluminum structure, $L_B > L_A$. . .	71
A.5	Displacement fields showing the worsening of background gradient as the jet velocity is increased	72
A.6	Linear fit of one line of the a) horizontal and b) vertical displacement field and 2D linear plane fit of the c) horizontal and d) vertical displacement field	73
A.7	Effect of the LINSUB operation	74
A.8	Effect of subsequent LINSUB and MSUB operations	75
A.9	Calibration curves of the pressure sensors, corresponded by colours	75
A.10	Single-sided amplitude spectra of the horizontal displacement field V	77
A.11	Single-sided amplitude spectra of the vertical displacement field W	78

List of Tables

3.1	Pump flow rate and jet exit velocity of the FSSS test cases	23
3.2	Properties of the viscoelastic coating used in experiments	24
3.3	Parameters of the dot patterns tested. Table coloured according to criteria on particle image diameter and particle image density by Moisy et al. [29], green = satisfied, red = not satisfied	27
3.4	FSSS acquisition parameters	32
3.5	FSSS parameters relevant to surface reconstruction	34
3.6	Parameters for calculating the uncertainty of surface reconstruction	37
3.7	PIV acquisition parameters	40
3.8	Pump flow rates and jet velocities of the test cases	40

Nomenclature

Abbreviations

<i>BOS</i>	Background-oriented schlieren
<i>CCPM</i>	Compliant coating-based pressure measurement
<i>CCS</i>	Calibrated colour schlieren
<i>DIC</i>	Digital image correlation
<i>DNS</i>	Direct numerical simulation
<i>DP</i>	Dot pattern
<i>DTA</i>	Dot-tracking algorithm
<i>FFT</i>	Fast Fourier transform
<i>FOV</i>	Field of view
<i>FSSS</i>	Free surface synthetic schlieren
<i>MZI</i>	Mach-Zehnder interferometry
<i>PDMS</i>	Polydimethylsiloxane
<i>PIV</i>	Particle image velocimetry
<i>PSP</i>	Pressure sensitive paint
<i>RMS</i>	Root mean square
<i>S – EB – S</i>	Polystyrene-b- (ethylene-co-butylene)-b-styrene
<i>TBL</i>	Turbulent boundary layer

Symbols

α	Ratio of refractive indices
β	Paraxial angle
ΔT	Duration between two adjacent snapshots
δ_v	Viscous sublayer thickness
δ_y	Background horizontal displacement
ϵ	Relative uncertainty of displacement field
η	Wave amplitude

λ	Wavelength
ρ_c	Coating density
σ^*	Largest absolute principal strain
σ_{nc}	Normal stress
ζ_c	Coating deformation
C_t	Shear wave speed
D	Dot diameter
d	Distance from impinging plane
d_t	Duration between laser pulses
f	Focal length
G''	Loss modulus
G'	Storage modulus
G^*	Shear modulus
H	Surface height
h_0	Effective surface-pattern distance
h_c	Thickness of coating
h_p	Thickness of polycarbonate plate
h_{cp}	Camera-dot pattern distance
L	Field of view size
M	Magnification
N	Number of snapshots
n_c	Refractive index of coating
N_d	Number of dots
N_g	Grid size
N_m	Number of sensors
n_p	Refractive index of polycarbonate plate
n_w	Refractive index of water
P	Pressure
r	Radial distance from jet impact point
Re_τ	Frictional Reynolds number
s_o	Object distance

u	Streamwise flow velocity
U_∞	Freestream speed
u_e	Jet exit velocity
V	Horizontal displacement
v	Spanwise flow velocity
W	Vertical displacement
w	Transverse flow velocity

Introduction

Turbulent flow is ubiquitous in nature and manifests itself in a wide range of applications such as industrial cooling/heating, the simulation of ocean currents and aircraft drag reduction. However, its chaotic and complex nature makes it difficult to predict as the governing equations cannot be solved analytically. Although numerical simulations such as direct numerical simulation (DNS) have been increasingly used to acquire accurate solutions, they still incur a prohibitive computational cost for complex geometries and/or high Reynolds numbers. In such cases, experimental data is needed.

1.1. Existing surface pressure measurement techniques

In wall-bounded turbulent flows such as for vehicle/transport applications, surface pressure measurements are crucial since they can be used to explain key changes in fluid-driven force components such as an increase in drag due to vortex shedding. Unfortunately, obtaining accurate surface pressure measurements with a high spatial resolution is no easy task. Currently, such measurements mostly rely on point-wise techniques such as placing individual pressure transducer taps on the measurement surface. Although straightforward, these techniques are not suitable for resolving dynamic pressure distribution over a large region with extensive spatial variation, as the cost builds up quickly with the number of sensors required for a sensor array. Therefore, a field measurement technique is needed.

One such technique, pressure-sensitive paint (PSP), has been successfully used in air [4]. The method relies on a photoluminescent coating which contains probe molecules that, when excited by light of an appropriate wavelength, release energy by emitting light at a higher wavelength when compared to the light source used for excitation [4]. A setup of the PSP technique is shown in Figure 1.1. The basic principle is based on the fact that higher local static pressure on the surface can be related to high partial oxygen pressure, which reduces the amount of luminescence as oxygen molecules are detrimental to the process, a phenomenon termed "oxygen quenching". However, due to its working principle, it cannot be extended for usage in liquid flows, where different techniques for field measurements need to be employed.

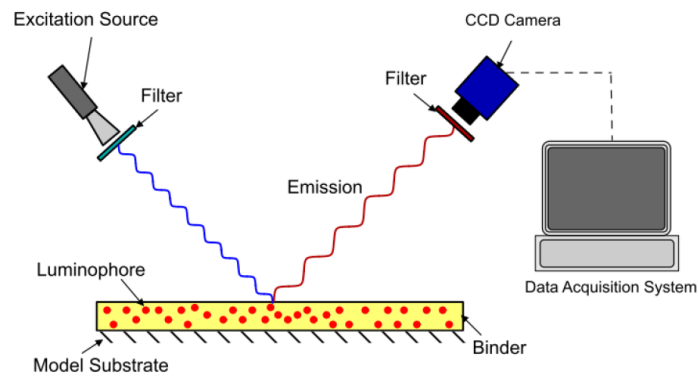


Figure 1.1: A polymer-based PSP setup. From Quinn et al. [5]

In liquid flows, one of the most promising non-intrusive pressure extraction methods is pressure reconstruction from velocity measurements. For this method, the momentum equation is used to obtain the pressure gradient from time-resolved velocity measured using particle image velocimetry (PIV). This pressure reconstruction technique is based on the fact that, for incompressible flows, the density is constant, while all the kinematic terms can be fully derived from velocity data [6]. The pressure can then be obtained by numerical integration of the pressure gradient, either by spatial integration or through Poisson's equation with the appropriate boundary conditions prescribed. A thorough accuracy analysis was carried out by van Oudheusden [6] and the method was validated through multiple experimental scenarios, including in 3D flow where planar PIV is able to provide reasonable accuracy when the out-of-plane flow component is relatively small. However, the accuracy of the reconstruction depends on the accuracy of the reference Dirichlet boundary conditions; these are not always available or sufficiently precise [6]. Therefore, although proven suitable in delivering instantaneous pressure in various flow scenarios, this method relies on prescribing accurate boundary conditions which makes the technique better suited to measurement in the bulk of the flow and not near solid boundaries.

1.2. Research questions

In this work, a novel underwater field surface pressure measurement technique based on the deformation of a compliant surface is proposed. The proposed technique exploits surface deformations to infer pressure and is based on a viscoelastic compliant coating. The coating, when applied on a surface, interacts with turbulent structures and its deformation is an indication of the pressure exerted on the surface.

The main research question that the investigation aims at addressing is:

Can a compliant coating-based pressure measurement (CCPM) technique be used to obtain order-of-magnitude accurate pressure fluctuation field measurement on a surface underwater?

Several sub-questions are derived to guide the investigation towards answering the main research question. The first sub-question concerns the working mechanism of the proposed system. In past studies, two coupling regimes have been identified for the interaction between fluid flow and a compliant coating. The one-way coupling regime where the coating deformation does not affect the surrounding flow is ideal for pressure measurement purposes. On the other hand, the two-way coupling regime in which the flow is affected by the coating would render the measurement technique an intrusive

one, although such a regime has been the target of drag reduction strategies. Therefore, it is necessary to assess the type and level of interaction between the coating and the flow, before any validation attempts or use of existing one-way coupling models for obtaining pressure from deformation. This interaction is naturally affected by both the coating and the flow properties. Since the target is to achieve a non-intrusive measurement technique, a natural subquestion is then to explore **what combinations of flow and coating properties are required to achieve sufficient coating deformation distinguishable by the optical setup while maintaining one-way coupling**. However, theoretically speaking, there is no absolute one-way coupling as the coating will always alter the flow to some degree. Although roughness effects have been used to formulate a threshold criterion for boundary layer flows in previous studies [3], such a criterion does not yet exist to clearly distinguish between one-way and two-way coupling regimes for other types of flows. Therefore, the question becomes: **given a flow scenario, to what extent does a chosen coating, which can deform sufficiently to be measured by a given optical setup, influence the flow? Furthermore, can experimental velocity data be used to establish such a criterion for distinguishing between the coupling regimes?** Answering this sub-question helps evaluate the suitability of a coating for extracting pressure in a given flow scenario when the CCPM system reaches maturity for application. Once the flow and coating parameters are set, the limitation of the system can be characterized: **what range of pressure fluctuations in the flow can the selected coating capture? What limits the resolution and accuracy of the CCPM?**

Moving towards the universal applicability of the CCPM technique even further, calibration-related questions need to be addressed before the implementation of the system. Since there is an existing model/scaling for obtaining pressure fluctuations from deformation [3], **can the one-way coupling model previously established from boundary layer flows be used for obtaining pressure fluctuations in a different flow scenario? If so, to what extent can the universality of the model be assumed? If not, what should an ad-hoc model look like?** To answer this last sub-question, a validation study is required to examine trends of pressure data obtained using the CCPM technique and a reference technique.

1.3. Research objectives

The main goal is thus to develop and assess a surface pressure measurement technique based on an in-house manufactured compliant coating. The operating principle of the CCPM technique is to measure deformations of the compliant coating induced by the flow on a submerged surface on which the coating is applied. To enable the functionality of the CCPM technique and to answer the research questions, a research plan is developed in this section.

The initial milestone is to capture the coating deformations induced by a flow. First, a compliant coating is prepared on a surface. A flow setup is then used to produce a range of pressure fluctuations in the flow field and an optical technique is used for the non-intrusive quantification of the coating deformations due to pressure fluctuations. Iterations are required to ensure the flow setup can induce coating deformations with sufficient magnitude such that they are quantifiable by the optical technique.

In addition, a flow measurement technique is used to characterize the flow field in order to assess the effect of coating deformation on the surrounding flow as only low degrees of two-way coupling are desired for pressure-sensing purposes. The literature suggests that the transition from one-way to two-way coupling regime can be identified through changes in the velocity profile [3] in addition to the occurrence of slow-moving large amplitude waves on the coating surface [7].

Next, the pressure fluctuations on the coating surface are extracted directly from the coating deformations. Past studies have shown that this can be achieved through a linear scaling between coating deformations and pressure fluctuations, at least in the case of turbulent boundary layer (TBL) flows in the one-way coupling regime [8]. It is unknown whether this scaling applies to other flows. Therefore, the current study aims to assess the suitability of this scaling for a flow other than a boundary layer flow through validation against pressure sensors. A new scaling is proposed if the TBL scaling is proven to be unsuitable.

Last but not least, the accuracy and resolution of the CCPM technique are assessed and its limitations are explored. Since this is a proof-of-concept study, the aim is to achieve order-of-magnitude accuracy and to lay a foundation for future systematic investigations which could involve a detailed variation of parameters.

1.4. Thesis outline

The thesis is structured as follows: Chapter 2 provides the necessary background on compliant coatings and their interactions with the flow, the optical technique used for the reconstruction of coating surfaces and the existing method for extracting pressure from coating deformations for TBL flows. Chapter 3 gives a detailed description of the experimental design of the CCPM technique developed and tested in this study. The results regarding the performance of the CCPM technique are discussed in Chapter 4 and the conclusions and future recommendations are presented in Chapter 5.

2

Background

2.1. Compliant coatings

Inspired by wavelike folds appearing in the skin of dolphins swimming in water [9], as demonstrated in Figure 2.1, Kramer first suggested that compliant coatings have the potential to reduce drag by altering boundary layer characteristics through hydroelastic coupling between the coating and the fluid [1]. Towards realization of the idea, he investigated a boundary layer stabilization technique called “distributed damping” which suppresses the transition to turbulence. He sparked excitement in the field after achieving up to 60% drag reduction when testing the method by towing test models with custom ducted rubber coatings with various stiffness behind a motorboat [1]. The coatings from the study consisted of a structural component made of natural rubber hoses and could be filled with a silicon liquid which was used as a damping fluid. To model the distributed damping, Kramer assumed the frequency and wavelength of the boundary layer waves are unaffected by the coating response. However, experiments in lab conditions afterwards failed to reproduce the results [10].



Figure 2.1: Wavelike folds appearing in the compliant skin of a Delphinidae during rapid swimming. From Gad-El-Hak [11]

As more insights over boundary layer transition came to light, researchers targeted transition delay as a drag reduction mechanism for laminar and transitional boundary layers [12] [13]. For turbulent boundary layers, investigations were not only geared towards boundary layer stability [14] but also skin friction drag reduction for fully-developed boundary layers [15] [16]. These efforts in drag reduction through compliant coatings were later summarized by Gad-el-hak [11].

Ever since Kramer’s first study [1], the effect of the coating response on the surrounding flow has

been shown to be the key to the drag modifications observed, whether it was successful drag reduction or undesired drag increase [17][18]. However, if the coating does not deform enough, it would not have a significant effect on the flow. This, on the other hand, is a desirable property for pressure-sensing purposes as it enables non-intrusiveness, and therefore, forms the basis for the proposed CCPM technique. These two distinct compliant coating-flow interaction regimes were later termed one-way coupling and two-way coupling. In the two-way coupling regime, the flow is significantly perturbed by the coating deformation which induces instability in the flow and can potentially result in drag changes [3]. In the one-way coupling regime, on the other hand, the coating deformation has a negligible effect on the dynamics of the flow.

Since the drag reduction studies, experts were keen on gaining more insights into the behaviour of compliant coatings and their interactions with the surrounding flow in order to explain the drag changes observed. While gathering baseline experimental data on the interaction of a viscoelastic compliant coating with turbulent boundary layers, Gad-El-Hak et al. [7] observed spanwise instability waves matching Boggs and Hahn's original prediction of the existence of large-amplitude wave structures [17]. These spanwise instability waves, as shown in Figure 2.2, are also known as "static divergence" waves since they have a wave speed much lower than the freestream flow speed [7]. During the experiments, the static divergence waves were observed whenever the convection velocity in the fluid was slightly larger than the propagation velocity (transverse wave speed) of the coating, indicating a strong interaction between the coating and the flow [7]. The transverse wave speed, also known as shear wave speed, is defined by:

$$C_t = (|G^*|/\rho_c)^{1/2}, \quad (2.1)$$

where $|G^*|$ is the shear modulus of rigidity and ρ_c is the density of the coating. As a result, the onset of the instability waves depends primarily on the freestream flow velocity and the modulus of rigidity of the coating. In addition, the study showed that the onset velocity depends on the thickness of the coating. It was concluded that the static divergence waves were a signature of two-way coupling, as no changes to the boundary layer structure were measured at freestream velocities below the onset velocity [7].

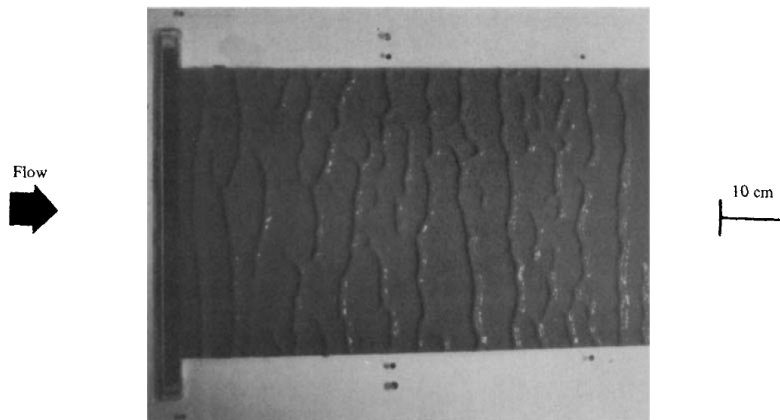


Figure 2.2: Static divergence waves under a turbulent boundary layer. From Gad-El-Hak et al. [7]

Around the same time, Duncan [19] established a model of the interaction between a TBL and a viscoelastic coating where experimental measurements are incorporated to create a more realistic pressure footprint. This model only allows for a one-way interaction between the imposed pressure

footprint and the coating. The study numerically characterized the response of viscoelastic coatings with different damping ratios when subjected to a range of flow speeds, as summarized in Figure 2.3. V-shaped travelling waves with a speed no larger than the pressure pulse speed of the turbulent boundary layer were predicted when the flow speed is sufficiently large ($U_\infty/C_t > 1.2$) and the damping is sufficiently low (< 0.5). The maximum amplitude of the coating response was approximately equal to the viscous sublayer thickness δ_v , from which the study concluded that even before exceeding the stability limit, the coating response might be large enough to alter the flow, entering what is now known as the two-way coupling regime [19].

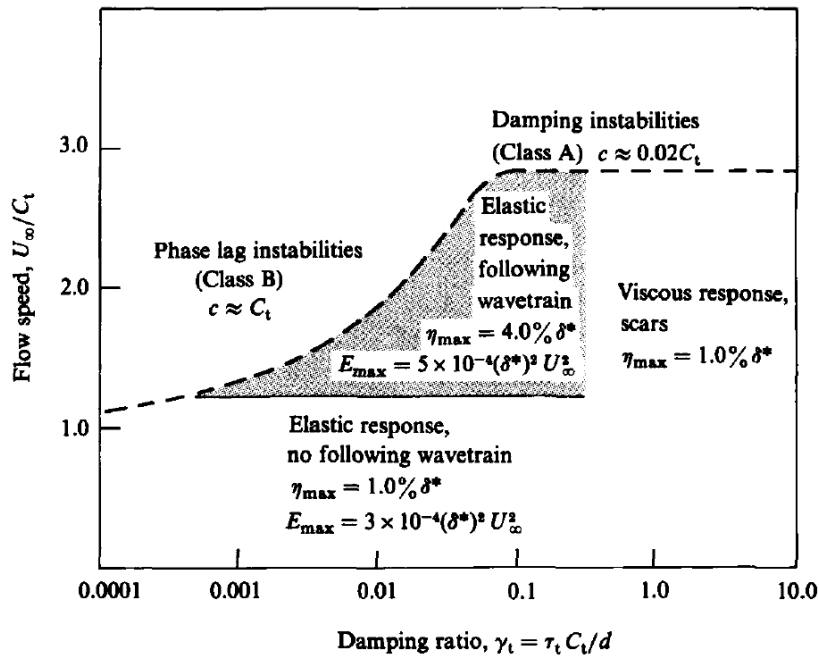


Figure 2.3: Response of an incompressible viscoelastic coating, where δ^* is the displacement thickness of the boundary layer, d is the coating thickness and τ_t is the shear relaxation time of the coating. From Duncan 1986 [19].

In recent decades, improved optical techniques helped unveil more intricate phenomena and provided experimental validation. Zhang et al. [2] investigated the one-way coupling interaction between a turbulent channel flow on a stiff coating using simultaneous PIV and Mach–Zehnder interferometry (MZI). Time-resolved PIV data was used to obtain pressure distributions through the integration of calculated material acceleration, while MZI was used to map out the wall shape for an extended field of view (FOV). The coupling between the flow and the coating was confirmed to be one-way as the root mean square value of the deformation after bi-directional linear detrending for filtering out channel vibration is much less than δ_v [2]. In addition, a streamwise phase lag between the deformation and pressure calculated from the measured velocity field was observed. They identified that a small fraction of the offset was due to viscoelastic damping while the majority was associated with a phase lag between near-wall pressure and pressure in the log layer. A fast (U_∞) and slow ($0.72U_\infty$) deformation wave speed associated with different flow structures in the boundary layer were identified. The study concluded that the coating thickness can be used to tune surface response based on flow features, as a length scale of around 1.9 times the coating thickness was shown to correspond to the fast mode. Furthermore, the study associated features in the deformation field with coherent structures in the boundary layer flow and provided a frequency-wave number spectrum for tuning compliant wall surface response

by selecting flow and wall parameters. For example, it was suggested that the coating response can be increased by matching the coating shear speed with the mean flow speed or the velocity at a wall distance where the Reynolds shear stress has the highest correlation with the coating deformation [2].

Recently, Benschop et al. [8] proposed a one-way coupling analytical model for computing the deformation of a liquid-coating interface given the coating properties and the stresses from a turbulent flow over a rigid wall, where the fluctuating interface stresses are modelled using a sum of streamwise travelling waves uniform in the spanwise direction. In order to validate their model with experiments, Benschop et al. [8] tested a set of compliant coatings made from triblockcopolymer polystyrene-*b*-(ethylene-co-butylene)-*b*-styrene (S-EB-S) and a mid-block selective paraffin oil, with varying S-EB-S concentrations. The concentration of S-EB-S is correlated to the stiffness of the coating as it increases the cross-link density of the material. Although Polydimethylsiloxane (PDMS) based coatings were used in past studies on compliant coating-fluid interactions [20], this new coating was chosen for the current study as it does not age quickly and is, therefore, able to maintain its mechanical properties over a longer period of time [8]. The theoretical model is not able to predict the measured displacement amplitudes well, as shown in Figure 2.4, where a factor of 0.35 was used to artificially provide a closer match between results from the model and experimental surface displacements. In addition, Figure 2.4a shows that for coating 1, at a velocity of $U_\infty = 4.5$ m/s ($Re_\tau = 7500$), there is a sudden increase in vertical displacement as well as drag, signalling a transition to the two-way coupling regime which the model failed to predict as it is based on the one-way coupling assumption. However, as seen in Figure 2.5, the model captures the trend of the spectra relatively well for increasing Reynolds number, especially for the softest coating (coating 1). For coating 2, the shift of the peak in the experimental data for increasing Reynolds number was attributed to fluid-structure interaction [8]. Furthermore, Figure 2.5a shows that root mean square (RMS) values of the experimental data for vertical surface displacement $\zeta_{c,rms}$ for all three coatings collapse onto a single curve with a proportionality factor of 0.031 when plotted against the normalized normal stress:

$$\zeta_{c,rms}/\delta = 0.031\sigma_{nc,rms}/|G|, \quad (2.2)$$

where δ is the coating thickness, $|G|$ is the coating stiffness parameter, and $\sigma_{nc,rms}$ is the RMS of the normal stress/pressure obtained from an empirical pressure spectrum model [8]. The results are in line with the assumption that the coatings behave as linear solids as the relative coating deformation $\zeta_{c,rms}/\delta < 0.01$ for most measurement points [8].

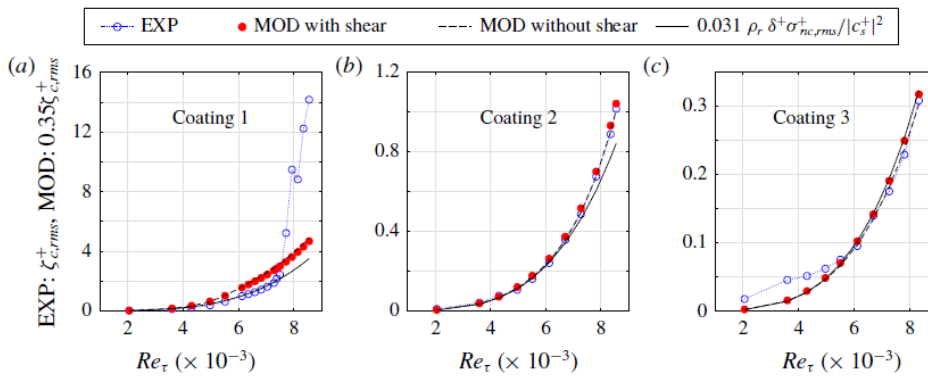


Figure 2.4: The measured and modelled vertical surface displacement $\zeta_{c,rms}^+$ as functions of the Reynolds number for three different coatings. From Benschop et al. [8]

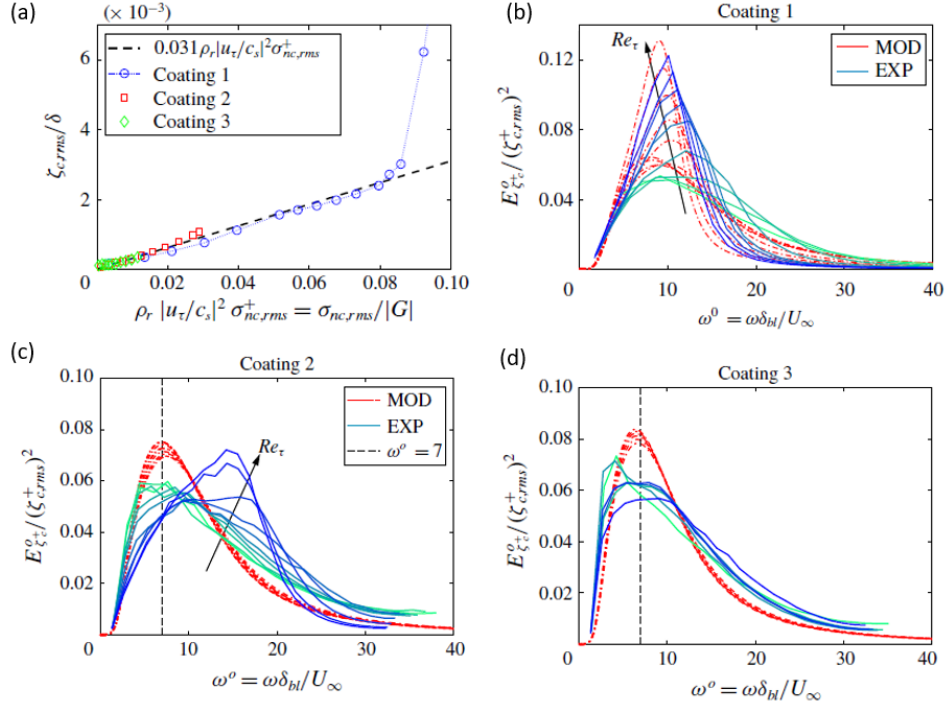


Figure 2.5: *a)* The measured vertical surface displacement for all three coatings as a function of the normalized stress. *b) – d)* The measured and modelled point spectra of the vertical surface displacement as functions of the angular frequency in outer units for coating 1,2,3, where the vertical displacement spectra are normalized in outer units $E_{\xi_c^+}^o = E_{\xi_c^+} U_\infty / \delta_{bl}$. From Benschop et al. [8]

It is not known if the scaling in Equation 2.2 holds for other flow scenarios and the scaling factor of 0.031 contains unknown factors, but it nevertheless inspired the proposed development of a CCPM technique where pressure fluctuations are extracted from compliant coating surface deformations in the one-way coupling regime.

Using the same set of coatings and flow scenarios as Benschop et al. [8], Greidanus [3] further studied the effect of coating parameters on the onset of instability. He noticed that the coating displacement increases linearly with coating thickness for thin coatings with thickness less than the viscous sublayer. However, for very thick coatings, the deformation no longer depends on the thickness. In addition, although a softer coating deforms more, significantly decreasing the stiffness also resulted in nonlinear behaviours in the materials themselves [3]. It was concluded that the coating deformation increases linearly with the fluid-to-solid density ratio until it reaches a critical value and the interaction then enters a two-way coupling regime [3]. The threshold between one and two-way coupling was defined using the roughness effect by comparing coating surface wave amplitude to the viscous sublayer thickness δ_v of the boundary layer flow, as suggested by Duncan [19]. Experimentally, it was observed that when transitioning from one- to two-way coupling, the root mean square of coating displacement starts to increase significantly faster [3], as shown in Figure 2.6 where experimental results similar to Benschop et al. [8] are illustrated in a log-log scale and the threshold of the coupling regimes is marked, and the pressure is estimated from measured wall shear stress using the same pressure spectrum model as Benschop et al [8]. It is evident that outside of the one-way coupling regime, experimental data deviates from the linear curve quickly. In addition, the deviation also increases for very small deformations in the one-way coupling regime due to nonlinear effects.

Furthermore, as shown in Figure 2.7, high-amplitude wave trains due to energy being transferred

towards the coating start to form at the transition velocity, similar to the observations by Gad-El-Hak et al. [7] (Figure 2.2). In addition, there were changes in the local mean velocity profile before the transition to two-way coupling and a 5% increase in local shear stress due to low-level interaction even though global force measurements do not suggest changes in drag [3]. This points towards a potentially measurable criterion for identifying the onset of two-way coupling that does not rely on knowing the viscous sublayer thickness and could be applicable in flows other than turbulent boundary layer flows.

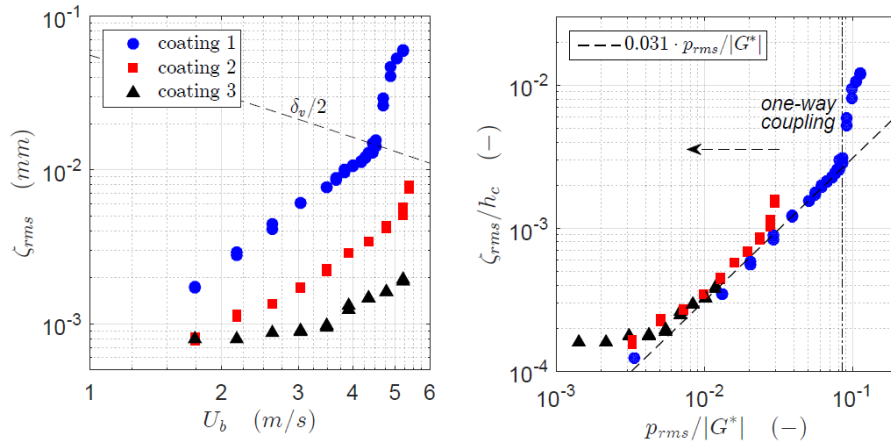


Figure 2.6: Surface height variation of the three coatings: *a*) Root-mean-square values as a function of the bulk velocity. *b*) RMS-values scaled with coating thickness in relation to the pressure fluctuations scaled with coating shear modulus. From Greidanus [3]

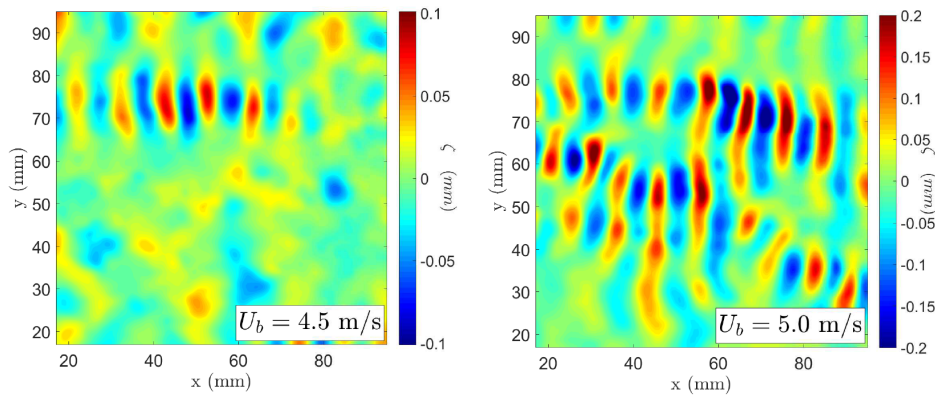


Figure 2.7: A high amplitude wave train first appearing in the instantaneous surface height field at the transitional velocity of 4.5 m/s (left) and more wave trains appearing at a higher velocity of 5.0 m/s (right). From Greidanus [3]

2.2. Measurement of surface deformation

In order to develop a CCPM system, capturing the deformation of the compliant coating surface is crucial as it is directly linked to pressure fluctuations. This section explores the existing optical techniques that have the potential to achieve this, many of which have their roots in density measurements and were later adapted to reconstruct a deformed liquid surface or other interfaces.

2.2.1. Densitometry

The **classical schlieren** technique was invented in the 19th century, originally for the purpose of visualizing density features in compressible flows, notably shock waves. The schlieren technique utilizes the refraction of light rays due to variation in density [21]. The original single-lens system consists of a light source, a lens, a knife-edge and a camera, but has since been improved upon to obtain both qualitative and quantitative measurements [22]. For strong gradients and when there is no requirement for capturing detailed features, shadowgraphy is sometimes used instead to capture only the sharp edges in view of its simpler setup [23].

Deriving from the classical schlieren technique, a new category of density measurement techniques called synthetic schlieren was developed [24]. The **synthetic schlieren** techniques have similar operating principles as the classical schlieren methods [24]. However, they make use of digital processing instead of optical/mechanical processing. The main advantage is that they are much simpler to set up and can provide information on a larger domain or when shadowgraphy is not useful. Of the four synthetic schlieren techniques mentioned in the paper, the latter three are quantitative extensions of the first method, qualitative synthetic schlieren. These quantitative methods are able to extract accurate quantitative density data using different masks: line refractometry which uses lines in the mask, dot tracking refractometry which uses arrays of dots as a mask, and pattern-matching refractometry which uses a randomized array of dots and pattern-matching algorithms [24]. For all of these methods, the distortion in the texture of the mask is used to determine the density perturbation field through density gradients [24].

Klinge and Riethmuller [25] developed a technique with an even simpler setup termed the **background-oriented schlieren (BOS)** technique, which can provide measurements of local density with only a background image, a light source and a camera. A setup of the BOS system is shown in Figure 2.8. This technique utilizes the fact that light rays deflect through a density gradient, causing images to distort when viewed on the other side of the medium. Tracking the movement of a predefined image provides the density gradient field. For BOS, correlation algorithms such as digital image correlation (DIC) are used to extract the apparent movement of random dots through a medium with a density gradient which allows for capturing finer features in the flow field [26].

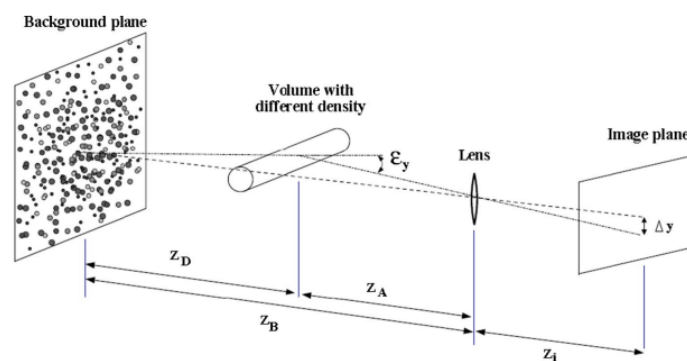


Figure 2.8: BOS imaging configuration. From Raffel [26]

Elsinga et al. [27] compared BOS with another quantitative schlieren method: **calibrated colour schlieren (CCS)**, through supersonic baseline experiments. Both methods are schlieren-based and can provide a density field. The CCS uses a colour filter to measure deflection angle in two directions

through the colour ratio, whereas BOS relies on the apparent displacements of a random dot pattern due to refraction. The study claimed that BOS has limited spatial resolution and requires additional boundary corrections to account for vibrations, while CCS has a more limited dynamic range [27].

2.2.2. Surface measurement

Grating-based technique

In 1990, the first example of a technique to reconstruct the topology of a liquid surface emerged when Kurata et al. [28] introduced a **grating-based measurement** method to obtain the shape and depth of a shallow water channel. The method is non-intrusive and simple to operate as it is solely based on the transmitted image of a grating pattern and uses an optical system that does not require any special light source. Using simple geometrical calculations and the principle of refraction, the water surface can be reconstructed using the movements of feature points as seen from the same camera between the original grating at the bottom of the water channel and a distorted one that appears on the surface when a simple light source (eg: lamp) illuminates the water from beneath [28]. The setup, shown in Figure 2.9, is similar to the BOS setup except that a grating was used instead of a dot pattern as correlation algorithms not yet existed and, therefore, calculations of the displacement between the original grating and the modulated grating need to rely on geometrical equations alone [28]. The technique was demonstrated successfully as a contour line map of the surface was reconstructed from water depth data to recognize key flow features [28].

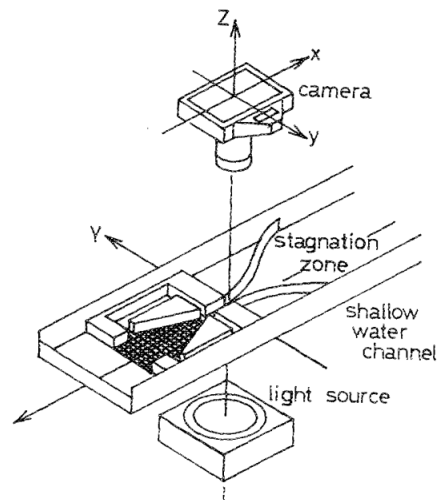


Figure 2.9: Location of components of the grating-based optical system. From Kurata et al. [28]

Free surface synthetic schlieren (FSSS)

Sharing great similarity with Kurata's grating-based measurement method, the BOS technique was naturally extended to measure liquid surface topology in addition to the density field. Moisy et al. [29] provided a detailed characterization of a synthetic schlieren method referred to as the **free surface synthetic schlieren (FSSS)** technique for measuring the topography of a liquid surface. The setup is similar to the BOS technique, with the difference being the presence of a liquid interface, the deformation of which acts as a concave or convex lens due to light refraction, distorting the fixed dot pattern. Figure

2.10 provides a 3D and 2D view of the incidence plane which illustrates the ray principle that the FSSS technique relies on, where a ray coming from point M appears to come from M' due to refraction at the deformed interface. Moisy et al. [29] proved that the apparent displacement of the dots calculated using a DIC algorithm, which compares the deformed dot pattern with the reference dot pattern, is assumed to be proportional to the slope of the deformed surface for small displacements/slopes:

$$\nabla H = -\frac{\delta r}{h^*}, \quad (2.3)$$

with

$$h^* = \frac{1}{\alpha h_0} - \frac{1}{h_{cp}}, \quad (2.4)$$

where h_{cp} is the distance between the dot pattern and the camera, α is related to the ratio of the refractive indices of air and water, and h_0 is the effective surface-pattern distance that accounts for the effect of refraction through multiple layers of materials on the apparent dot displacement, as shown in Figure 2.11. In the case of small deformations and dot patterns that optimize the DIC cross-correlation procedure, the uncertainty of the displacement field calculation is determined by the uncertainty of the DIC algorithm which has been examined in studies on PIV uncertainty [30].

The surface slopes are then least-square integrated over a chosen grid which is used for defining the residual to be minimized for finding the optimal surface height. This allows the entire surface topology to be reconstructed. The study showed good agreement of both the displacement field and the reconstructed surface with expected values obtained in a validation experiment using the deflection of a reflected laser beam [29]. An empirical law was obtained where the relative resolution of surface reconstruction is linearly related to the uncertainty of the displacement field [29]:

$$\frac{\Delta\eta}{\eta_{rms}} = (5.0 + 0.2) \frac{L\epsilon}{\lambda N_g}, \quad (2.5)$$

where L is the field of view dimension, N_g is the grid size, ϵ is the relative uncertainty of the input displacement field, λ is the wavelength, η is the wave amplitude.

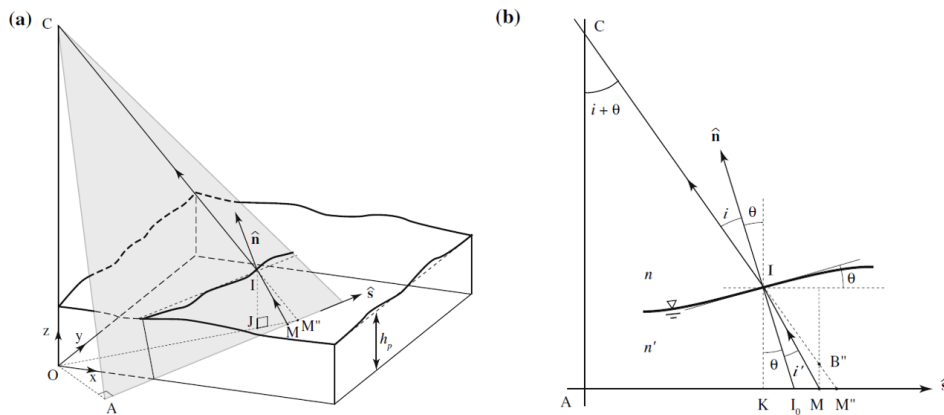


Figure 2.10: a) 3D ray geometry of an arbitrary surface showing the incidence plane CAM, defined by the dot pattern point M, the camera location C, and the unit normal vector \hat{n} at the point I where the light ray MIC intercepts the interface. b) 2D view of the incidence plane illustrating the ray principle. From Moisy et al. [29]

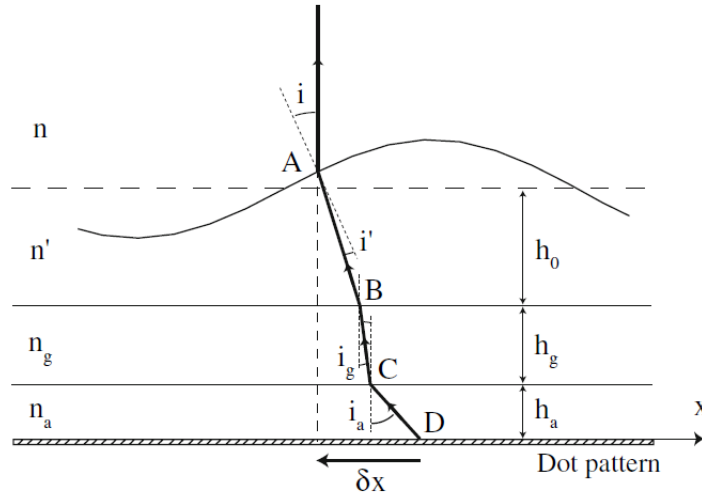


Figure 2.11: Apparent dot pattern displacement due to multiple layers of materials with different refractive indices. From Moisy et al. [29]

Assumptions and rules of thumb of FSSS

To arrive at Equation 2.3 and to achieve a proper surface reconstruction where Equation 2.5 applies, several assumptions must be met. In addition, limitations of the FSSS technique were identified, for which rules of thumb are proposed [29]. They are presented in this section.

Parallax distortion

Firstly, a finite camera-to-pattern distance leads to parallax distortion as the surface gradient is measured at point I where the light ray from M to C crosses the interface and not at the vertical projection of M on the interface, as shown in Figure 2.10. This limits the resolution of surface reconstruction to h_0/h_{cp} [29]. However, in the case of an insufficient camera-pattern distance, it can be corrected using a remapping procedure before integration based on:

$$OJ = (1 - h_0/h_{cp})OM'', \quad (2.6)$$

where the locations of the points O, J and M'' are shown in Figure 2.10a) [29].

Paraxial/small angle approximation

Secondly, FSSS uses the paraxial/small angle approximation, where the dot pattern-camera distance h_{cp} is assumed to be much larger than the field of view size L such that the maximum paraxial angle satisfies the following [29]:

$$\beta_{max} \approx L/(\sqrt{2} h_{cp}) \ll 1. \quad (2.7)$$

The paraxial angle is defined in Figure 2.12.

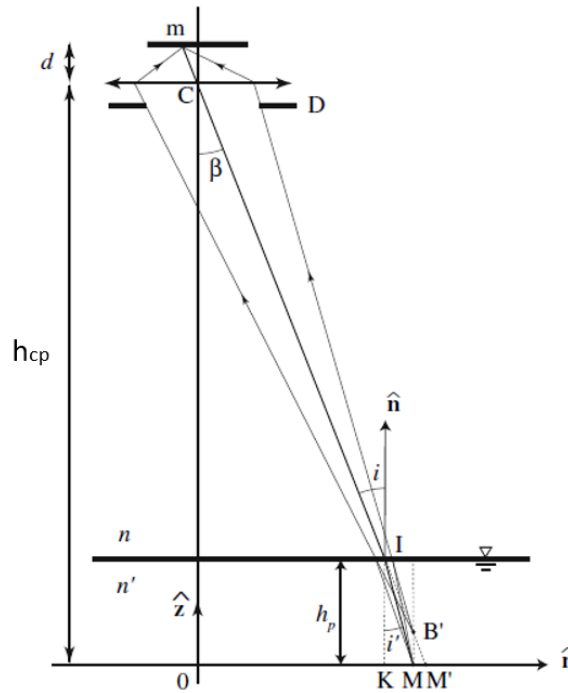


Figure 2.12: 2D view of the vertical incidence plane showing camera location C, camera-pattern distance h_{cp} and paraxial angle β . From Moisy et al. [29]

Ray crossing

Thirdly, although a large surface-to-pattern distance increases the resolution, the ray crossing phenomenon illustrated in Figure 2.13 could occur when the surface-to-pattern distance exceeds a critical value or when the interface curvature is significant, resulting in incorrect images.

To avoid ray crossing, the effective surface-pattern distance h_0 needs to be sufficiently small to satisfy the following condition [29]:

$$h_0 < h_{0,c} = \frac{\lambda^2}{4\pi^2 \alpha \eta}. \tag{2.8}$$

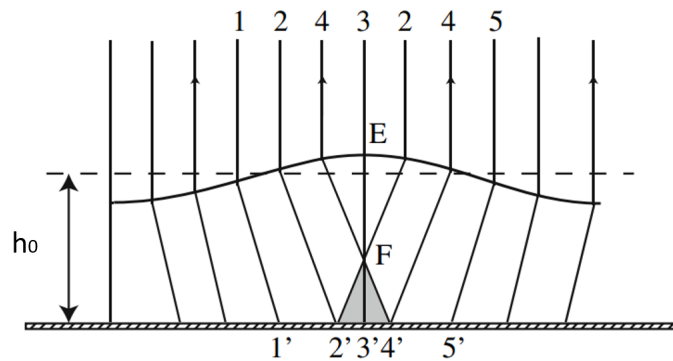


Figure 2.13: Ray crossing phenomenon when h_0 is larger than the focal length EF of the wave crest. In this case, the sequence of points 2'3'4' on the pattern will be seen as reversed, where 2' and 4' have multiple images. From Moisy et al. [29]

Image strain

Last but not least, the moderate strain assumption needs to be met for the FSSS method to prevent non-circular dots which would increase the uncertainty of the displacement field [29]. When DIC is used, the RMS of the largest principal strain over the entire field needs to satisfy the criterion in order to prevent regions of large surface curvature from polluting the quality of the entire reconstructed surface due to the non-local integration procedure [29]. In the case of the x-y plane, for example, the criterion is:

$$\sigma_{rms}^* = \sqrt{\frac{1}{N_x N_y} \sum_{x,y} \sigma^{*2}(x, y)} < 0.15, \quad (2.9)$$

where N_x and N_y are the number of grid spacings in each direction and the largest absolute principal strain field is used:

$$\sigma^* = \max(|\sigma_1(x, y)|, |\sigma_2(x, y)|) \quad (2.10)$$

with $\sigma_1(x, y)$ and $\sigma_2(x, y)$ being the two highest principal strains [29].

Vibrations

According to the literature, the FSSS technique is also very sensitive to vibrations in the setup [29], which could lead to synthetic background displacements of the dot pattern that once integrated, superimposes to the surface height field. If the background displacement field is due to in-plane vibrations, the resulted mean slope can be subtracted before integration [29].

On the other hand, out-of-plane vibrations would result in a non-uniform background displacement field which would require more advanced procedures to remove. The effect of out-of-plane vibrations has not been addressed formally in the literature.

Extension to water-coating interface

The FSSS technique is not limited to the detection of an air-water interface. As Moisy et al. [29] pointed out, the key to the reconstruction of the surface height is that for a free surface, there is a step-like change in the refractive index. This property also applies to other interfaces where the refractive indices are different on the two sides, as shown by the studies by Benschop et al. [8] and Greidanus [3] that successfully reconstructed the deformed surface of a compliant coating in water using FSSS. In the study by Greidanus [3], a compliant coating was applied on a rigid plate and tested in a water channel [3]. The setup is shown in Figure 2.14 where a camera captures the apparent displacement of the background dot pattern due to refraction at the water-coating interface. An example raw image of the dot pattern captured by the camera and the corresponding displacement field as well as the reconstructed coating surface height are shown in Figure 2.15.

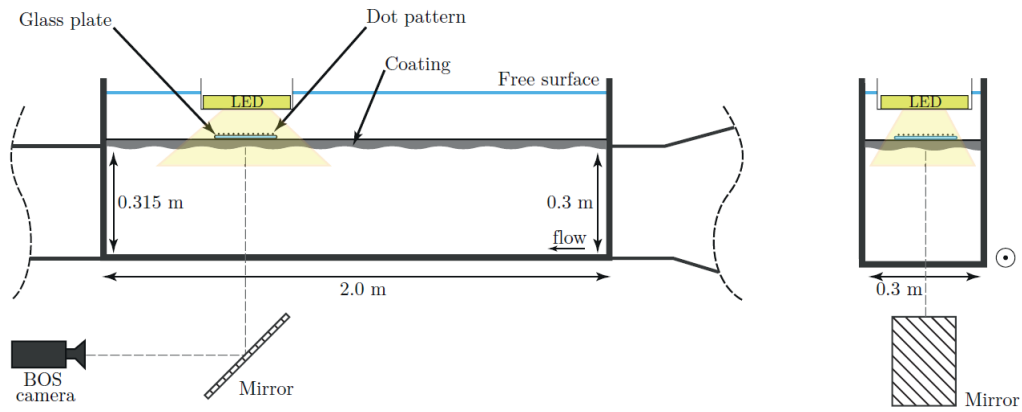


Figure 2.14: FSSS setup for performing surface deformation measurements. From Greidanus [3]

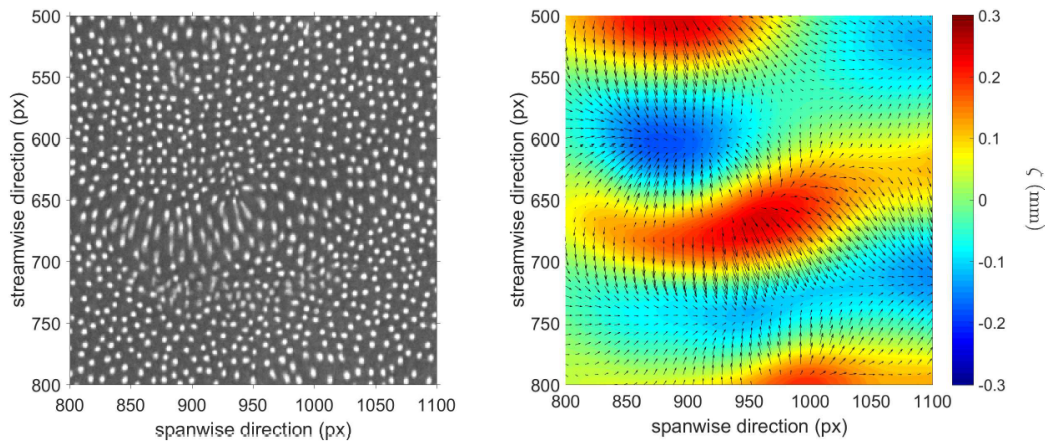


Figure 2.15: Example image of a deformed dot-pattern (left) and the corresponding computed displacement vector field (arrows) and reconstructed surface height field (colour) (right). From Greidanus [3]

Although FSSS was recommended for small deformations [29], recently, by using a dot-tracking algorithm (DTA) instead of a correlation algorithm based on DIC, Charruault et al. [31] were able to modify the FSSS technique to allow the measurement of stronger surface curvatures, therefore larger deformations. First, the dot-tracking algorithm was tested on a compliant coating with mild deformations induced by a travelling wave. It was shown that DTA performed as well as a DIC-based algorithm. Next, an air cavity was used to test the DTA's ability to capture strong deformations. Results in Figure 2.16 show that DTA computed a higher number of correlation peaks with values between 0.6 and 0.96 and has a larger area with values above 0.5 in the correlation map than the DIC algorithm in PIV.

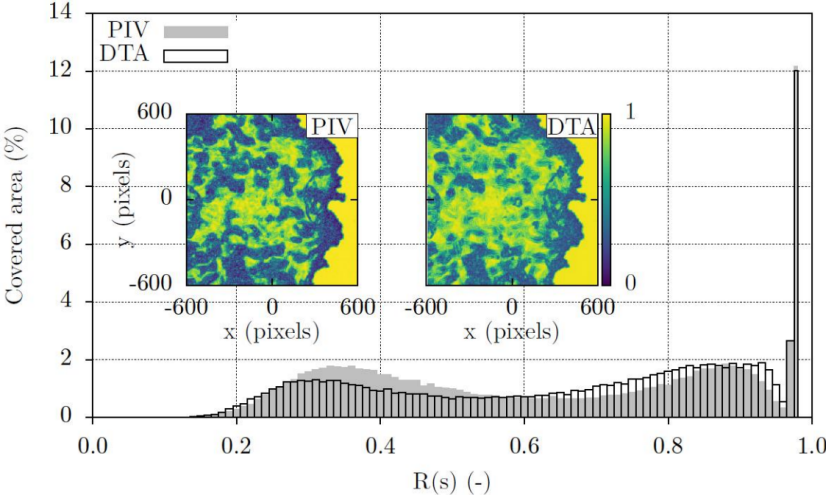


Figure 2.16: Histogram of the maximum correlation peaks when computing the cross-correlation between the reference undeformed image and the deformed image. The contour plots represent the normalized cross-correlation maps. From Charruault et al. [31]

3

Experimental design of a CCPM system

3.1. Requirements

The CCPM technique described in this chapter was designed and constructed according to system-level and subsystem-level requirements derived from the research questions and objectives in Chapter 1. The requirements are discussed in this section.

System

As per the functional objective of a CCPM technique in Chapter 1, the technique must be compatible with usage in water and be able to provide field measurements over the region of interest. In addition, as a proof-of-concept, the aim is to achieve order-of-magnitude accuracy. This is only possible in the one-way coupling regime as in the two-way coupling regime the coating would affect the flow itself, rendering the CCPM technique intrusive. Hence, the technique should also be able to distinguish between the two coupling regimes in order to provide reliable results.

Compliant coating

In addition to the need for the compliant coating to be able to sustain its properties for a sufficient duration of time during testing underwater, the requirements for the compliant coating are interdependent on the requirements for the deformation quantification technique. The coating must be able to deform sufficiently such that the deformation can be detected for the deformation quantification method. Furthermore, the coating shall be transparent as the literature suggests that it is an essential part of the working principle for many non-intrusive deformation quantification techniques that rely on tracking a background pattern through the material.

Deformation quantification

To properly retrieve the coating deformation, the deformation quantification procedure must be non-intrusive. As per system-level requirements, the technique shall provide the surface deformation of the region of interest. More specific requirements pertaining to the deformation quantification technique

depend on the specific technique chosen and will be discussed later.

Flow quantification

To determine whether the coating deformations affect the adjacent flow field, a flow quantification technique is needed for which 2D velocity vectors in the plane perpendicular to the coating plane are sufficient as output. More specific requirements regarding the flow quantification technique depend on the specific technique chosen and will be discussed later.

Test flow

The test flow is not a part of the CCPM technique but is crucial for evaluating its performance. To isolate purely flow-related complexity and focus on the flow-coating interaction, a simple and well-known flow is desired. As it is unknown when the transition from one-way to two-way coupling occurs, it is desirable to test out a large range of pressure fluctuations such that both regimes can be observed if possible. Therefore, a difference between the minimum and maximum pressure fluctuations of at least one order of magnitude is desired. This requirement has, however, a lower priority as the feasible range of pressure fluctuation is dependent on the coating properties and the deformation quantification method. The maximum pressure fluctuation is limited by the coating as surface breakage is possible in the case of high pressure variations. On the other hand, too small a pressure fluctuation might not induce sufficient deformations detectable by the deformation quantification method.

Validation method

The validation method provides the reference pressure data for comparison with CCPM outputs. As the CCPM results can be no more accurate than the validation method during the validation experiments, the validation method should be sufficiently accurate (at least to the order-of-magnitude) such that the CCPM can be within order-of-magnitude accurate when compared to the true pressure.

3.2. System overview

The design of a CCPM technique requires the integration of the following individual components mentioned in the previous section: a test flow setup, a compliant coating, a deformation measurement technique, a flow quantification technique and a pressure validation method. Based on the literature, as described in the previous chapter, free surface synthetic schlieren (FSSS) is chosen as the deformation measurement technique as it has been shown to be able to measure the interface topology between two mediums with different refractive indices including water and compliant coating [8] and with high accuracy (2%) provided that the underlying assumptions mentioned in Section 2.2.2 including small deformation and a proper optics arrangement are met [29]. Particle image velocimetry (PIV) is chosen as the flow quantification technique as it can provide high-resolution high-accuracy flow velocity data in the region of interest. A submerged impinging jet is chosen as the test flow to provide a sufficient range of pressure fluctuations and pressure sensors are chosen to provide reference validation data. Each component as well as the motivation behind it will be discussed in detail in the sections that follow.

Since this is an exploratory study, it is not the aim of the project to achieve the highest accuracy possible for a CCPM technique through optimization of the components, but rather a proof of concept aiming at obtaining an order-of-magnitude accuracy in the RMS value of the pressure fluctuations.

An iterative process was first carried out using various combinations of coating and flow parameters with the aim to achieve a sufficient deformation that can be measured by the FSSS setup. This required

balancing the coating parameters (stiffness, thickness), jet parameters (flow rate, nozzle diameter), and the distance from the jet nozzle exit to the coating. Once this feasibility milestone was reached, all but one parameter (flow rate) were fixed and a set of validation experiments were conducted by varying the remaining free variable to assess the performance of the CCPM technique when compared to pressure sensors.

The test flow scenario, as well as the final experimental configuration, are shown in Figure 3.1. A submerged jet going downstream in the x direction impinges on a coating plate in the y - z plane. The coating plate consists of a polycarbonate plate with a homogeneous layer of compliant coating on the side facing the jet. On the other side of the coating plate is a background dot pattern which was illuminated by an LED from the back of the tank during the FSSS experiments. For the FSSS experiments, a camera was pointed at the coating from the front of the tank, taking images of the dot pattern through the transparent coating. The images were then used to extract the coating surface deformations. For the separate PIV experiments, a laser sheet (coloured orange) was produced in the x - z plane intersecting the coating plate in an orthogonal manner. A camera positioned on the side of the tank was pointed at the laser sheet, capturing the 2D components of the flow in the x and z directions. For gathering the pressure validation dataset, the coating plate was replaced by a plate with flush-mounted pressure sensors to measure the pressure fluctuations at a few selected points on the impinging surface. The pressure from the pressure sensors was then compared to the pressure extracted using FSSS.

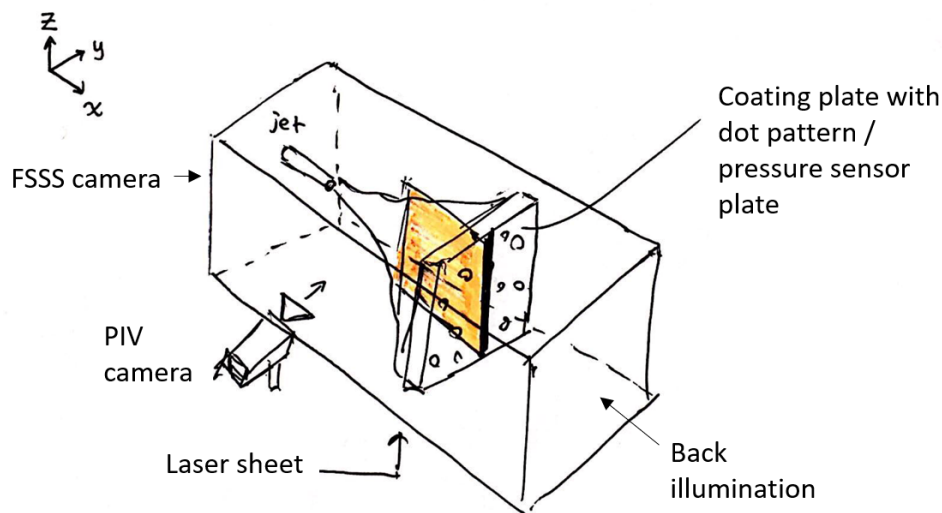


Figure 3.1: A sketch of the experimental setup, note that the coating plate is exchangeable with the validation sensor array plate

3.3. Test flow

To study the response of the coating when subject to flow perturbation, a facility and an underwater test flow setup are needed. The flow parameters determine the range of pressure fluctuations on the measurement surface. For proof-of-concept purposes, it is desirable to test a range of pressure fluctuations with a relatively simple and controllable flow underwater. A turbulent impinging jet setup was chosen to achieve a high dynamic range of pressure fluctuations as it contains flow structures with a large range of scales [32].

Experiments were conducted in an open water tank at the Laboratory for Aero and Hydrodynamics

at TU Delft. The water tank has a test section length of 200 cm and a cross-section size of 60 cm by 60 cm. A diagram of the water tank setup is shown in Figure 3.2. A horizontal jet was positioned at a distance of 35 cm downstream of the front wall of the tank. The water tank was made recirculating, driven by a SAER 32/3 electric centrifugal pump which was controlled through a dial knob which regulates the flow rate through the circuit and thus the jet speed. The flow rate was detected by a Badger 3012 4F16 flow rate sensor with a range of 5 to 65 L/min and a 3% accuracy. The recirculating mechanism ensures that the water level within the tank can be kept constant, which removes the constraint on experimental acquisition time due to a changing water level, and also mitigates changing hydrostatic pressure at a fixed point within the tank which could bias the pressure sensors over time. A water height of 55 cm was chosen such that there is an equal amount of water above and below the jet nozzle to prevent shear in the z-direction.

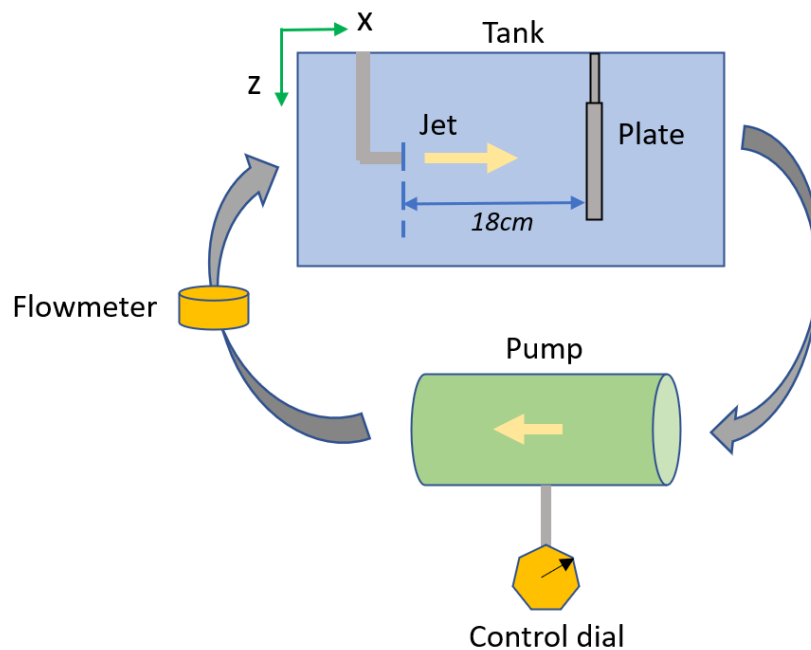


Figure 3.2: Configuration of the recirculating water tank setup

The field of view (FOV) and the distance from the nozzle to the impinging plane were determined simultaneously by balancing the characteristics of the camera and lens and the amount of space available through trial and error. On one hand, the FOV needs to include the entirety of the jet cross-section for analysis. On the other hand, the FOV is also limited by the size of the coating plate which is in turn limited by the size of the oven available for manufacturing the coating and the size of the water tank cross-section. A jet half angle estimate of 11.8° was used for the initial estimates of the jet cross-sectional area as it is a typical value for turbulent jets according to the self-similarity principle [33]. An illustration of the development of a turbulent jet is shown in Figure 3.3. Through trial and error, a FOV of approximately 15 cm by 18 cm was chosen as it is large enough to encompass the full jet cross-sectional area while remaining feasible for coating manufacturing. The aspect ratio is due to the camera sensor size. At the same time, a compatible nozzle diameter of 5 mm and a nozzle-to-coating distance were chosen to be 18 cm for all experiments.

The pump has a maximum driven frequency of 50 Hz and a resolution of 0.005 L/s. It was operated in the range of 0.043 L/s to 0.1 L/s to avoid coating surface breakage while ensuring the coating

deformations are sufficient to be measured by the deformation quantification method. This gives a jet exit velocity (u_e) range of 2.19 m/s to 4.84 m/s. A number of jet velocities within this range were selected for the FSSS experiments. The pump flow rate and corresponding jet exit velocity of the FSSS test cases are detailed in Table 3.1.

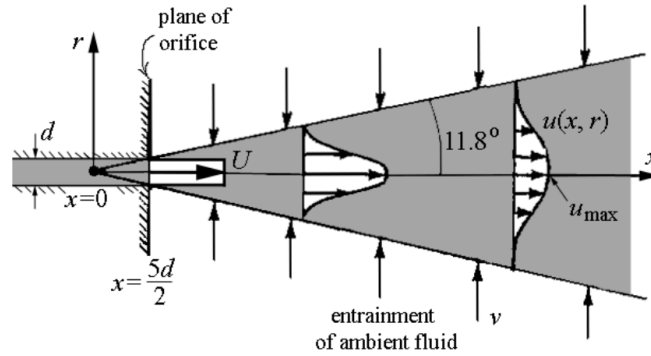


Figure 3.3: Illustration of a turbulent jet. From Cushman-Roisin [33]

Table 3.1: Pump flow rate and jet exit velocity of the FSSS test cases

Pump flow rate (L/s)	0.043	0.052	0.067	0.071	0.076	0.081	0.090	0.095
Jet exit velocity (m/s)	2.19	2.65	3.41	3.62	3.87	4.13	4.58	4.84

3.4. Compliant coatings

The compliant coating is the core component of the CCPM system. Although its interaction with a turbulent boundary layer flow has been studied previously [3] and it has been suggested to be a promising method for drag reduction [11], there have been no attempts at using it for pressure measurement purposes. Previous studies on coating-flow interactions have shown that the material composition, coating thickness, and stiffness are the key parameters that determine how a coating responds to pressure fluctuations [3]. A specific type of viscoelastic coating produced by Greidanus [3] was tested in the experiments since it meets the requirements in Section 3.1 and creating coatings with new chemical compositions is outside the scope of this project. The coating characteristics and manufacturing techniques are detailed in this section.

3.4.1. Material properties

A viscoelastic coating made from a mixture of triblockcopolymer polystyrene-b-(ethylene-co-butylene)-b-styrene (S-EB-S) and mid-block selective paraffin oil previously tested by Greidanus [3] was used for the experiments. It has a slower aging property when compared to the silicon-based compliant coatings used by other studies as, in contrast to the polymerization of silicon-based materials, physical bounds are created during the coating synthesis and no continuous cross-link reactions between polymer chains occur [3]. The coating with the material properties listed in Table 3.2 was used for the validation experiments as initial tests verified that it could provide sufficient deformation measurable by the deformation quantification technique with the chosen range of jet velocities at the selected nozzle-to-coating distance. The material is considered incompressible for the range of pressure in this

study as the bulk modulus is around 5 GPa [3]. The shear wave speed of the coating is calculated using Equation 2.1, where the shear modulus $|G^*|$ is a composition of the storage modulus and loss modulus:

$$|G^*| = \sqrt{(G')^2 + (G'')^2}. \quad (3.1)$$

Table 3.2: Properties of the viscoelastic coating used in experiments

Storage modulus G'	1.5 kPa
Loss modulus G''	0.05 kPa
Shear modulus $ G^* $	1.5 kPa
Density ρ_c	862 kg/m ³
Shear wave speed C_t	1.31 m/s

3.4.2. Casting and maintenance

A 5 mm thick viscoelastic coating was manufactured on top of a 10 mm thick high-temperature (150°C) resistant polycarbonate plate. The coating plate was designed in the shape of a tray such that the coating is contained inside when in liquid form.

The coating plate preparation procedure is shown in Figure 3.4. Solidified coating in a beaker at room temperature was put into an oven and the coating was melted to a liquid form at 110°C. Maintaining this temperature for 30 minutes ensured that the coating was fully melted. Any impurities were taken out of the melted coating with a clean spoon and the liquefied solution was poured into the polycarbonate plate mould and weighed with a scale. A levelling tool was used to ensure that the coating plate is levelled such that the coating thickness is more or less homogeneous, as a variation in coating thickness would cause biases in the results.



Figure 3.4: Coating casting process showing the solidified coating in a beaker and the melted coating in a polycarbonate plate mould inside the metal tray

While not used in water, the coating was maintained in an enclosure in air to prevent contamination from impurities and dust in the surroundings. Although this method was proven quite robust for the duration of the experiments, potential deterioration of the surface quality and homogeneity due to impurities or breakage was seen to be reversible through remelting of the coating. A comparison of the coating before and after the remelting procedure is shown in Figure 3.5.

For the experiments, the coating plate was mounted on an aluminum structure underwater. A dot pattern was secured to the backside of the coating plate. When in water, some minimal oil leaking was observed with no appreciable effects on imaging quality or coating properties, although the latter could be more systematically quantified in future studies. In addition, air bubbles that form on the coating underwater need to be removed as much as possible before starting a new experiment as they appear as optical irregularities/bright spots in the deformation quantification images, amplifying/obstructing the dot pattern behind them.



Figure 3.5: Damaged coating surface before and after remelting

3.5. Measurement of coating deformation with FSSS

The FSSS method from Moisy et. al [29] was modified to quantify the deformation of the compliant coating surface underwater. The experimental setup of the FSSS technique consists of a surface, in this case, the coating surface underwater, a random dot pattern, a digital camera, and an LED for background illumination. Figure 3.6 shows the arrangement of the components of the FSSS setup and Figure 3.7 specifies the most relevant distances between these components. In addition, Figure 3.7 also shows the x, y, z axes as defined. In the coating plane ($y-z$), the horizontal and vertical displacement fields are denoted as $V(y, z)$ and $W(y, z)$. The coating surface height field is denoted as $H(y, z)$, which is measured in the x direction, normal to the plate. The velocity components in the x, y, z direction are denoted as u, v, w , while u_e is the jet exit velocity.

Each of the experimental components as well as the processing and post-processing methods are further described in detail in the following sections.

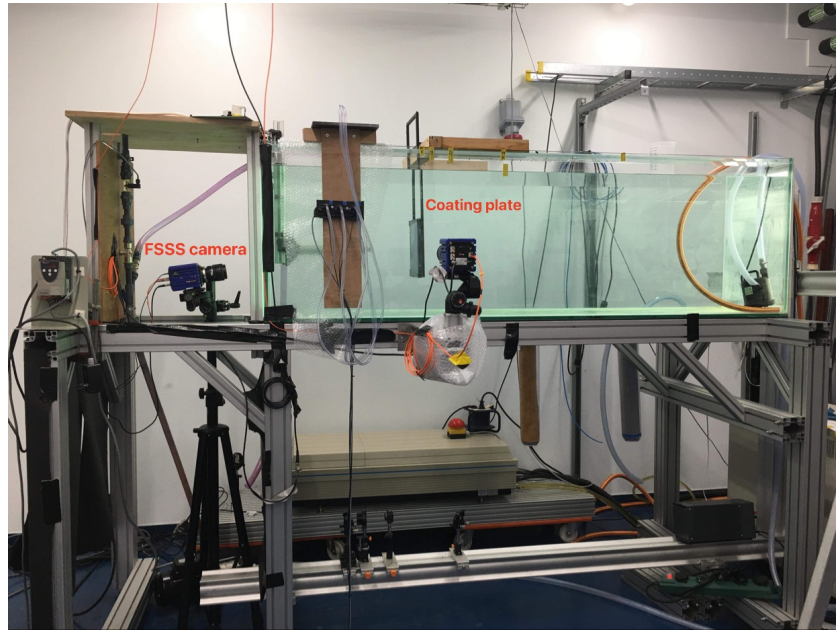


Figure 3.6: Experimental setup for the FSSS experiments

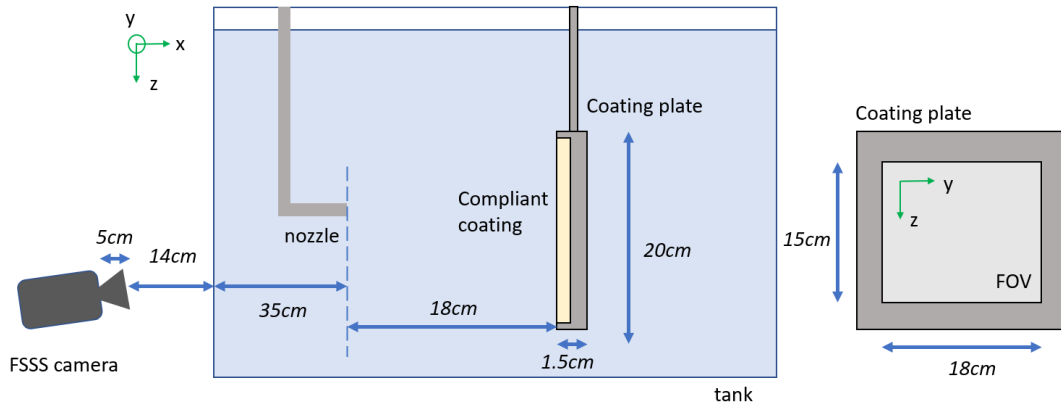


Figure 3.7: Locations of key components and important dimensions

3.5.1. Optics selection and placement

The camera used was a 5MPx PCO SCMO Edge 5.5 with a sensor size of 13.3 mm by 13.3 mm, a resolution of 2560 px by 2160 px and a pixel size of $6.5 \mu\text{m}$ by $6.5 \mu\text{m}$. Since there was limited space for the placement of the camera and its support structure, an appropriate lens was needed to ensure the field of view can be in focus.

First, the magnification number M was calculated to be 0.074 using the FOV and the sensor size. The object distance s_o is then related to the focal length and magnification number:

$$s_o = (1 + M^{-1})f. \quad (3.2)$$

The object distance is equal to approximately 73.5 cm according to the position of the camera and the dimensions indicated in Figure 3.7. This suggests that a lens with a focal length of 50 mm is suitable for

capturing the entire FOV with a slightly adjusted focus.

As discussed in Section 2.2.2, FSSS uses the paraxial/small angle approximation which requires a sufficiently large dot pattern-camera distance h_{cp} when compared to the field of view such that the maximum paraxial angle satisfies Equation 2.7. A β_{max} value of 0.17 is obtained with the distances specified in Figure 3.7. Therefore, the paraxial approximation is valid. Additional factors that may influence the validity of FSSS results are discussed later in Section 3.7 as they rely on posterior evaluations.

3.5.2. Background dot pattern

The generation of a suitable random dot pattern follows a few rules of thumb according to Moisy et al [29]:

- The particle image diameter should be between 1.3 pixels and 4 pixels
- The number of particles per square pixel should be between 0.02 and 0.2

Given the dot diameter (D) and the number of dots (N_d) as input, a MATLAB program based on the original code "makebospattern.m" [34] by Moisy generates a pattern in the desired field of view based on the camera characteristics. The initial values of D and N_d were chosen based on rough calculations following the rules of thumb mentioned above. The code judges whether the input parameters satisfy the rules of thumb, and compute the main characteristics of the dot pattern such as the number of particles per interrogation window for a range of window sizes.

Initial tests show that patterns with a black background and white dots provide better contrast for the dots as when the light goes through a white background, diffusion makes the dots appear smaller and the boundary less clear. To assess the effect of window size and particle density on the FSSS results, experiments were conducted using the dot patterns shown in Table 3.3 and the results were compared. The same flow was used throughout these dot pattern experiments.

Table 3.3: Parameters of the dot patterns tested. Table coloured according to criteria on particle image diameter and particle image density by Moisy et al. [29], green = satisfied, red = not satisfied

	D (mm)	N_d	Window size (px)	Dot diameter (px)	N_d/pixel^2
DP1	0.3	2×10^5	16	3.6	0.13
DP2	0.15	8×10^5	12	1.8	0.52
DP3	0.6	5×10^4	32	7.2	0.03
DP4	0.3	4×10^5	16	3.6	0.25

Example displacement fields obtained from each dot pattern are shown in Figure 3.8. *DP2* has the highest spatial resolution as it was designed for the smallest window size. However, it is most susceptible to noise due to potential dot pattern movements or vibrations, which are likely to be larger at a higher jet velocity. All four dot patterns were able to capture the propagating wave-like structures emanating from the jet impact point. Further systematic studies are required to generate the optimal dot pattern for a certain measurement scenario which is beyond the scope of this project.

Overall, the selection of dot patterns involves balancing resolution and noise as competing criteria. In the end, *DP1* was chosen for the FSSS experiments as it satisfies all the criteria mentioned above by

Moisy et. al [29], although the other dot patterns tested are likely to provide a similar result as long as the displacements of the dots can be captured properly by the DIC algorithm.

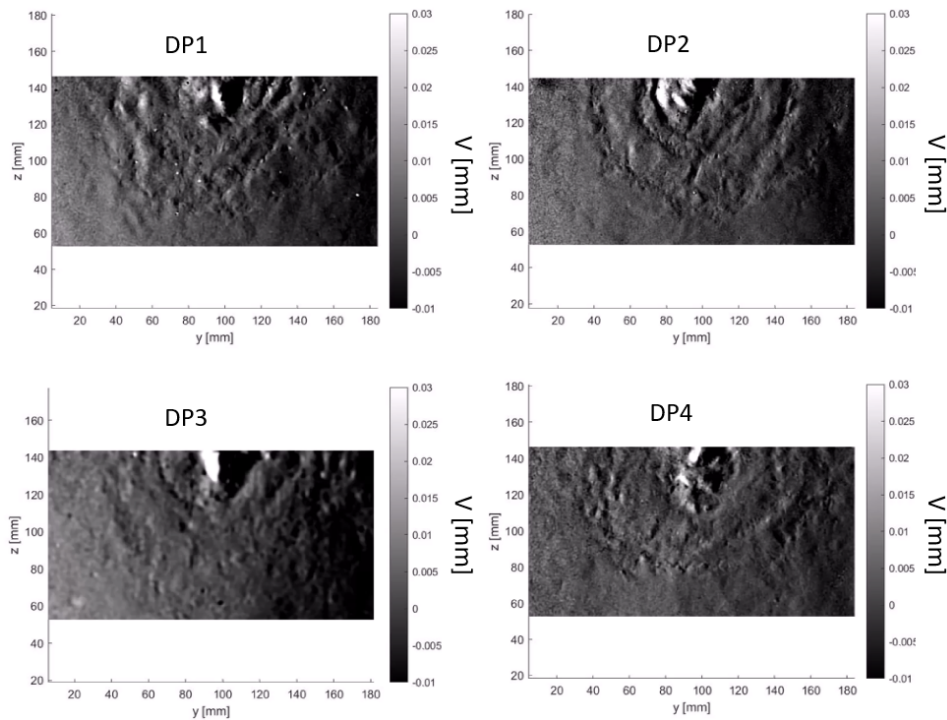


Figure 3.8: Example instantaneous displacement fields obtained using the dot patterns in Table 3.3.

3.5.3. Calibration

Camera calibration is required for the correct calculation of dot displacements and thus the reconstruction of the coating surface and the extraction of pressure fluctuations, especially considering that the camera was placed at a tilted angle due to space constraints. It is also crucial for mapping the known sensor locations to the camera images.

The FSSS camera field of view was calibrated when the jet was off using a custom-made calibration pattern that was printed on a transparent plastic sheet and fixed in place between the coating plate and another polycarbonate plate on the back. The calibration pattern was positioned at exactly the same location as the random dot pattern used in the FSSS experiments.

The custom-made calibration target has a size of 16 cm by 16 cm and consists of a 2D dot array. Each row and column of the array has 20 dots each with a diameter of 5 mm. The spacing between two adjacent dots is 8 mm. The calibration target and its position in the flow facility are shown in Figure 3.9.

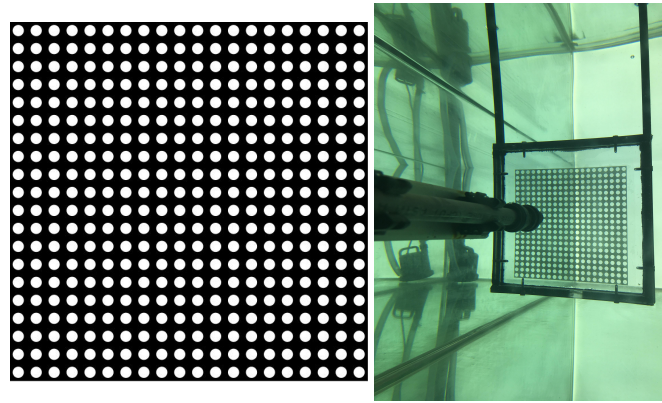


Figure 3.9: FSSS calibration target and its position in the flow facility

It was assumed that the calibration plane was identical to the measurement plane in the jet-on scenario as testing did not show any plate displacement due to jet impact. The FSSS results would later suggest that this might not have been the case. The misalignment of the calibration focus plane and the dot pattern plane could introduce additional uncertainties in the displacement field.

3.5.4. Image acquisition

The coating plate was placed at the same nozzle-to-plate distance of 18cm for all the experiments, maintaining a constant field of view. The jet velocity was varied to generate pressure fluctuations of different magnitudes in the flow. The FSSS setup was shown previously in Figure 3.6. During experiments, an LED lamp illuminated the transparent coating plate from the back of the water tank. The dot pattern was placed between the coating plate and a support plate to prevent its movement which could result in erroneous displacement vectors. The FSSS camera was placed in front of the water tank, pointing slightly upward towards the coating plate to prevent a significant portion of the field of view from being blocked by the jet nozzle structure. It is, however, inevitable that the jet creates a shadow in parts of the field of view. The section of the field of view affected by the shadow was removed during post-processing. Although the line-of-sight of the camera goes through part of the jet, it has no impact on the results. Since the water tank is recirculating, there is no significant thermal gradient between the jet and the surrounding water that could affect light propagation properties.

An image acquisition rate of 50 Hz was used which is the maximum rate for the low-speed camera. There is a slight (<10 mm) side-to-side movement of the jet due to its position instability. Therefore, a sufficient number of statistically independent snapshots are required to ensure convergence in the statistics. Figure 3.10 shows the convergence behaviour of the RMS values of the horizontal displacement V_{rms} at a fixed point in the FOV for the lowest and highest jet velocity cases. 2000 images were taken for each test case to ensure convergence is achieved.

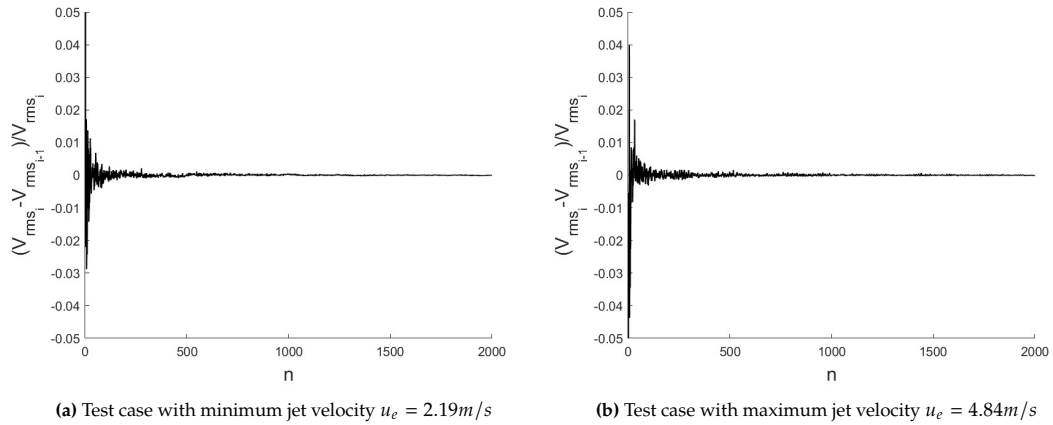


Figure 3.10: Convergence of the horizontal displacement V at a location near the jet impact point

3.6. FSSS Processing and post processing

In this section, the processing and post-processing procedures used to extract pressure fluctuations from FSSS snapshots are described. An overview of the workflow used for obtaining the results in Chapter 4 is presented in the flowchart in Figure 3.11, which involves generating displacement fields, calculating surface gradients, integrating surface gradients to obtain surface height fields and finally, converting surface height fluctuations to pressure fluctuations. Each step will be explained in detail in this section. A longer version of the flowchart with additional steps for further processing the displacement field is included in Appendix A but is not applied to the experimental data.

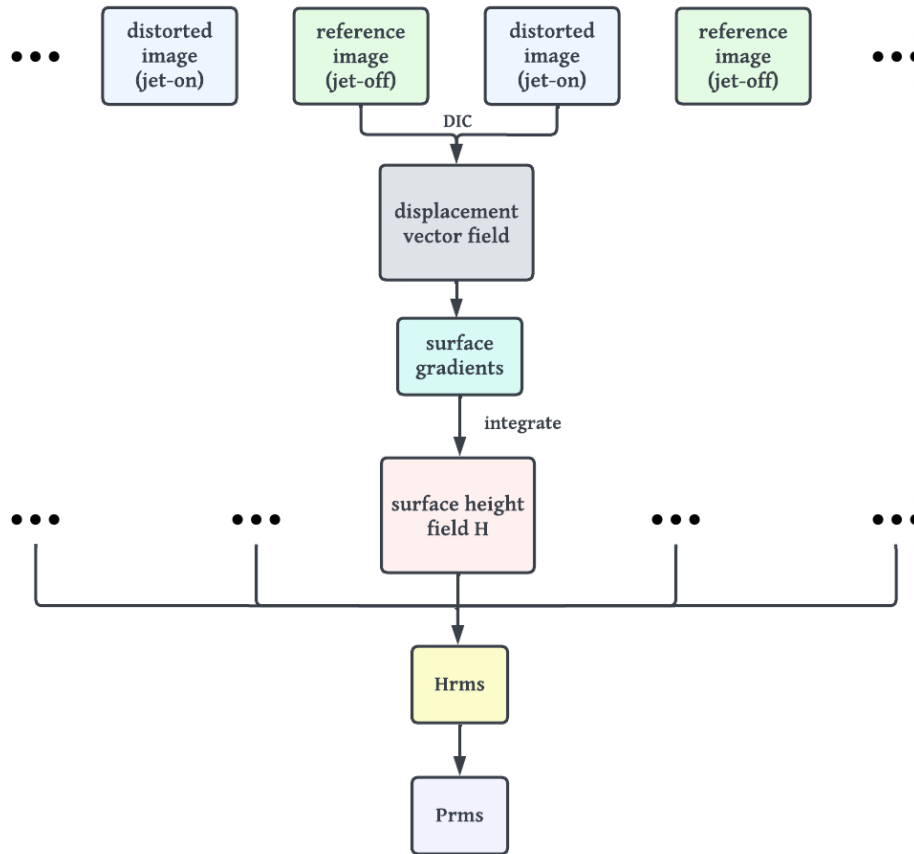


Figure 3.11: Flow chart of processing and post-processing steps

3.6.1. From dot patterns to displacement field

First, the reference images of the dot pattern when the jet was off and images of the distorted dot pattern when the jet was on were merged into a multi-frame dataset, where the reference image was added in between every two successive distorted dot pattern images. The merged dataset was then fed into the PIV vector processing routine in Davis which calculates the apparent displacements of the dot pattern in the y and z directions (V , W) due to the deformed coating surface at each instance in time using a DIC algorithm. A window size of 16 px by 16 px with 50% overlap was used as the final pass, as the dot pattern was designed for this window size. This gives a uniform vector spacing of 0.28 mm. The FSSS acquisition parameters are summarized in Table 3.4.

Table 3.4: FSSS acquisition parameters

Field of view	180 mm × 150 mm
Magnification number	0.074
Interrogation window size	16 px × 16 px
Overlap	50%
Vector spacing / resolution	0.28 mm
Acquisition frequency	50 Hz
Number of snapshots per test case	2000
Test cases	All cases from Table 3.1

It is important to recall that FSSS is limited to small deformations. For big deformations, an algorithm more robust than DIC is required, such as DTA. This assumption is more likely to be met for the small jet velocity cases where the pressure fluctuations are small. For the large velocity cases and at locations close to the jet impact point, there is potentially a two-way coupling between the flow and the coating which would result in much larger deformations. Whether the small deformation assumption was upheld for the various test cases is evaluated in Section 3.7.2.

3.6.2. Cleaning up the displacement field

In some cases, the displacement field outputs from DIC require further post-processing to ensure their quality.

Cropping out jet shadow

In the raw images, the shadow of the jet was cropped out from the FOV to enhance the quality of the displacement field after processing. Since the coating is considered incompressible (see Section 3.4), any peak has a corresponding trough to balance out the mean surface height as the mean surface height over the entire coating area must be zero. This is not the case when only a part of the coating is included in the final FOV for analysis. However, this is not an issue as will be discussed in the next section, in the case of a non-zero mean surface height, the mean is removed during the integration step as only the fluctuations are relevant to this study. As shown in Figure 3.12, the cropping operation does not have a significant impact on the reconstructed surface height field in the region that remains. Nevertheless, there is a small difference between the cropped and non-cropped results due to the propagation effect of the non-local integration procedure. This shows that cropping is necessary as the jet shadow region would otherwise pollute the rest of the FOV.

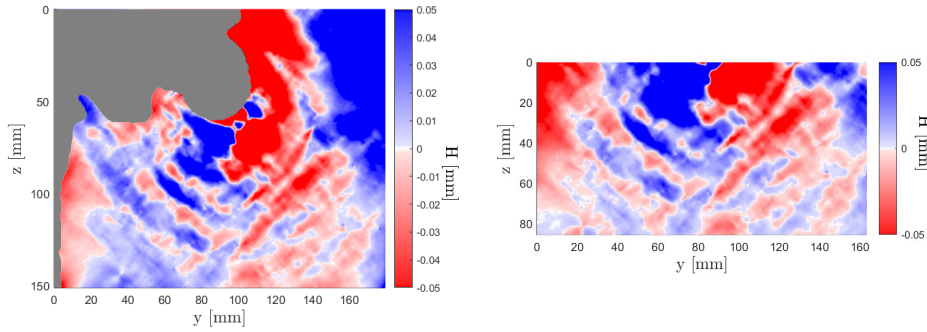


Figure 3.12: Surface height fields showing the effect of processing the entire FOV compared to processing the half without jet shadow. The jet shadow is shown in grey

Additional inhomogeneity removal

Two additional custom operations not included in the flowchart in Figure 3.11 and not applied to the final results were developed and tested to improve the quality of the displacement field. The LINSUB operation is used to remove the time-varying linear background gradients observed by subtracting the 2D planar fit of the displacement field from each individual displacement field image, while the MSUB operation is used to remove non-time varying background inhomogeneity by subtracting the ensemble mean of all the displacement fields. Details on the two operations and their effects can be found in Appendix A.

Figure 3.13 shows that the LINSUB and MSUB operations have minimal effects on the final P_{rms} values, especially near the jet impact point. Furthermore, although the operations effectively removed the background inhomogeneities observed (see Appendix A), a more comprehensive analysis is needed to justify the usage of both operations considering their noticeable impact on the pressure output and the lack of a concrete conclusion for the background displacement inhomogeneities observed. Therefore, for validating the CCPM system, the set of experimental data with the least amount of background inhomogeneities is chosen and the LINSUB and MSUB operations are not applied to the displacement fields used for validating the CCPM technique.

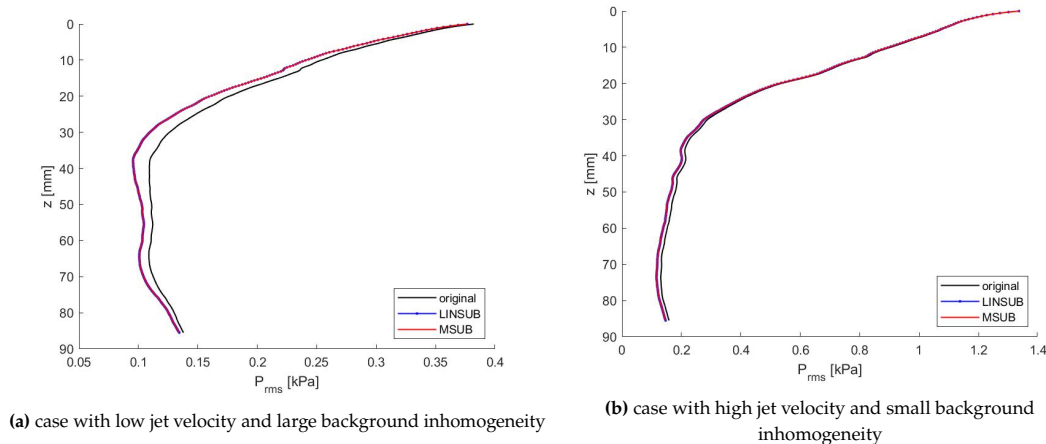


Figure 3.13: Effect of the LINSUB and MSUB operation on P_{rms} on a vertical line extending from the jet impact point to the bottom edge of the field of view

3.6.3. From displacement to pressure

It has been shown in past literature that the dot pattern displacement field can be used to reconstruct the surface height of the deformed coating [3]. The surface reconstruction method originally developed for an air-water interface by Moisy et al. [29] (see Section 2.2.2) was tested by Greidanus [3] for the case of a water-compliant coating interface with small modifications and showed success in reconstructing the coating deformations due to a turbulent boundary layer flow. Therefore, a similar surface reconstruction procedure is applied for the current study involving a water-compliant coating interface with changes due to a different FSSS setup and coating plate construction.

It is known that the slope of surface height is proportional to the displacement field by a factor k [29]:

$$\frac{dH}{dy} = kV \quad (3.3)$$

and

$$\frac{dH}{dz} = kW, \quad (3.4)$$

where the factor k can be determined using the refractive properties and thus the composition of the coating plate and the placement of the camera:

$$k = \frac{1}{h_{cp}} - \frac{1}{\alpha h_0}, \quad (3.5)$$

where α is a ratio of the refractive indices of water n_w and the coating n_c [3], calculated using:

$$\alpha = 1 - \frac{n_w}{n_c}, \quad (3.6)$$

and h_0 is the effective thickness of the coating plate which, in the case of the current experimental setup, is a weighted sum of the coating thickness and the thickness of the polycarbonate plate:

$$h_0 = h_c + (n_c/n_p)h_p, \quad (3.7)$$

where h_c, h_p are the thickness of the coating and the polycarbonate plate and n_c, n_p are the refractive indices of the coating and the polycarbonate plate. The values of experimental parameters used are listed in Table 3.5.

Table 3.5: FSSS parameters relevant to surface reconstruction

h_c	5 mm
h_p	10 mm
h_0	14.3 mm
n_w	1.333
n_c	1.475
n_p	1.59
α	0.096
$ G^* $	1.5 kPa

Integrating the surface height gradients over the vector spacing leads to the reconstruction of the deformed coating surface. The resolution of the surface topology is, therefore, limited by the vector spacing which is 0.28 mm as shown previously. In order to preserve only the fluctuations as the mean spatial pressure cannot be inferred from the surface topology alone, the integration constant (i.e. the mean height) is set to zero. For the remainder of the report (and previously when relevant), surface height is equivalent to surface deformation.

The goal is to compare the CCPM pressure predictions with pressure sensor measurements through the RMS statistics as the jet is turbulent. According to the study on the interaction between compliant coatings and turbulent boundary layers by Benschop et al. [8], the RMS of pressure P_{rms} is linearly related to the RMS of the surface deformation H_{rms} using the following equation which is rearranged from Equation 2.2:

$$P_{rms} = |G^*| \frac{H_{rms}}{0.031h_c}. \quad (3.8)$$

The validity of this scaling for the current case of a submerged impinging jet will be examined through comparison with pressure sensor data.

3.7. FSSS validity

Although FSSS can reach a surface height reconstruction accuracy of 1.5% as shown by Moisy et al. [29], many factors that could compromise the displacement measurements and the surface reconstruction process, leading to a surface height field with much lower accuracy. Therefore, a few a posteriori checks are necessary to evaluate the validity of the results.

3.7.1. Ray crossing

As mentioned in Section 2.2.2, ray crossing can occur for large surface-to-pattern distances or large surface curvatures, causing artificial magnification.

To avoid ray crossing, the surface-pattern distance h_{sp} needs to satisfy the condition in Equation 2.8, where the α value from Table 3.5 is used. Using the worst-case scenarios, a minimum wavelength of approximately 7 mm and a maximum amplitude of 0.2 mm can be extracted from the results later shown in Section 4.2. Equation 2.8 then gives a minimal critical surface-pattern distance $h_{0,c}$ of approximately 65 mm. In the case of the experiments, a surface-pattern distance h_0 of 14.3 mm was used which is much smaller than $h_{0,c}$. Therefore, ray crossing would not have occurred.

3.7.2. Image strain

It was pointed out in Section 2.2.2 that FSSS does not work for strong curvature even when ray crossing is not present, as it would result in non-circular dots. Moisy et al. [29] suggested using the strain of the displacement field as an evaluation criterion.

A strain check was, therefore, performed on the displacement field in the y and z direction, with the largest absolute principal strain field σ^* calculated using:

$$\sigma^* = \max(|dV/dy|, |dW/dz|). \quad (3.9)$$

where σ_{rms}^* in the appropriate coordinate is:

$$\sigma_{rms}^* = \sqrt{\frac{1}{N_y N_z} \sum_{y,z} \sigma^{*2}(y, z)} \quad (3.10)$$

where N_y and N_z are the numbers of displacement vectors in the y and z directions.

The results of all the test cases are shown in Figure 3.14, where each dot represents a snapshot and each colour represents a test case with a different jet velocity. The threshold of 0.15 is not exceeded by a single snapshot for any of the test cases, therefore, the displacement fields can be assumed to have sufficiently small curvature.

A more detailed examination shows that the highest jet velocity case has the highest strain, indicating the highest curvature in the image field as expected. In general, the higher the jet velocity, the higher the strain, with the exceptions being case $u_e = 3.87$ m/s which has the second highest strain despite having the fourth highest jet velocity, and the second highest jet velocity case $u_e = 4.58$ m/s has only the fourth highest strain. Further analysis is required to identify the cause behind these outliers.

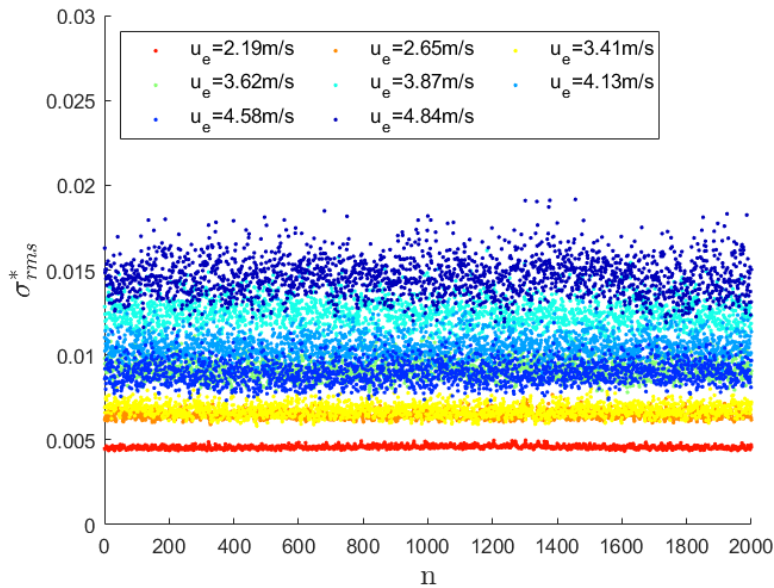


Figure 3.14: σ_{rms}^* values of each test case for all snapshots

3.7.3. Uncertainties

Dot pattern displacement measurement

It was discussed previously that the uncertainty of the displacement measurements depends mostly on the DIC algorithm. In the current case, the DIC algorithm part of the PIV processing routine in Davis is used. For the case with the highest jet velocity, in the region near the jet impact point, uncertainty computation in Davis shows that the displacement field has an uncertainty of around 0.005 mm for a displacement of around 0.05 mm. This gives a relative uncertainty of 10%. The lowest jet velocity case gives a relative uncertainty of about 30%.

These are, however, optimistic estimates assuming no plate displacement or other outstanding

circumstances such that the noise is correlated. The real uncertainty in the displacement fields is unknown and likely larger. This is to be determined in future investigations.

Surface reconstruction

According to the empirical law obtained by Moisy et al. [29] in Equation 2.5 and using the parameters in Table 3.6 below, a relative uncertainty in surface deformation of the order 10^{-3} is obtained. A wave of amplitude 0.05 mm should therefore have an absolute uncertainty of around $50 \mu\text{m}$ to $100 \mu\text{m}$. The error in surface height does not blow up with displacement field uncertainties thanks to the grid size. However, as mentioned in Section 2.2.2, the resolution of surface reconstruction is limited to h_0/h_{cp} (2%) without remapping due to parallax distortion. As P_{rms} can be obtained by multiplying H_{rms} by a constant using Equation 3.8, the relative uncertainty remains the same and is small enough to be negligible when aiming at an order-of-magnitude accuracy.

There are, however, likely larger sources of uncertainties. For example, the error due to the integrated background displacement gradients cannot be quantified using Equation 2.5 as it only applies to uncorrelated noise in the displacement field. However, once the LINSUB operation is validated, the error can be estimated from Figure 3.13a to be much larger than 2% for cases with large background gradients. These larger sources of uncertainties require further identification and quantification in future studies. For the validation results, the test sets with the least amount of background displacements were chosen which should not introduce additional large uncertainties to the pressure output, as shown in Figure 3.13b.

Table 3.6: Parameters for calculating the uncertainty of surface reconstruction

L	18 cm
N_g	586
λ	10 mm
ϵ	0.1-0.3

3.7.4. Maximum deformation vs coating thickness

A coating with a specific thickness has a limit on how much it can deform, and thus the amount of actual deformation/pressure it can capture. A thicker coating with the same material properties has the capacity to deform more. In the case of a head-on impact such as the impinging jet, a thicker coating might resolve more depth and as a result, indicate a higher pressure fluctuation. This limitation on deformation itself is different from the limitation on the measurement of the deformation using FSSS, which has been assessed using the image strain in Section 3.7.2.

For a turbulent boundary layer, Greidanus [3] suggested that coating thickness only has an effect on coating deformation for thin coatings $h_c < \delta_v$, in which case deformation increases linearly with coating thickness. For the case of an impinging jet, it is unclear whether there is a threshold for sufficient thick coatings such that when the threshold is exceeded, thickness no longer affects coating deformation. The coating deformations at the jet impact point in contrast to the thickness of the coating for all jet velocity cases are shown in Figure 3.15. The ratio H_{rms}/h_c spans a range from 0.002 to 0.022. This implies the maximum deformation magnitude is less than 3% of the coating thickness. Therefore, it can be assumed that the coating is sufficiently thick that it can fully resolve the deformations.

From the literature, Figure 2.6 suggests that a H_{rms}/h_c ratio of more than 0.005 falls within the

two-way coupling region for a turbulent boundary layer flow [3]. Analysis in the following chapter will investigate whether this holds for the impinging jet in this study and whether a deformation-based threshold can be established for the coupling regimes.

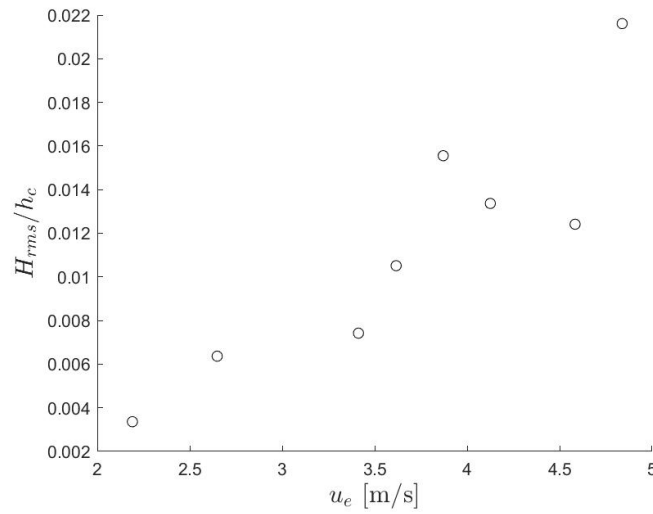


Figure 3.15: H_{rms} at jet impact point scaled with coating thickness for all jet velocity cases

3.8. PIV

2D planar particle image velocimetry was used to quantify the flow field in the vicinity of the coating plate as it can provide accurate statistics of the flow field near the coating. Flow field data obtained from PIV near a rigid plate and the coating plate are compared to evaluate the impact of coating deformation on the surrounding flow.

An image of the PIV setup and an illustration showing the key dimensions are shown in Figure 3.16. The PIV camera was placed 40 cm away from the centre plane (x-z). The same camera and lens as the ones used for FSSS were used for PIV with adjusted focus. A laser sheet was positioned in the x-z plane, pointing upward at an angle towards the coating plate such that the region of the laser sheet with the highest intensity overlapped with the field of view. The positions of the PIV camera and the laser sheet are shown in Figure 3.16.

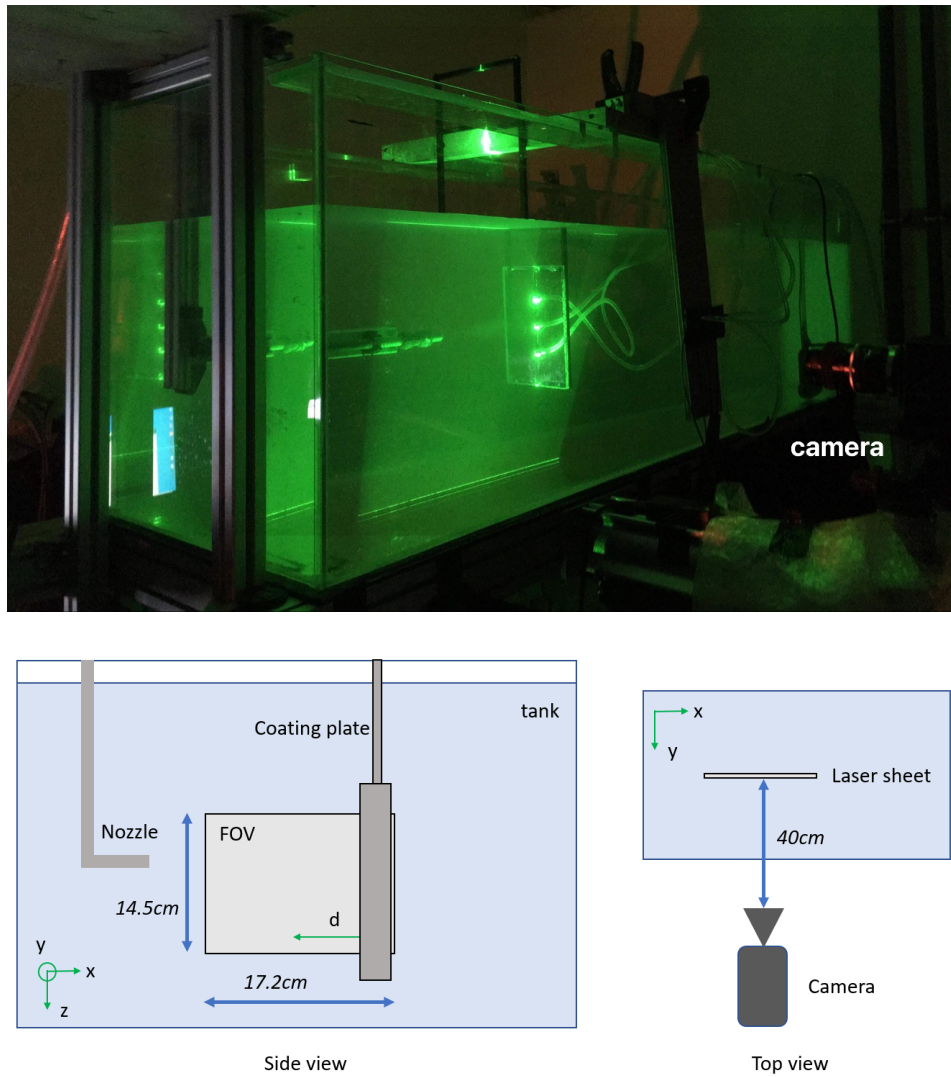


Figure 3.16: PIV setup showing camera and laser sheet positions and key dimensions

As shown in the illustration in Figure 3.16, the relative distance from the impinging plane d is defined as:

$$d = x_0 - x \quad (3.11)$$

where x_0 is the position of the coating/plate surface.

The PIV acquisition parameters are summarized in Table 3.7. The acquisition frequency was chosen as 5 Hz as this allows the majority of the particles to exit the field of view before the next snapshot is taken, ensuring the snapshots are statistically independent. PIV experiments were only conducted for 4 of the 8 jet velocities tested in the FSSS experiments as the goal of the PIV experiments is to capture a shift in coupling regime if any. Preliminary FSSS results showed that a distinction in wave appearances can be made for the cases with $u_e \leq 3.41$ m/s and the cases with $u_e \geq 3.87$ m/s. Therefore, the jet velocities listed in Table 3.8 were chosen for the PIV experiments.

A window size of 16 px by 16 px with a 50% overlap was used, which gives a uniform vector spacing

of 0.54 mm. A different duration between laser pulses (dt) was used for each test case to ensure a particle displacement of 5-7 pixels in the region of interest near the plate despite the differences in jet velocities between the cases. The uncertainties on the mean and RMS statistics were obtained from Davis. An ensemble size of 3000 was used for which the streamwise and radial velocity components for the lowest and highest jet velocity cases all converged to less than 1%, as shown in Figure 3.17 and 3.18.

Table 3.7: PIV acquisition parameters

field of view	172 mm \times 145 mm
Magnification number	0.077
Interrogation window size	16 px \times 16 px
Overlap	50%
Vector spacing / resolution	0.54 mm
Acquisition frequency	5 Hz
Number of snapshots per test case	3000
Test cases	$u_e = 2.65$ m/s, $u_e = 3.41$ m/s, $u_e = 3.87$ m/s, $u_e = 4.58$ m/s
Mean velocity uncertainty	max 0.005-0.007 m/s for $d < 15$ mm for all test cases
RMS velocity uncertainty	max 0.003-0.005 m/s for $d < 15$ mm for all test cases

Table 3.8: Pump flow rates and jet velocities of the test cases

Pump flow rate (L/s)	0.052	0.067	0.076	0.090
Jet exit velocity (m/s)	2.65	3.41	3.87	4.58

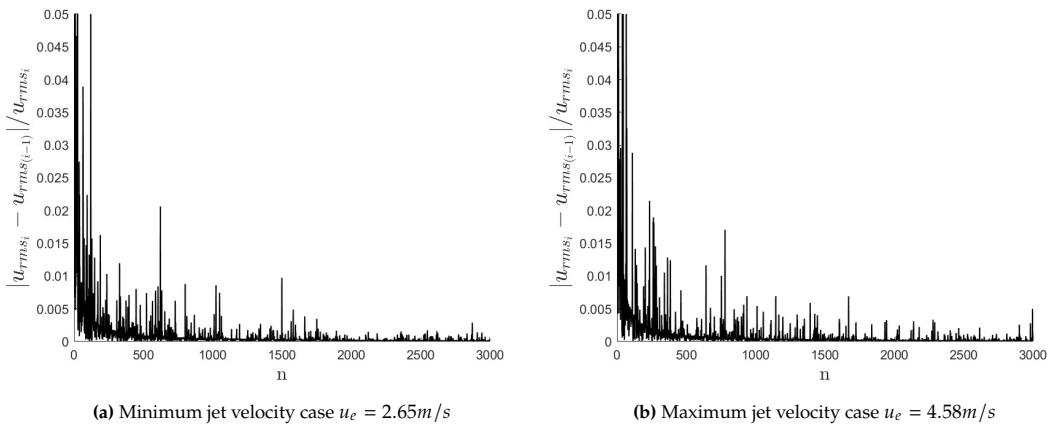


Figure 3.17: PIV u_{rms} convergence with the number of snapshots

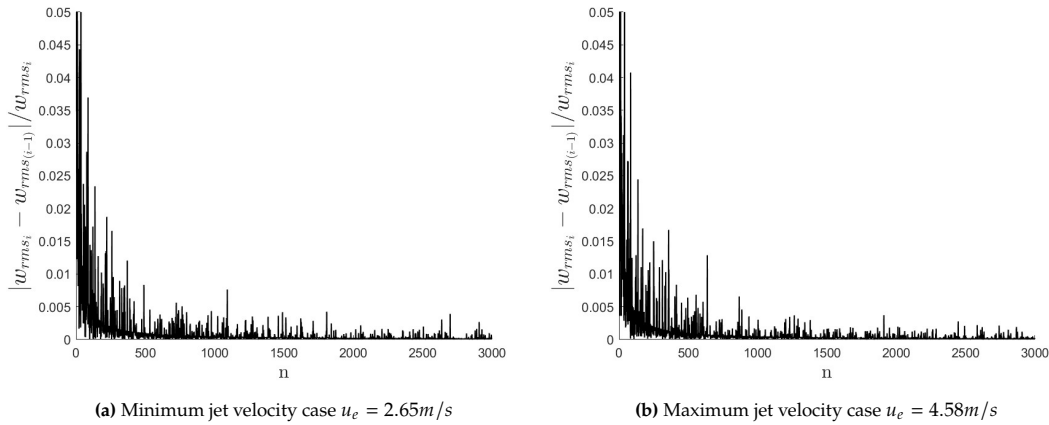


Figure 3.18: PIV w_{rms} convergence with the number of snapshots

3.9. Pressure sensors

For validation purposes, three point-wise pressure sensors were used to obtain reference pressure fluctuations in the same measurement plane as the coating surface. It is important to note that, for this validation experiment, the highest measurable accuracy of the CCPM technique is limited by the accuracy of the pressure sensors.

The pressure sensor array consists of three identical Honeywell gauge pressure sensors with a maximum pressure reading of 0.5 psi (3.4 kPa), selected based on maximum values measured during initial testing. It has an accuracy (linearity) of $\pm 0.25\%$ of the full range (8.5 Pa) and a response time of 1 ms. The sensors have a theoretical resolution of approximately 3 Pa. However, due to electrical noise induced by the pump and other environmental elements, in reality, the sensors have a resolution of approximately ± 30 Pa. The sensors were positioned at different radial distances, 0 cm, 1.5 cm and 2.5 cm, with respect to the nominal jet centre in the measurement plane which is 18 cm away from the nozzle exit. The spacing between sensors is limited by the diameter of the connector. The inner diameter of the sensor hole is 5 mm, meaning the data captured by the sensor is averaged over the area of a circle with this diameter. The physical locations of the sensors relative to the jet impingement region are shown in Figure 3.19a. The locations of the sensors are mapped to the FSSS images through FSSS calibration data as shown in Figure 3.19b. Note that although one sensor was physically placed above the jet impact point (see Figure 3.19a), its location in the FSSS image was reflected onto the lower half of the FOV as its actual location in the top half of the FOV falls in the jet shadow region which was cropped out during FSSS post-processing. It was assumed that the FSSS statistics at the reflected location should not be very different from the real location as the jet should be more or less axisymmetric. The sensor tubes were connected to a polycarbonate plate through flush-mounted connectors on one end and plugged into the sensor input ports placed outside of the water tank on the other end.

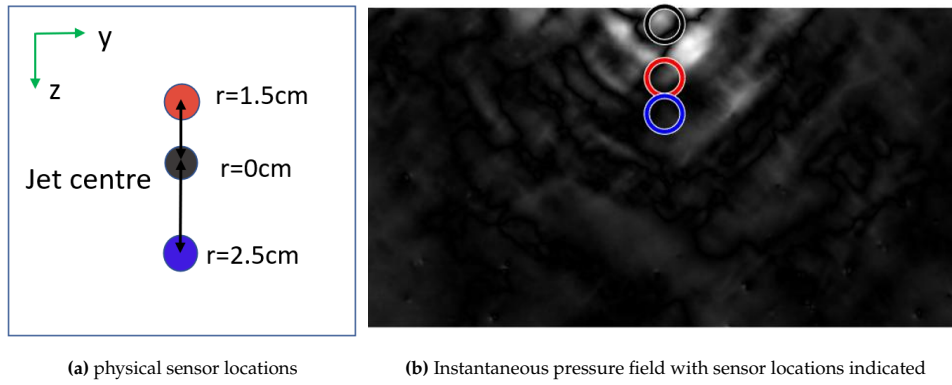


Figure 3.19: Physical locations of the pressure sensors and the locations at which the pressure data was extracted from FSSS, sensors corresponded by colours

A Validyne T-140 pressure calibrator kit was used to extract the pressure-voltage curve for each sensor. A linear fit of the calibration curves, shown in Figure A.9 in Appendix A, was used to convert sensor output voltage measurements to pressure.

The voltage measurements with the jet off were manually subtracted from the jet-on measurements to account for the different hydrostatic pressure at each sensor location, such that the correct pressure footprint on the sensor plate is measured when the jet is turned on. The jet-off measurement only measures the static pressure:

$$P_{off} = P_{stat}, \quad (3.12)$$

where P_{stat} is the absolute static pressure when there is no flow, while the jet-on measurements include the dynamic pressure due to the jet:

$$P_{on} = \frac{1}{2}\rho u^2 + P'_{stat} - P_{off}, \quad (3.13)$$

where P'_{stat} is the jet-on static pressure and is smaller than P_{stat} due to flow.

An acquisition rate of 50 Hz was used and a convergence study was conducted at the lowest jet velocity to determine the duration of sample time required. The convergence plots for the lowest and highest jet velocity cases are shown in Figure 3.20. A sample size of 2500 was used for which the measurement value of the sensor furthest from the jet impact point converges to within 0.5%.

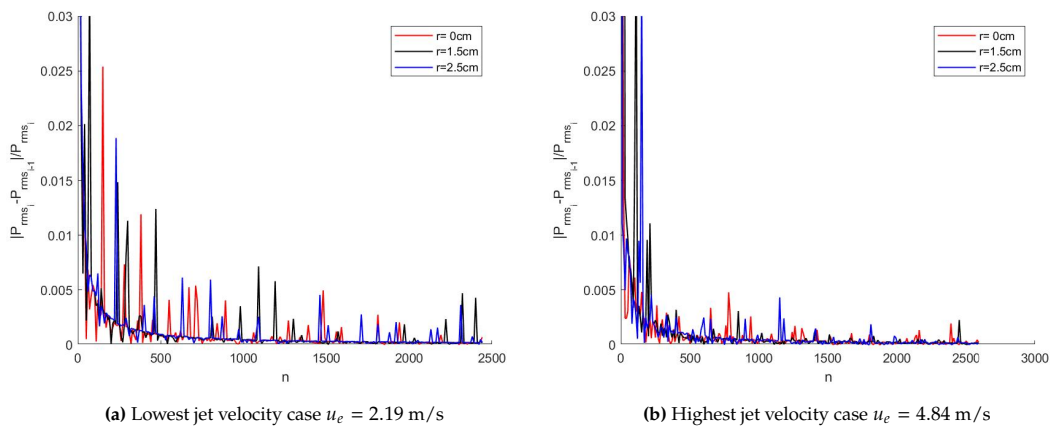


Figure 3.20: Convergence of P_{rms} with the number of samples for all three sensors, plotted in increments of 10 samples

Since the RMS values of the pressure measurements are used for comparison with CCPM, it is necessary to quantify the effect of sensor resolution on the deviation of the measured RMS values from the true RMS value in the case of perfect sensors. The measured data shows approximately a normal distribution between P_{min} and P_{max} for each sensor, as shown in Figure 3.21. A simulation is conducted where a truncated normal distribution between P_{min} and P_{max} is used to represent the data gathered by an ideal sensor with perfect resolution. The ideal pressure distribution is then corrupted with a normal distribution with a standard deviation of 30 Pa, representing the sensor resolution of ± 30 Pa in reality. The results show that there is a less than 2% increase in RMS for all three sensors. Therefore, the effect of sensor resolution on the RMS values is assumed to be negligible.

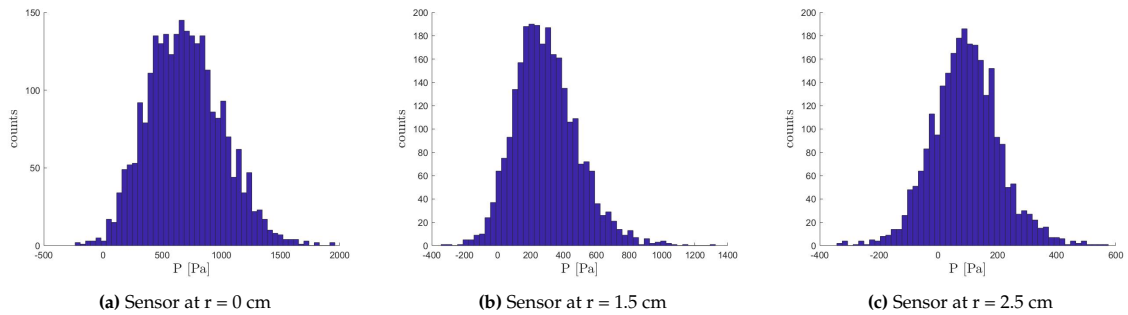


Figure 3.21: Pressure distribution histograms for the three sensors

4

Results

In this chapter, results from test cases with different jet velocities are analyzed and compared to gain insights into the behaviour of the coating under pressure fluctuations induced by the impinging jet flow.

4.1. Effect of jet velocity on coating deformation

The displacement fields of the random dot patterns were successfully extracted by the DIC algorithm in Davis. One example horizontal displacement field for each of the test cases is shown in Figure 4.1. The jet creates ring-like footprints on the coating surface, distorting the dot pattern when viewed by the camera. Only a section of the field of view (18 cm by 8.5 cm) is shown as the rest contains an inevitable jet shadow and has been cropped out as discussed in Section 3.6.2. The rings originate from the jet impact point and expand in the radial direction towards the boundary of the coating plate. At lower jet velocities ($u_e < 3$ m/s), it appears that the rings could not travel far from the jet impact point before being completely dissipated. As the jet strength is increased, the displacement at the jet impact point becomes higher, causing the expanding ring to reach a further and further distance from the jet impact point while maintaining a measurable amplitude.

For a more direct look at what is happening to the coating, one must look at the surface topology of the deformed coating. Examples of the reconstructed surface height fields (with the mean height subtracted) for each of the test cases are shown in Figure 4.2. The LINSUB operation described in Appendix A.1 was applied to the displacement fields in Figure 4.1 before integration to obtain Figure 4.2. However, note that this operation was only applied here to reveal the wave structures in surface height that would be otherwise masked by noise due to background displacement gradients. This operation was not applied for the rest of the analysis including the pressure results used for validation in Section 4.3. It is clear that for the higher jet velocity cases ($u_e > 3.5$ m/s), the wavefronts further from the jet impact point maintain a measurable amplitude, while the wave amplitude decays quickly in the radial direction for the lower jet velocity cases. For the lowest jet velocity cases ($u_e < 3$ m/s), no significant surface height was captured at the jet impact point and no high-amplitude ring-like wave structures can be observed from the surface topology. Although there are possibly small-scale waves present, they might not be resolved as the spatial resolution is limited by the interrogation window and

the resolution in amplitude is limited by parallax distortion.

Overall, the displacement and surface height results showed that the CCPM technique is able to capture the large-scale structures in the coating due to pressure fluctuations induced by an impinging jet, and can reconstruct the amplitude of those structures.

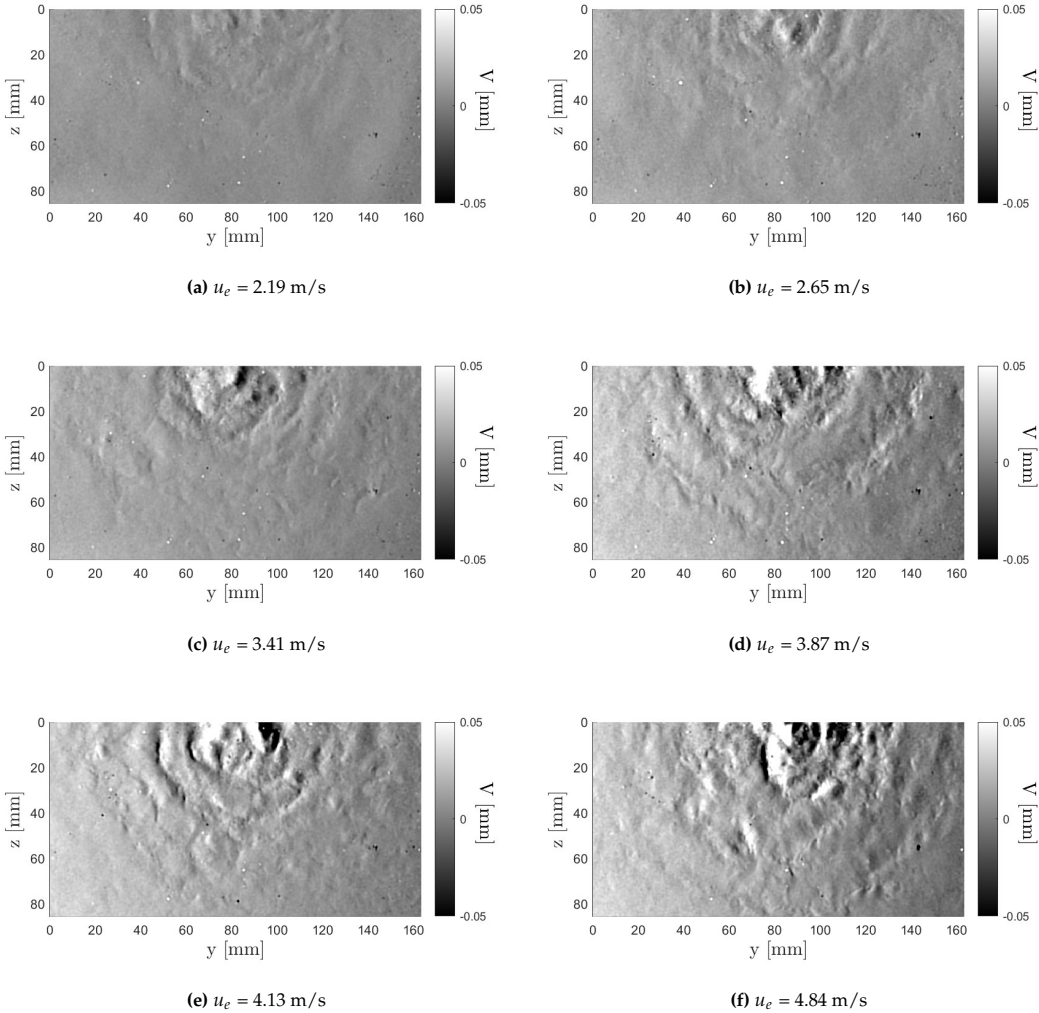


Figure 4.1: Example displacement fields from selected cases of increasing jet velocity

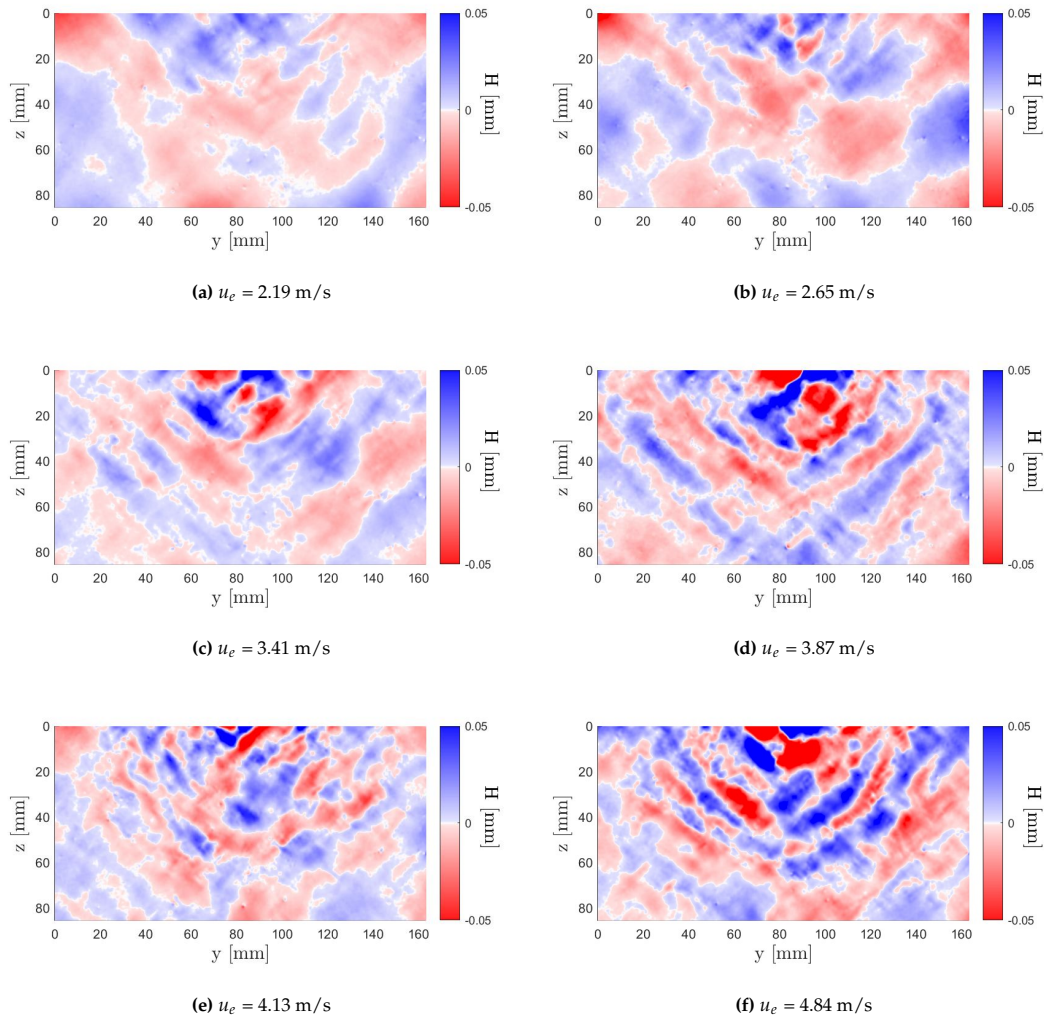


Figure 4.2: Example instantaneous surface height fields from selected cases of increasing jet velocity.

4.2. Wave characteristics

It was observed that the pressure footprint from the jet impingement propagates outwards in the shape of circular waves. In this section, the characteristics of the waves are analyzed. Although similar waves are observed in the surface height fields, the displacement fields are used for analysis as the waves are clearly visible whereas the surface height fields contain integrated background displacement gradients that, although has little impact on the P_{rms} as shown in Section 3.6.2, makes the waves difficult to identify clearly. The horizontal displacement fields are used but the vertical displacement fields would give similar results as the physical wave structures affect measured quantities in both directions in a similar manner.

4.2.1. Propagating wavefronts

While examining the test cases, it was observed that for the cases with higher jet velocities, the ring-like wavefronts in the displacement field transition from a circular shape to an angular shape while

propagating outwards from the jet impact point. It was hypothesized that this phenomenon is due to the interaction of an outward-travelling wavefront with waves that are reflected back from the plate boundary.

Therefore, a separate FSSS experiment was conducted to examine the propagation of one wavefront by quickly turning up the jet. Although the jet has a small finite ramp-up time, the effect of possible boundary reflections of large magnitudes on the outward-travelling wavefronts is removed. As shown in the displacement field time series in Figure 4.3, the wavefronts are circular near the jet impact point, but transition to straight lines angled at $\pm 45^\circ$ at a certain radial distance away from the jet impact point. Furthermore, it was observed that the wavefront transitioned to straight lines when parts of the ring reached the plate boundary.

It is hypothesized that as a part of the wavefront hits the plate boundary, the energy within that section of the wavefront is transferred to the boundary along the plate edge as it follows the direction of least resistance. Therefore, near plate boundaries, only the part of the wavefront furthest from the plate boundary that travels along directions at $\pm 45^\circ$ relative to the x direction remains, making the wavefront appear angular. The hypothesis that this is due to boundary reflections does not hold as there were no waves of significant magnitude initiated prior to this first wavefront. However, there were smaller amplitude waves that were initiated during the ramp-up time which could still reflect from the boundary and interfere with the out-going wavefront if they are not fully dissipated before reaching the coating boundary.

A closer look at one ring-like wavefront in Figure 4.3 shows that the ring is broken up into small structures, similar to the way turbulent spots form in the case of a boundary layer during the laminar-to-turbulent transition. This is likely due to the turbulent nature of the jet.

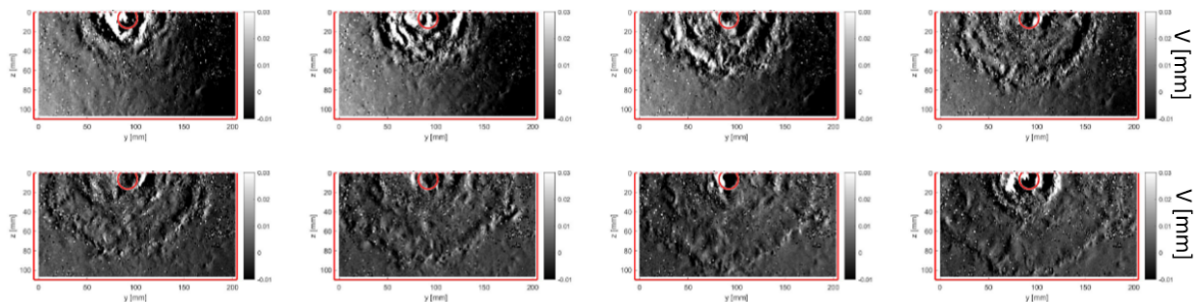


Figure 4.3: Horizontal displacement fields showing a propagating wavefront. The jet impact point and the plate boundaries are marked in red

4.2.2. Wavelength and wave amplitude

When the jet is on for a continuous period as in the case of the FSSS and PIV experiments, the wave properties change when propagating outward from the jet impact point, as the pressure source is unsteady and not perfectly sinusoidal. As a result, it is not possible to identify a single characteristic wavelength or wave speed. The mean quantity is not necessarily a good representation without knowing how the data points are distributed. However, the distribution of the characteristics itself can provide some insights.

As the waves are circular, it is logical to examine the wave characteristics along the radial distance

from the jet impact point (r) instead of the x-y coordinates. For each displacement field, the displacements are averaged over a range of azimuthal positions at each fixed radial distance r to obtain the distribution of displacements in the radial direction $V(r)$. Figure 4.4a shows the locations (marked in green) where the displacement values are averaged for a fixed r , while Figure 4.4b shows an example of $V(r)$ at one instance in time. The signal shows clear oscillations in r representing the outward-travelling waves. The peaks are identified and the peak-to-peak distance in $V(r)$ is used to identify the local wavelength. Figure 4.5 shows the distribution of the peak-to-peak distances between the first two and the second two peaks for different jet velocity cases. These distances are used to represent the wavelengths closest to the jet impact point. The two FSSS cases with the lowest jet velocities $u_e = 2.19$ m/s and $u_e = 2.65$ m/s are not included as they do not show peaks with a prominence larger than 0.003 mm in $V(r)$ for most of the displacement fields. All the other jet velocity cases show similar distributions, where the peak-to-peak distance between the first two and second two peaks both have the highest concentration around 8mm ($1.6h_c$) except for the cases $u_e = 4.13$ m/s and $u_e = 4.84$ m/s which have the highest concentration around 12 mm ($2.4h_c$) for the peak-to-peak distance between the second and third peak. This suggests that the wavelength does not depend strongly on the flow properties. It is possible that the range of jet velocities tested is too small to result in significant differences in wavelength among the cases and a dependency on flow properties might become more obvious when a larger flow velocity range is tested.

$V(r)$ is also used to find the amplitude of the waves, as shown in Figure 4.6. Note that wave amplitude in this section refers to displacement amplitudes, not surface height amplitudes. The first and second peak amplitudes show approximately a normal distribution and increase with jet velocity except for the cases $u_e = 4.13$ m/s and $u_e = 4.58$ m/s which show smaller peak amplitudes than their neighbouring cases. For all cases, the second peak has an amplitude smaller than or equal to the first peak as the first peak is located closer to the jet impact point.

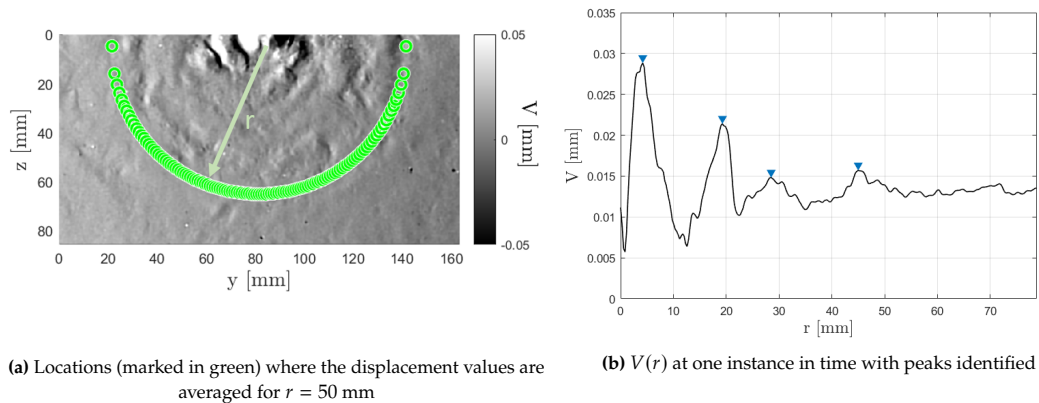


Figure 4.4: Wave characteristics quantification method

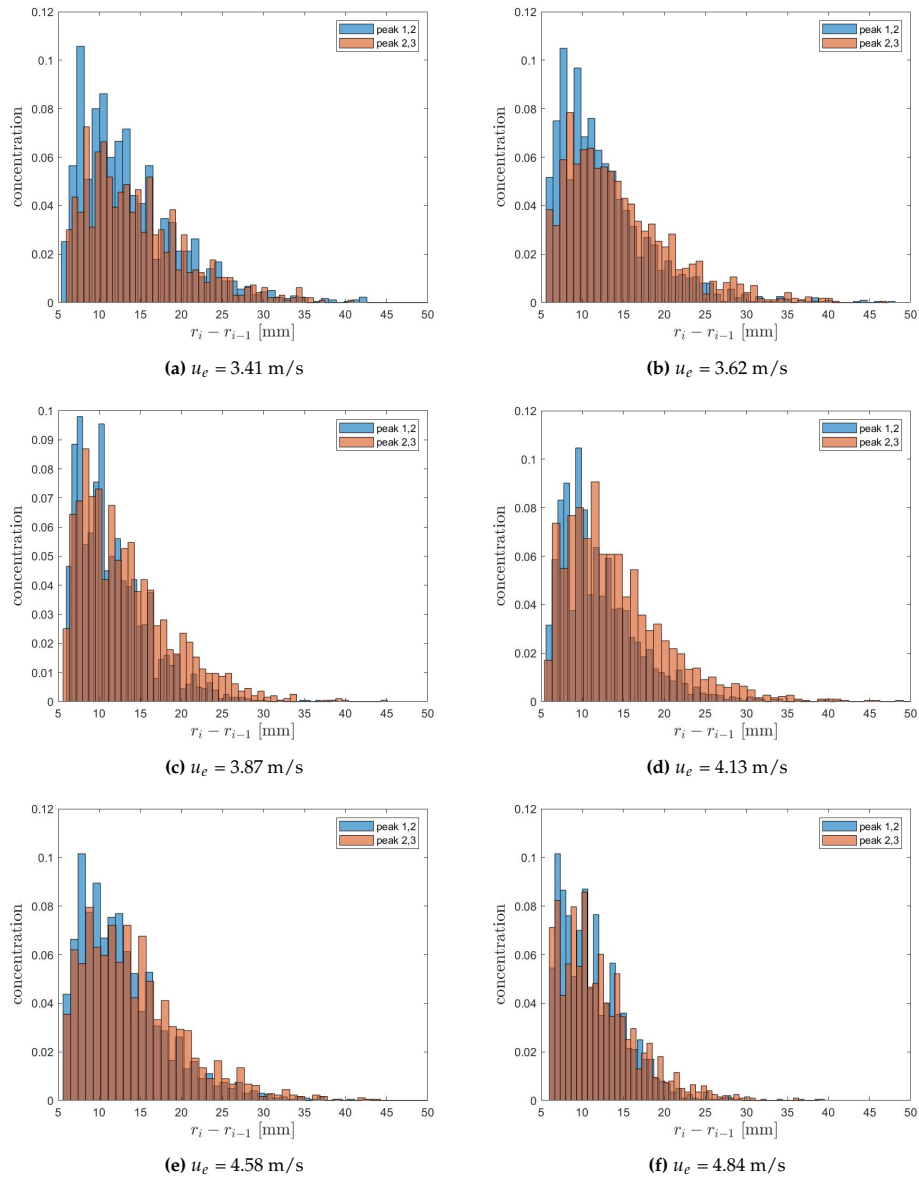


Figure 4.5: Distribution of $V(r)$ peak-to-peak distances for the first three peaks for all jet velocity cases

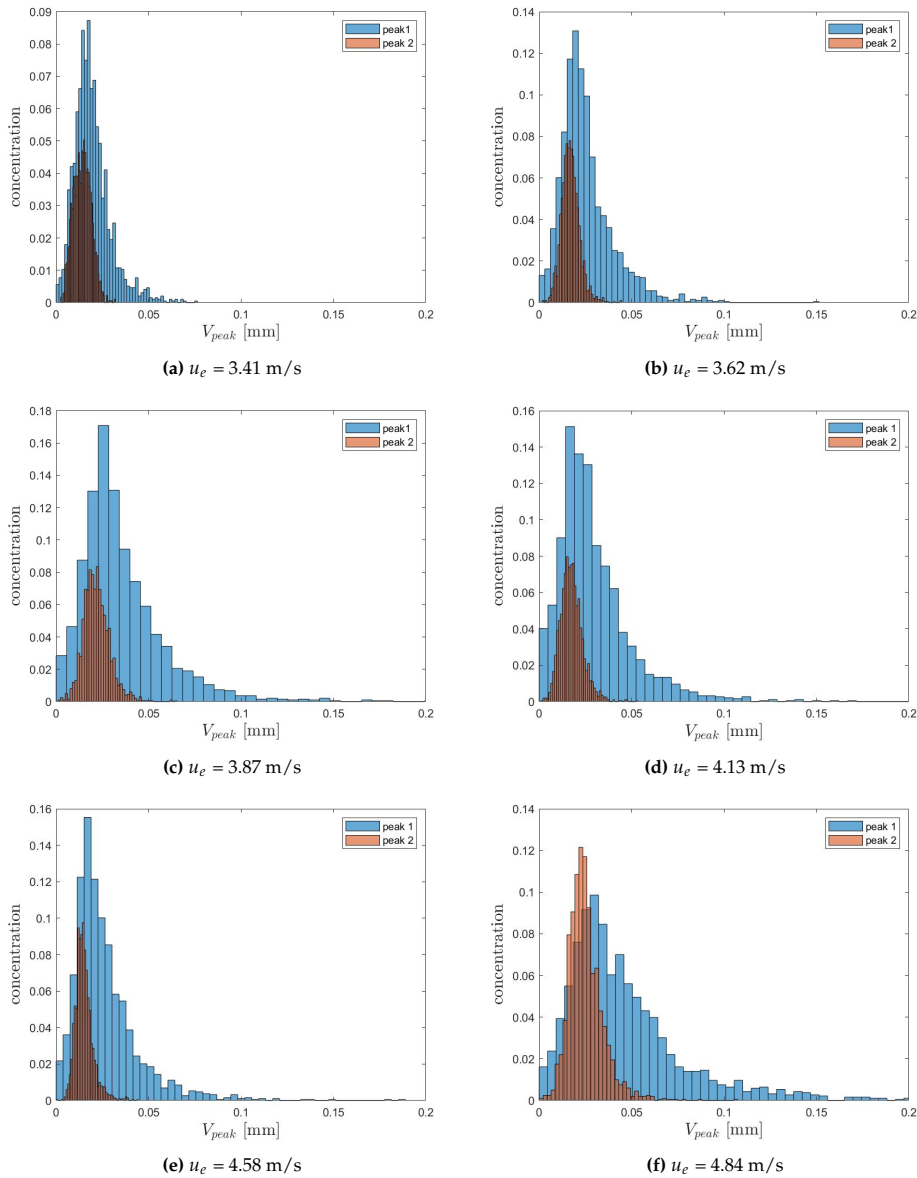


Figure 4.6: Distribution of $V(r)$ peak amplitudes for the first and second peak for all jet velocity cases

4.2.3. Wave speed

Similar to wavelength, it is not possible to identify a single wave speed as there is a wide range of wave speeds that vary in time and in radial distance. It is also difficult to find a distribution of the wave speed as the dynamic nature of the waves makes them hard to track from one time frame to another when only non-time resolved data is available. Figure 4.7a shows that the correlation in $V(r)$ between subsequent displacement fields is less than 0.5 for a large portion of the displacement fields as the waves change significantly within the sampling time of 0.02 seconds. For the cases with sufficiently strong correlations (> 0.5), it is still difficult to track some of the wave peaks as they disappear in the next frame. Figure 4.7b shows a rare example of two subsequent images with a high correlation of 0.84. In this case, the first four peaks can be tracked from the 14th to the 15th frame of displacement fields. One can see that as the most dominant peak at the smallest r is diminished a time frame later, the adjacent

peak at a higher r gained value. This is likely because the first peak transferred a part of its wave energy to the second peak as a component of it propagated radially outward. This shows that newer waves could have an impact on the evolution of the waves that were initiated at a previous instance in time.

In addition, the first two peaks both remained at the same r after the change in amplitude. The third and fourth peaks, on the other hand, both reduced in amplitude over time and shifted to a larger radial distance. The fourth peak travelled the most distance (approx. 12 mm) within a time step. This corresponds to a wave velocity of 0.6 m/s which is of the same order of magnitude as the shear wave speed of the coating and around the same value as the radial bulk flow velocity at 1 mm distance from the coating (≈ 0.6 m/s) as shown by PIV data in Section 4.4.

A frequency analysis was performed on the displacement fields through fast Fourier transform (FFT) and the results are included in Appendix A.3. However, time-resolved data is required to obtain data with stronger temporal correlations and for extracting more accurate frequency information.

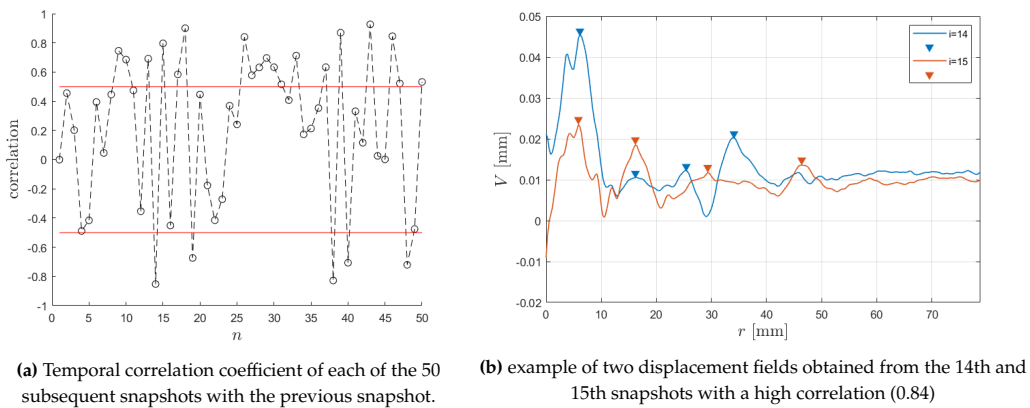


Figure 4.7: Extraction of temporal information from $V(r)$ for the case of $u_e = 3.87$ m/s

4.3. Validation with pressure sensors

To validate the CCPM technique, pressure fluctuations extracted from FSSS displacements using the pressure scaling from Equation 3.8 are compared with values measured by the pressure sensors.

4.3.1. Resolution

In order to make a fair comparison, the spatial resolutions of both methods are first examined. The spatial resolution of the CCPM technique is limited by the vector spacing. This implies that, although there is a wide range of scales in the flow from large-scale structures down to Kolmogorov scales, only structures with scales larger than the vector spacing are resolved. This effect is passed down from the displacement field to the P_{rms} field. On the other hand, the sensor pressure value is an average over the entire sensor inlet hole area which is a 5 mm diameter circle. Therefore, when comparing with sensor data, each P_{rms} data point from CCPM is taken as the average over an area of a similar size as the sensor inlet hole which is a 16 px by 16 px square (4.4 mm by 4.4 mm).

4.3.2. Symmetry

In the perfect experimental setting, one expects the pressure field to be axisymmetric about the x -axis at the jet impact point. However, this is likely not the case due to experimental limitations such as a potentially non-perpendicular impingement and asymmetric movements of the jet. To check for symmetry, several virtual probes are positioned in the P_{rms} field. For the sensor radial locations $r = 1.5$ cm and $r = 2.5$ cm, two additional probes were placed at the same radial distance but at a different azimuthal angle, as shown in Figure 4.8a.

The P_{rms} values at the probes are compared for all jet velocity cases in Figure 4.8b. At low jet exit velocities $u_e < 3$ m/s, the probes with the same radial distance give similar values at both $r = 1.5$ cm and $r = 2.5$ cm. At higher jet velocities, the probes on the left of the original sensors show a higher value. This is most evident for the radial location $r = 1.5$ cm where there is a difference of around 75 Pa (14%) for the highest jet velocity case. The probe on the right of the centerline at $r = 1.5$ cm shows a value lower than the value on the centerline at $r = 1.5$ cm but shows a higher value than on the centerline at $r = 2.5$ cm. This could be due to non-uniform coating thickness or non-perpendicular impingement of the jet, especially at high jet velocities, which would cause the coating surface height field to be asymmetric, leading to an asymmetric pressure fluctuation field. For the former, a thickness variation of 2.3 mm is required for a 14% change in pressure. This amount of thickness variation was not observed from the coating which is 5 mm thick. Therefore, the latter is more probable. Unfortunately, it is not possible to verify whether the jet impinged at an angle to the left or right (in the y -direction) as only PIV data in the x - z plane is available. Nevertheless, PIV data will be used to examine the potential deviation of the jet centreline from the x -axis in the z -direction in Section 4.4.

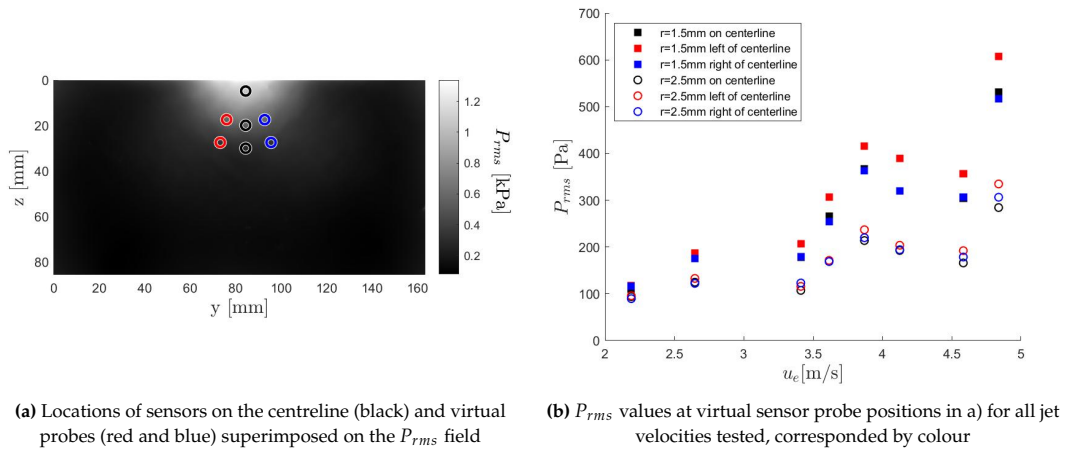


Figure 4.8: Comparison of P_{rms} at different azimuthal angles

4.3.3. Scaling

The pressure-deformation scaling in Equation 3.8 obtained from a TBL flow by Greidanus [3] is used to convert FSSS surface deformations to pressure fluctuations. One does not expect an exact alignment in the pressure-deformation scaling between the TBL flow cases in literature [3] and the impinging jet flow in the present study since, although the scaling for both cases measures the coating response due to forcing, the source of the forcing is fundamentally different for the two flows due to the difference in the physical mechanisms of the flows.

Figure 4.9a shows the comparison between P_{rms} values obtained from sensors and CCPM for all the test cases. Overall, the P_{rms} data from CCPM shows a decreasing trend with increasing radial distance from the jet impact point as expected, and an increasing trend with jet velocity similar to what the sensor data exhibits, except at a higher rate. Although the sensor trend increases monotonically, the CCPM P_{rms} shows large variations despite the CCPM pressure outputs having a small relative uncertainty as discussed in Section 3.7.3. Figure 4.9b shows the P_{rms} values obtained from sensors and CCPM as a function of u_{rms}^2 measured with PIV. Since P is proportional to u^2 , a linear scaling between P_{rms} and u_{rms}^2 is expected, as shown by the sensor data. Figure 4.9a and 4.9b further show that CCPM predicts higher P_{rms} values than sensor data. This suggests that the TBL scaling factor of 0.031 in Equation 3.8 overestimates the pressure for an impinging jet flow, which implies that lower pressure is required to achieve the same deformation for an impinging jet as a TBL.

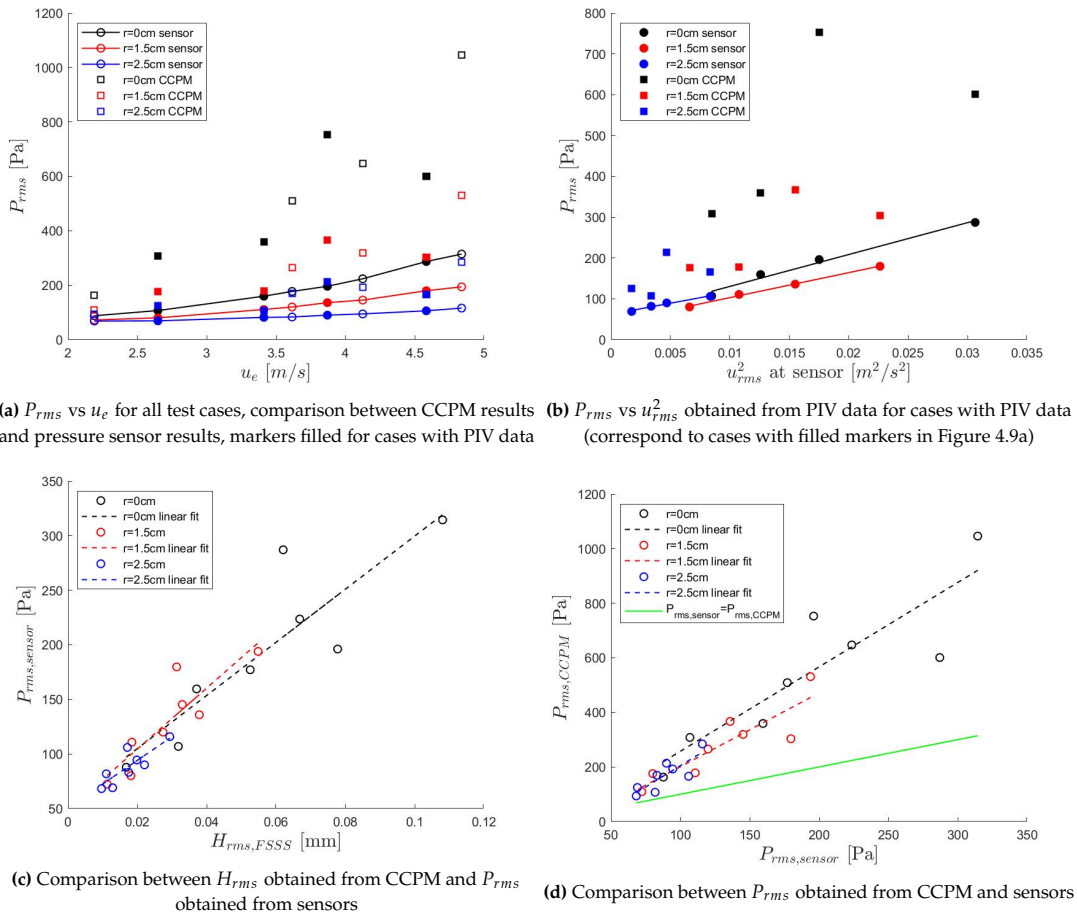


Figure 4.9: Comparison between sensor and CCPM results using the pressure scaling factor of 0.031 from Greidanus [3]

A linear trend between the H_{rms} obtained from FSSS and P_{rms} measured by the sensors is evident in Figure 4.9c which suggests that Equation 3.8 is perhaps, to some degree, universal. The part of the TBL scaling that is not suitable for the impinging jet appears to be the constant scaling factor of 0.031 which is too small as shown by the deviation from the line $P_{rms,sensor} = P_{rms,CCPM}$ in Figure 4.9d. To verify this hypothesis, CCPM P_{rms} values were recomputed from FSSS deformations using a new scaling factor of 0.12 which is calculated by matching FSSS deformations to the average sensor P_{rms} trend:

$$factor = \left[\frac{h_c}{N_m |G^*|} \sum_{m=1}^{N_m} \frac{dP_{rms,sensor}}{dH_{rms,FSSS}} \right]^{-1}, \quad (4.1)$$

where N_m is the number of sensors. In addition, an offset of 50 Pa is added to the P_{rms} to achieve an alignment in magnitude in addition to the trend, as shown in Figure 4.10c. The complete expression for the new scaling becomes:

$$P_{rms} = |G^*| \frac{H_{rms}}{0.12h_c} + 50 \text{ Pa}. \quad (4.2)$$

This is an ad-hoc scaling specific to the impinging flow setup in this study. However, it demonstrates the universality of the scaling as the linear nature between H_{rms} and P_{rms} depends only on the coating properties h_c and $|G^*|$ for both TBLs and the impinging jet tested.

The new scaling is not applicable to the pressure range below 50Pa as H_{rms} can not be negative by definition. Furthermore, it implies that zero deformation corresponds to a pressure of 50 Pa, which is not physical and does not match previous results by Greidanus [3]. As the scaling was extracted by matching deformation to sensor data, this offset of 50Pa comes from either an overestimation of the sensor P_{rms} or an underestimation of the coating deformations. The latter is less likely as the known sources of uncertainty of the surface height field have been quantified in Section 3.7.3 to be negligible and the time-varying background displacement gradients can only add to H_{rms} . On the other hand, a part of the 50 Pa offset could be artificial enhancement of the sensor P_{rms} due to noise that is not caused by turbulence alone, for example, vibration-induced electrical noise which has been quantified previously to be ± 30 Pa. Looking at the sensor data alone in Figure 4.9b, it seems that the three sensors share slightly different pressure scalings from u_{rms}^2 , where the sensor at the jet centre has the highest slope and magnitude. This is possibly due to the unstable movement of the jet artificially adding to the P_{rms} values which would indeed be most pronounced at the jet centre. All three sensor slopes intersect the y-axis of Figure 4.9b at around 50 Pa, which is in alignment with the 50 Pa offset in the new scaling.

The CCPM results using the new scaling are shown in Figure 4.10. Figure 4.10a shows the new CCPM predictions align well with the sensor data for most of the jet velocities tested. Figure 4.10d shows that the new scaling successfully collapse CCPM pressure data and sensor data onto the curve $P_{rms,sensor} = P_{rms,CCPM}$ for most data points.

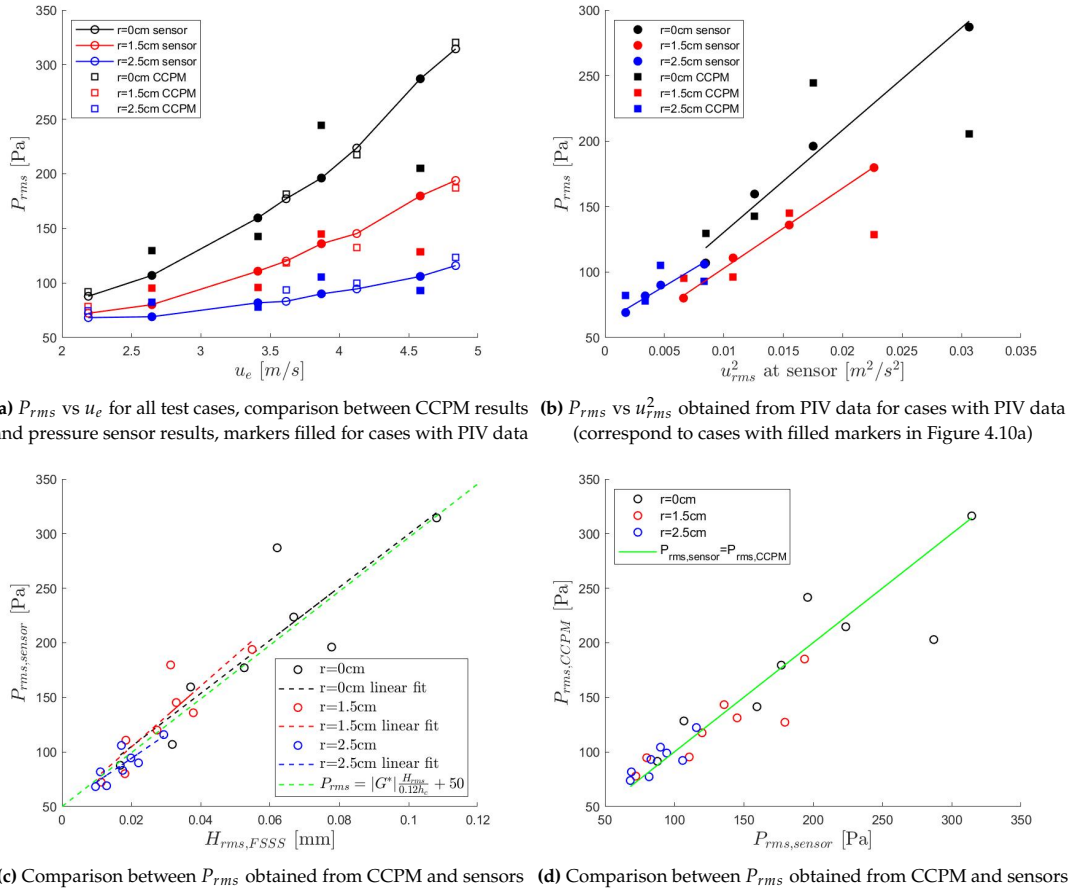


Figure 4.10: Comparison between the sensor and FSSS results using a new pressure scaling in Equation 4.2

Figure 4.10 also shows that case $u_e = 3.87$ m/s and $u_e = 4.58$ m/s have the highest deviation from the linear trend, and the deviation is the worst at the jet impact point location $r = 0$ cm. Case $u_e = 3.87$ m/s not only shows an unexpectedly high P_{rms} compared to the neighbouring cases but it was also shown previously in Section 3.7.2 to have a high strain rate and deformation when compared to the neighbouring case. Looking at the snapshots for this case, it seems that there is a higher than average level of fluctuations in background displacements that vary from one snapshot to the next. This suggests that perhaps at this jet velocity, there is resonance amplifying the vibrations. However, it is not possible to verify this without accurate frequency information. Case $u_e = 4.58$ m/s, on the other hand, has a much lower P_{rms} than expected by the linear trend. Although the exact cause is not known, it is possible that the pump had a lower performance than expected for this test case. It is worth pointing out, however, that the outliers do not have a jet exit velocity significantly different from the neighbouring cases.

4.4. Flow characterization

PIV was used to obtain 2D velocity fields in the x-z plane, particularly near the impingement plate, in order to quantify the effect of coating deformations on the flow. Experiments were conducted with both the coating plate and a rigid plate for comparison.

4.4.1. Velocity contours

Mean and RMS velocity contours for the streamwise and radial velocity components for a single test case are shown in Figure 4.11 and 4.12. Although the FOV encompasses the entire jet from the nozzle exit to the impingement plane, analysis is carried out only in the region near the impingement plane.

The in-plane velocity components near the jet nozzle are unreliable according to the rule-of-thumb for particle displacement [30] as the streamwise particle displacements are much larger than 7 pixels while the radial displacements are much smaller than 5 pixels, which results in poor correlations. However, vectors closer to the impinging plane ($d < 15$ cm) are sufficiently accurate according to the PIV correlations calculated in Davis. Therefore, only the section of the FOV within 15 cm from the impingement plane is analyzed.

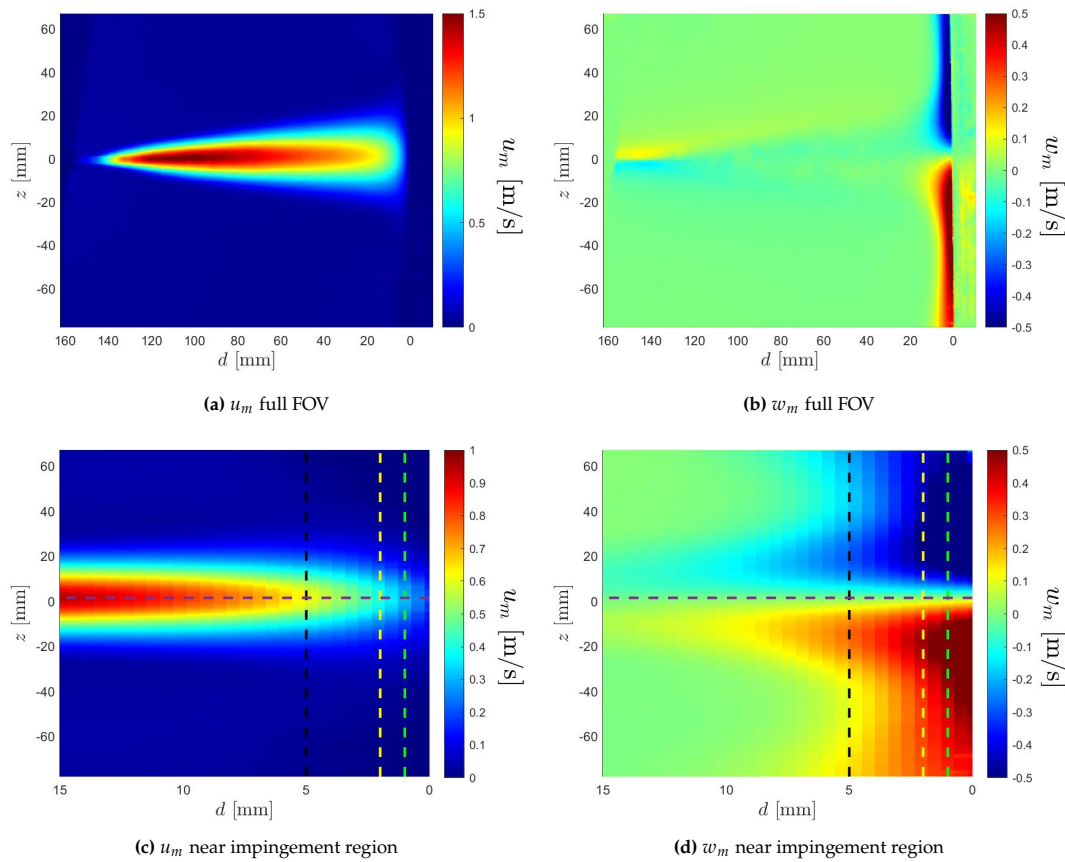


Figure 4.11: Mean velocity profiles for the streamwise and radial velocity components for case $u_e = 4.58 \text{ m/s}$ with the coating plate. The dotted lines at $d = 1$ mm (green), $d = 2$ mm (yellow) and $d = 5$ mm (black) indicate locations along which analysis is performed

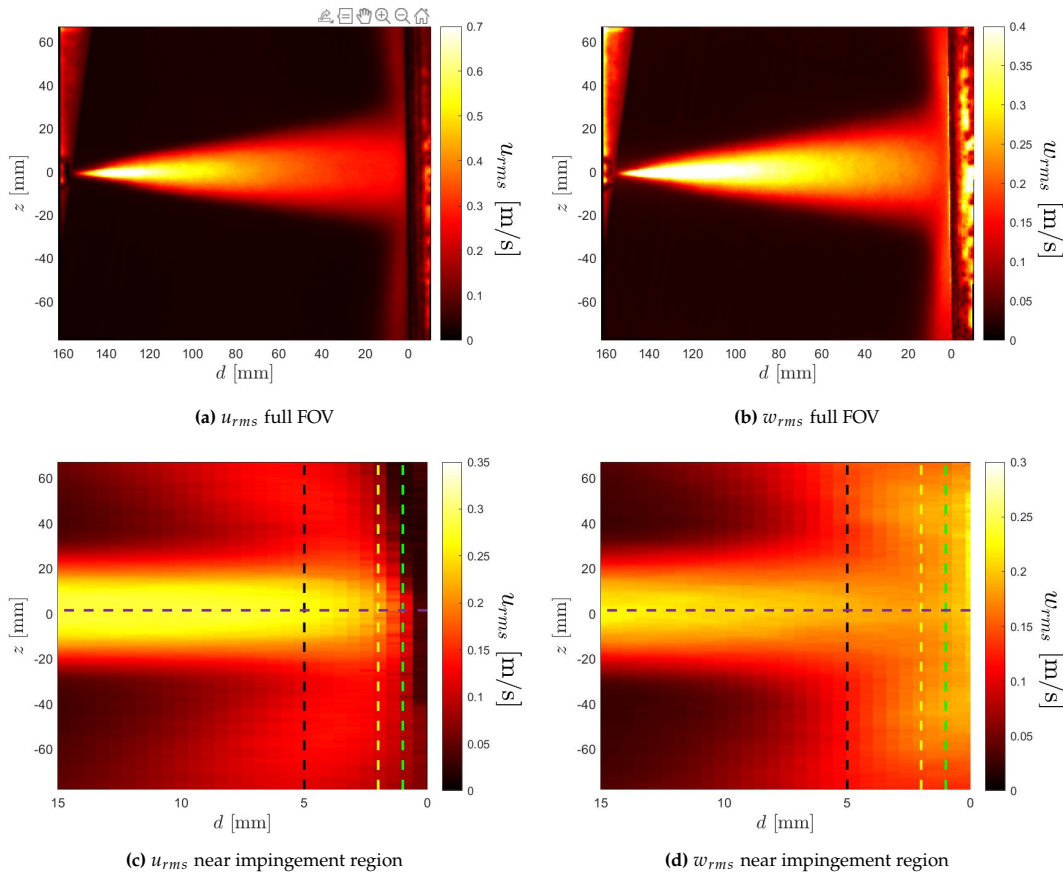


Figure 4.12: RMS velocity profiles for the streamwise and radial velocity components. The dotted lines at $d = 1$ mm (green), $d = 2$ mm (yellow) and $d = 5$ mm (black) indicate locations along which analysis is performed.

4.4.2. Profiles along jet centreline

First, the variation in velocity statistics along the jet centreline is examined. The coating and rigid plate cases are compared. Figure 4.13c shows that the turbulence intensity of the streamwise velocity component u_{rms}/u_m increases with decreasing distance from the plate d (defined in Section 3.8) for both the coating plate and the rigid plate. This is due to the fact that the rate of decrease in mean velocity due to impingement is much faster than the rate at which RMS velocity decreases, as shown in Figure 4.14. Figure 4.13b further shows that the difference in turbulence intensity between the coating plate case and rigid plate case mostly occurred near the plate ($d < 2$ mm) for all jet velocities. In addition, the turbulence intensity at the wall is higher for all test cases when the coating plate is used. Cases with lower jet exit velocity show a larger difference in turbulence intensity between the coating plate and rigid plate. This suggests that the two-way coupling effect is stronger for lower jet velocity cases, which is counter-intuitive.

On the other hand, the turbulence intensity of the radial velocity component decreases as d becomes smaller as w_m increases faster than w_{rms} near-plate. This increase in w_m is due to the jet flow changing direction from perpendicular to the plate to parallel to the plate surface. Figure 4.13d shows that all cases have a lower radial turbulence intensity when the coating plate is used, where the highest jet velocity case has the largest difference.

Looking at the mean velocity trends in Figure 4.14, the highest jet velocity case shows the largest

deviation between the coating plate and rigid plate scenarios. Figure 4.14d) revealed a sudden decrease in rigid plate radial velocity at $d < 1$ mm. Similarly, the RMS data in Figure 4.15b reveals a sharp increase of up to 25% for the difference in U_{rms} between the coating case and rigid plate case. Notably, this increase in the difference between the two cases mostly occurred at $d < 1$ mm, which matches the observation from mean flow data. For all jet velocity cases, the presence of the coating modified the u_{rms} values in the case of a rigid plate by more than 10% in close proximity of the wall $d < 1$ mm, as shown in Figure 4.15b. This is higher than the u_{rms} convergence interval (shown in Figure 3.17) and the uncertainty computed by Davis ($< 1\%$), meaning that the difference can indeed be resolved. However, it is likely that the PIV data at such proximity to the wall is unreliable due to a lower particle density and sharp gradients [35] and thus cannot be trusted. Also, since the spatial resolution of the PIV data is 0.54 mm, there are only two data points within 1mm from the wall which is insufficient to make a definitive statement.

Furthermore, in terms of the difference between the coating and rigid plate cases, there is no monotonic trend in turbulence intensity or RMS values with increasing jet velocity, as the highest difference in u_{rms} was observed for the case $u_e = 3.87$ m/s, and the lowest was observed for case $u_e = 3.41$ m/s. In addition, the values are relatively close to each other (from slightly above 10% to less than 25%). Further from the impinging plane ($d > 1$ mm), the difference in streamwise and radial velocity RMS are both less than 5% for all test cases.

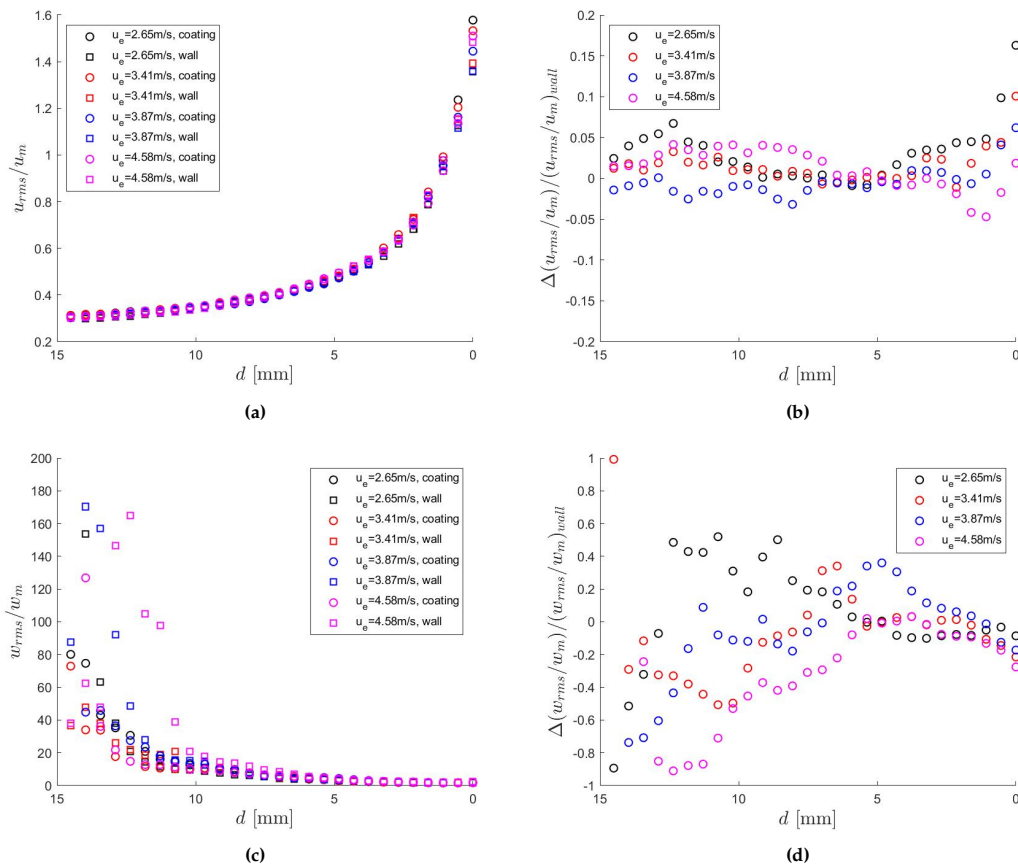


Figure 4.13: Comparison of the streamwise and radial turbulence intensity between the coating and rigid wall cases. Δ refers to the coating plate value subtracted by the rigid plate value

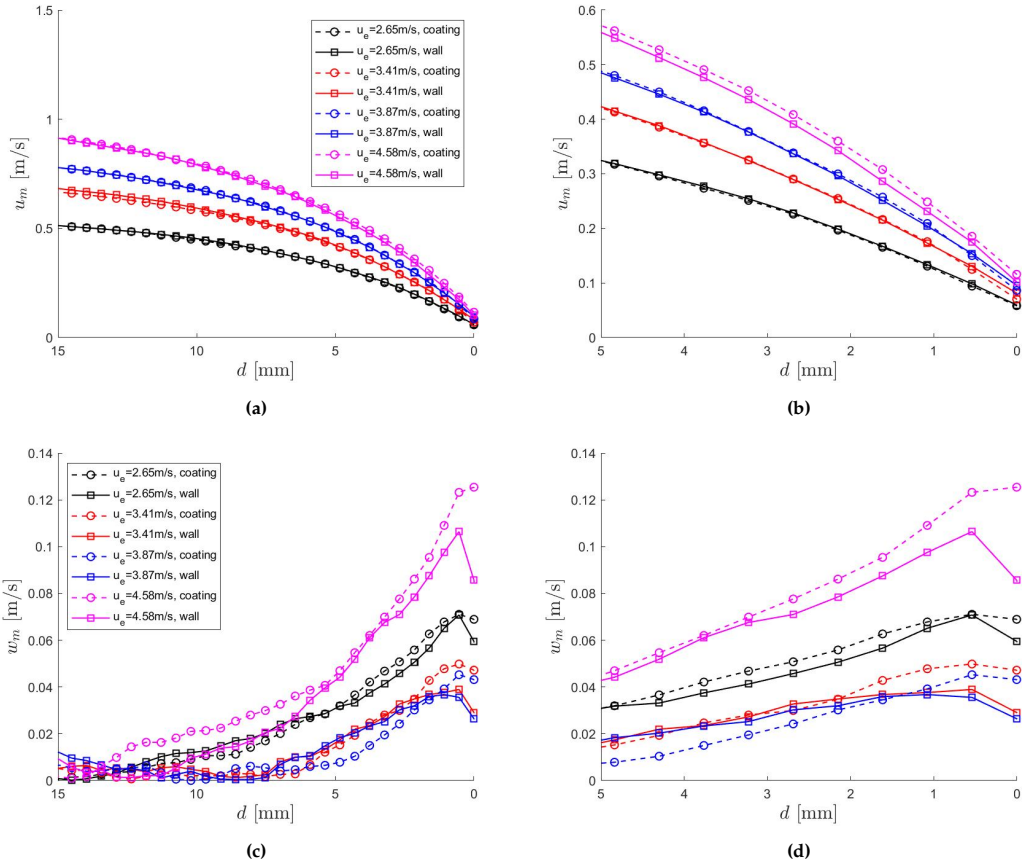


Figure 4.14: u_m, w_m as a function of distance from the impinging plate along the jet centreline

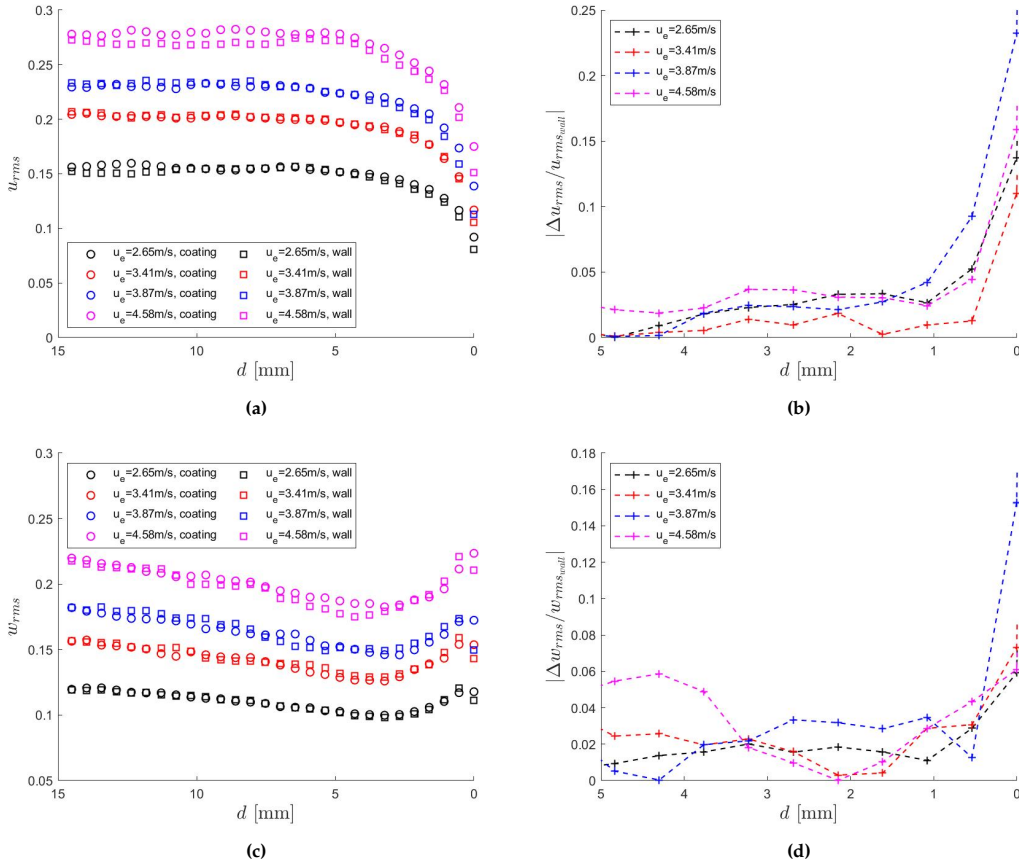


Figure 4.15: u_{rms} and w_{rms} as a function of distance from plate along the jet centreline

4.4.3. Radial profiles

Next, the radial variations of the velocity statistics are examined. Figure 4.16 and 4.17 show the mean and RMS streamwise and radial velocity profiles at fixed distances (d) of 5 mm, 2 mm and 1 mm from the impinging plane, as a function of the radial distance from the jet impact point r .

At a distance of 5 mm from the impinging plane, as shown in Figure 4.16a and 4.17a, there are no significant differences in u_m and u_{rms} between the coating and rigid plate cases. At a distance of 2 mm from the impinging plane, the mean velocity profiles at the jet impact point ($r=0$) begin to separate for the highest jet velocity case, and differences can be observed in the RMS profiles at large radial distances ($|r| = 20$ mm). At a distance of 1 mm from the impinging plane, notable deviations in the RMS, as well as mean velocity profile, can be observed for all jet velocities tested at the jet impact point, as well as at larger radial distances. In addition, differences in the velocity profiles can also be observed at radial distances outside of the jet impact zone ($|r| > 40$ mm). In fact, Figure 4.16e shows that the largest difference in u_m occurs at $|r| > 40$ mm.

The w_m profiles also reveal a difference between the regions above and below the jet impact point. It appears that the coating imposed a larger perturbation on the region above the jet impact point which is especially evident at $d = 1$ mm. In addition, the region above the jet impact point also has a higher mean radial velocity than the region below for both the coating plate and the rigid plate. This is due to the slightly forward tilting of the plates which results in the region above the jet impact point having

a smaller d than the region below in reality, as the calibration coordinate frame has a small relative rotation with respect to the frame in which the plates align with the z -axis.

The u_m radial profiles at large radial distances show that the jet itself impinges slightly upward instead of along the x -axis. This suggests that the jet has a similar rotation relative to the calibration frame as the plates. The upward tilting appears slightly less severe for higher jet velocities, making the impingement less perpendicular to the tilted plates. This corroborates the observation in Section 4.3.2 that the P_{rms} field is less axisymmetric at higher jet velocities. To correct for this misalignment, the FOV needs to be rotated to match the y - z frame. This is, however, of lesser importance as the rotation is the same for both the coating plate and rigid plate cases and thus does not affect the main observation that the coating begins to have a significantly larger effect on the surrounding flow at distances of $d \leq 1$ mm.

A closer look at Figure 4.16f shows that there are large fluctuations in the coating case w_m for $r > 20$ mm above the jet impact point that is only observable at $d = 1$ mm and a corresponding increase in w_{rms} of up to 50% when compared to the rigid plate case as shown in Figure 4.17f. Similar observations can be made below the jet impact point albeit with a much smaller amplitude. It is not possible to verify the cause behind this increase with the data available. However, it is possible that the propagating surface waves leads to local acceleration/deceleration in flow along the z directions which could explain the large fluctuations.

Lastly, Figure 4.16 suggests that the coating deformation at sensor location $r = 0$ cm is mostly due to the head-on impact as u_m is at the maximum and w_m is near zero, while the deformation further from the jet impact point (at sensor location $r = 1.5$ cm and $r = 2.5$ cm) is also largely due to the shear component of the flow as $u_m \ll w_m$.

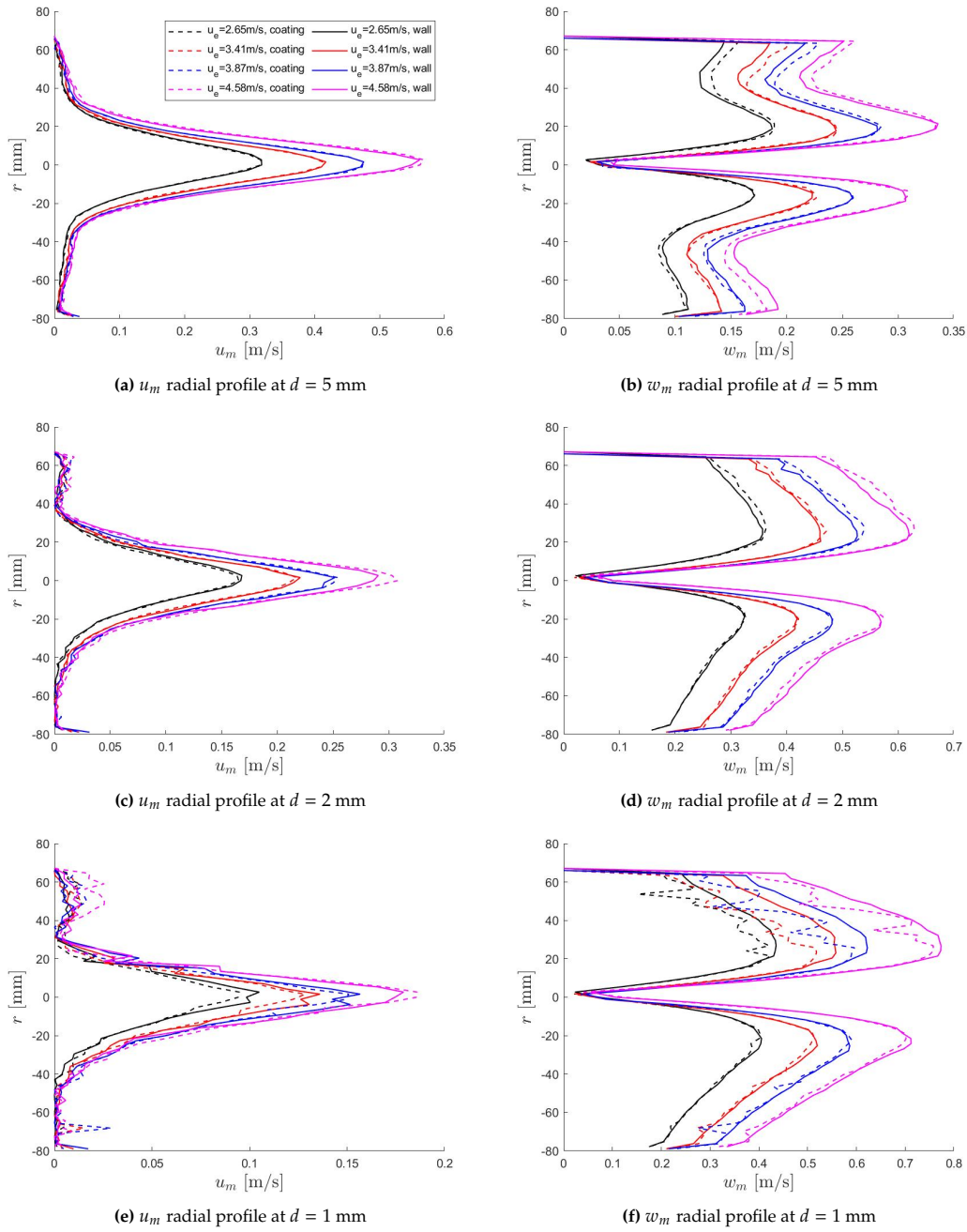


Figure 4.16: u_m and w_m as a function of radial distance from jet impact point at a fixed distance d from the impinging plane. (For ease of visualization, every 5 grid point was plotted)

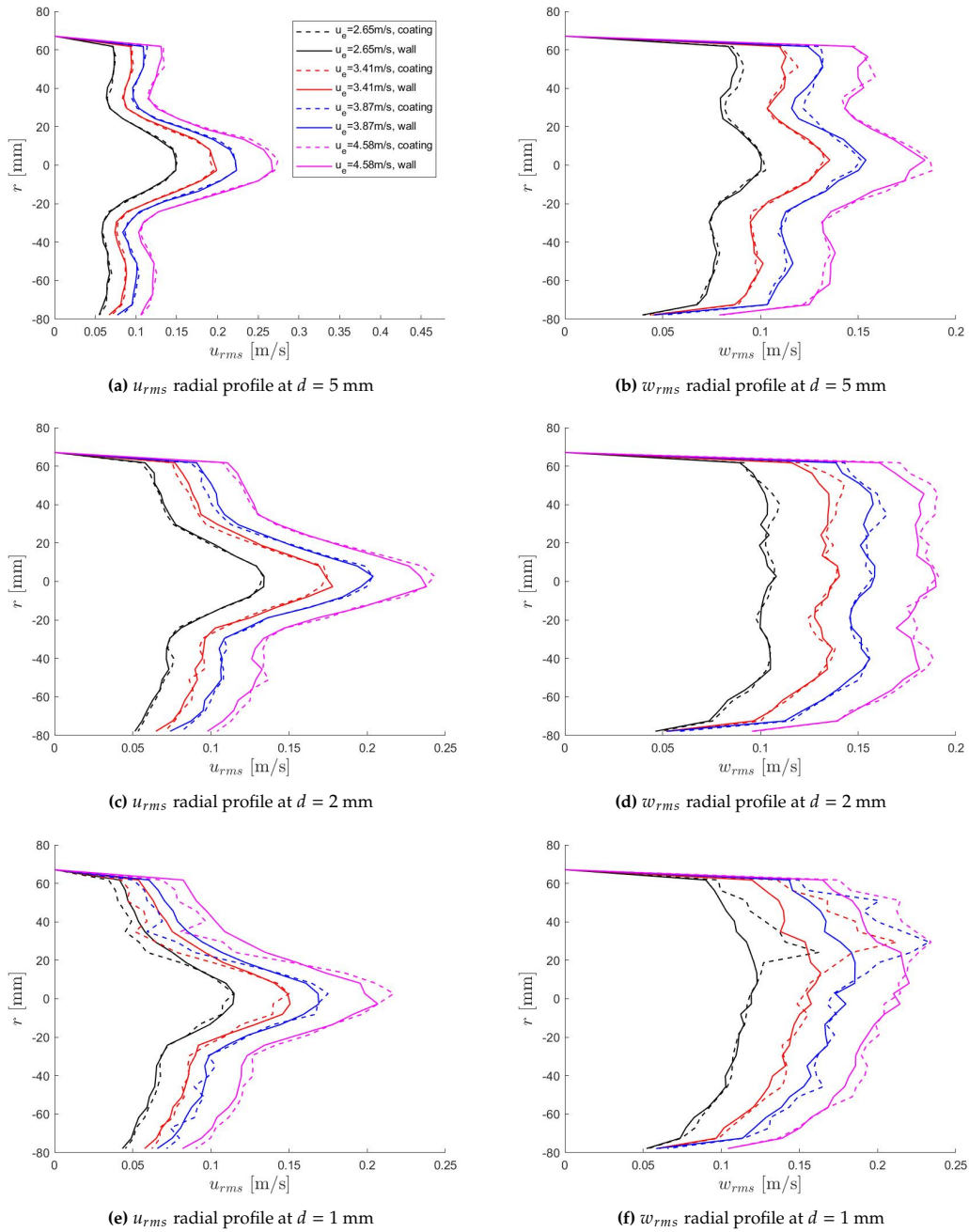


Figure 4.17: u_{rms} and w_{rms} as a function of radial distance from jet impact point at a fixed distance d from the impinging plane. (For ease of visualization, every 5 grid point was plotted)

4.5. Coupling regime

All evidence so far suggests that all flow-coating combinations tested in this study fall within the one-way coupling regime, where coating deformation does not affect the surrounding flow significantly. No clear sign of transition from one-way to two-way coupling is observed from the surface deformations, the relationship between coating deformation and pressure fluctuations, and velocity profiles.

For turbulent boundary layer flows, the literature suggests that large amplitude waves with a much

smaller wave speed than the bulk speed (static divergence waves) signal the transition from one-way to two-way coupling regime [7]. In the case of an impinging jet, the pressure footprint forms ring-shaped waves on the coating that are visible at all jet velocities. The amplitudes of these waves increase with velocity and the wavelength and wave speed change with radial distance and in time as shown in Section 4.2. The wave speed for one case is estimated to be 0.6 m/s which is comparable to the radial bulk flow speed. The unsteadiness of these waves makes it hard to identify any static divergence waves by eye. Future time-resolved analysis might reveal the much slower static divergence waves if there were any.

Previously in Section 3.7.4, the H_{rms}/h_c ratio obtained from the current study corresponds to two-way coupling according to the shear flow study results by Greidanus [3]. However, the new scaling suggests that, for an impinging jet, the same amount of pressure would lead to higher coating deformation when compared to a TBL. Therefore, one can not predict the transition to two-way coupling by comparing the deformation to the threshold in Figure 2.6. In fact, it is not possible nor reasonable to establish a criterion for two-way coupling based on deformation alone without any regard to the flow, since the coupling phenomenon involves both the coating and the flow.

From the pressure data, the hypothesis that no two-way coupling occurred within the tested velocity range can be made as the relationship between the FSSS coating deformations and the sensor pressures is relatively linear. If two-way coupling occurred, a large jump in P_{rms} and a strong deviation from the linear pressure-deformation trend as shown in Figure 2.6 would have been observed. In addition, the maximum $P_{rms}/|G^*|$ obtained from the current study is in the order of $O(10^{-2})$. Comparing with the coupling regimes extracted from shear flow experiments [3] in Figure 2.6, it seems that the range of pressure fluctuations induced by the impinging jet on the coating surface falls within the one-way coupling regime. This comparison is, however, not valid as the two pressure sources have different mechanisms and as the new scaling suggests, a turbulent impinging jet could induce higher deformations with the same pressure fluctuations as a TBL flow.

Furthermore, the PIV results show that the effect of coating deformation on flow velocity profiles occurs mostly at distances within 1mm from the impinging plane. At distances further than 1mm from the impinging plane, there is a less than 5% change in u_{rms} and w_{rms} . In addition, no monotonic trends on the effect of coating on rigid plate velocity statistics with increasing jet exit velocities were observed. It is likely because for an impinging flow, the flow has the freedom to travel around the edges of the impinging plate, and deformation has little effect on the bulk flow, unlike turbulent boundary flows. Furthermore, the jet velocities for the different test cases are not too different from each other as there is only around a 2 m/s difference between the lowest and highest jet velocities tested.

Finally, according to the numerical shear flow studies by Duncan [19], two-way coupling is expected when the bulk flow speed is sufficiently large ($> 1.2C_t$) when compared to the shear wave speed. The PIV data in Figure 4.16 shows that the radial component of flow velocity near the impingement plate is around the same order of magnitude as the shear wave velocity of the coating for the maximum jet velocity case but slightly smaller. Therefore, two-way coupling is unlikely according to this criterion from literature. However, this criterion must be applied with caution as the radial component of the impinging jet flow near-plate is not exactly the same as a turbulent boundary layer.

Conclusions and Recommendations

5.1. Conclusions

In summary, a compliant-coating based pressure measurement (CCPM) technique was designed, built and tested with a submerged impinging jet. The CCPM technique consists of several key components. First, the apparent movement of a background dot pattern through a layer of compliant coating is quantified using free-surface synthetic schlieren (FSSS). The displacement field of the dot pattern is proportional to the slope of the deformed coating surface which is spatially integrated to obtain the coating surface deformations. The deformations are then converted to pressure fluctuations using a pressure-deformation scaling extracted using sensor data and are based on a shear flow scaling by Benschop et al. [8]. The effect of coating deformation on the surrounding flow is characterized using particle image velocimetry (PIV).

The main research objective is fulfilled as the CCPM technique developed successfully obtained pressure fluctuations on a surface underwater within the same order-of-magnitude as sensor pressure measurements through the pressure-deformation scaling proposed in Equation 4.2. The research questions in Chapter 1 are addressed as follows:

What combinations of flow and coating properties are required to achieve sufficient coating deformation distinguishable by the optical setup while maintaining one-way coupling?

A submerged turbulent impinging jet with jet exit velocities in the range of 3.41 m/s to 4.84 m/s induced deformations (H_{rms}) in the range of 0.01 to 0.11 mm on the surface of a 5mm thick viscoelastic coating with $|G^*| = 1.5$ kPa. This set of flow and coating combinations is shown to fall within the one-way coupling regime according to evidence from the pressure trends and velocity data.

Can the one-way coupling model previously established from boundary layer flows be used for obtaining pressure fluctuations in a different flow scenario? If so, to what extent can the universality of the model be assumed? If not, what should an ad-hoc model look like?

The pressure-deformation scaling with the scaling factor of 0.031 in Equation 2.2 from Benschop et al. [8] overestimates the pressure fluctuations induced by the impinging jet as the same pressure leads to a higher deformation when compared to a turbulent boundary layer. However, the linear trend of the

scaling was observed. A new ad-hoc scaling factor of 0.12 was obtained using the measured coating deformation and pressure data from pressure sensors (Equation 4.2). It is possible that the linear scaling between pressure fluctuation and deformation holds for impinging jets with different flow parameters and possibly other flow types. A different scaling factor is likely needed to provide a good estimate of the pressure magnitude, which would depend on the method of forcing.

What range of pressure fluctuations in the flow can the selected coating capture? What limits the resolution and accuracy of the CCPM?

Using the new scaling, the coating was able to capture pressure fluctuations in the range of 72 Pa to 314 Pa. It was shown that within this range, the image strain can be considered moderate, which prevents additional uncertainty in displacement measurements. Moreover, the coating can be considered sufficiently thick for the range of coating deformations observed and thus the deformations were not attenuated.

The resolution of the surface deformations and thus the pressure is limited by the parallax distortion to be 2%. The accuracy of the pressure reconstruction also scales with the uncertainty of displacement measurements due to the DIC algorithm [29]. In addition, background displacement gradients were observed which could introduce additional uncertainties to the pressure output. However, there is not sufficient evidence to conclude the cause of background gradients in the displacement fields. Although the set of cases with the least background displacements was chosen for analysis, this is potentially the main source of uncertainty in the study. It is also unclear to what extent the movement of the jet during experiments adds to the RMS of the pressure results.

Furthermore, the FSSS results were limited to a spatial resolution of 0.28 mm by the vector spacing. As a result, the final CCPM pressure output only encompasses the impact of large-scale structures in the impinging jet flow. It is unknown how smaller-scale structures would affect the result.

Given a flow scenario, to what extent does a chosen coating, which can deform sufficiently to be measured by a given optical setup, influence the flow? Can experimental velocity data be used to establish such a criterion for distinguishing between the coupling regimes?

For the range of jet exit velocities tested, PIV data showed that the coating has a less than 5% influence on the RMS of the velocity components when compared to a rigid wall, at distances larger than 1mm from the impinging plane, while the influence is larger immediately next to the impinging plane ($d < 1$ mm). However, PIV data immediately next to the plates is likely unreliable. It is not possible to identify a criterion for distinguishing between the two coupling regimes from velocity data as clear indications of two-way coupling were not observed.

5.2. Future recommendations

This study serves as a first exploration of using a compliant coating for pressure measurement purposes. It successfully demonstrated the potential of a CCPM technique for providing pressure field measurements underwater and paves the way for future explorations and potentially full validation of the CCPM technique. As a result of the study, several recommendations for future studies can be made and are discussed in this section.

First and foremost, it was shown for the first time that for an impinging jet, a similar scaling between pressure fluctuations and surface deformations to that extracted from TBL flows can be applied with an adjusted constant factor. This shows a universal property, namely the linear relation between compliant

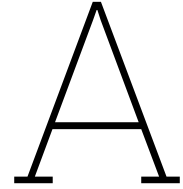
coating deformation and pressure fluctuations which is based on coating properties alone. Future studies with other types of flows are required to further explore the extent of universality and the flow-independency.

Secondly, as no transition from one- to two-way coupling was observed, to identify the two-way coupling transition threshold for an impinging jet with the current coating, the range of jet velocities must be extended to higher values. However, a different coating might be required as surface breakage was already observed at a jet velocity slightly higher than the largest jet velocity tested. On the other hand, only one viscoelastic coating was tested in this study. Since two-way coupling was not detected with the current coating in the range of feasible jet exit velocities, a coating with a smaller stiffness can be used to extend the range of pressures in the one-way coupling regime as it would be more sensitive to deform under pressure fluctuations. Visco-elastic coatings with other formulations as well as non-viscoelastic coatings may also be explored. Then, the combination of coating and flow parameters can be optimized to test a large range of pressure fluctuations.

Thirdly, the CCPM technique can only extract the component of spatial pressure distribution that deviates from the mean. As the coating is incompressible, a spatially-uniform pressure distribution would not induce coating deformations. This is shown in the post-processing where the mean spatial surface height is set to zero. Therefore, it is not straightforward to obtain quantitative pressure at any point. To extract the spatial mean, a direct pressure sensing technique such as using a compressible material or putting a spring scale at the back of the coating plate is required. On the other hand, the CCPM can sense both the temporal mean and temporal fluctuations. This is shown by the background inhomogeneity in the displacement fields that is constant in time (Appendix A.1).

Next, to further evaluate the effect of the coating plate boundary, one might consider testing coating plates with different shapes and sizes to set different boundary conditions. It is also beneficial to investigate the effect of surface curvature as the current study and all compliant coating experiments in the literature so far were limited to a flat plate. Such studies would bring the CCPM technique one step closer to real-world applications where the coating is likely applied to irregular shapes and surfaces.

Furthermore, in the current study, FSSS and PIV experiments were conducted separately. For future testing of the CCPM technique, doing PIV and FSSS experiments simultaneously could provide additional insights into the flow-coating interactions. For example, flow structures in the velocity field can be mapped to features in the reconstructed coating deformation field to establish a correlation between flow features and the coating behaviour. Time-resolved data would also be needed for extracting accurate temporal information such as the wave speeds and potential vibrations in the setup. The Reynolds shear stress in addition to the mean and RMS velocities may be examined as it has been suggested as a parameter for tuning the coating response [2] and could provide an indication for the coupling regime as shown by Greidanus [3].



Additional plots and analysis

A.1. Additional steps in post-processing

As discussed in Section 3.6.2, additional post-processing steps were investigated and showed good results for improving the quality of the displacement field. The complete flow chart including these additional steps is shown in Figure A.1.

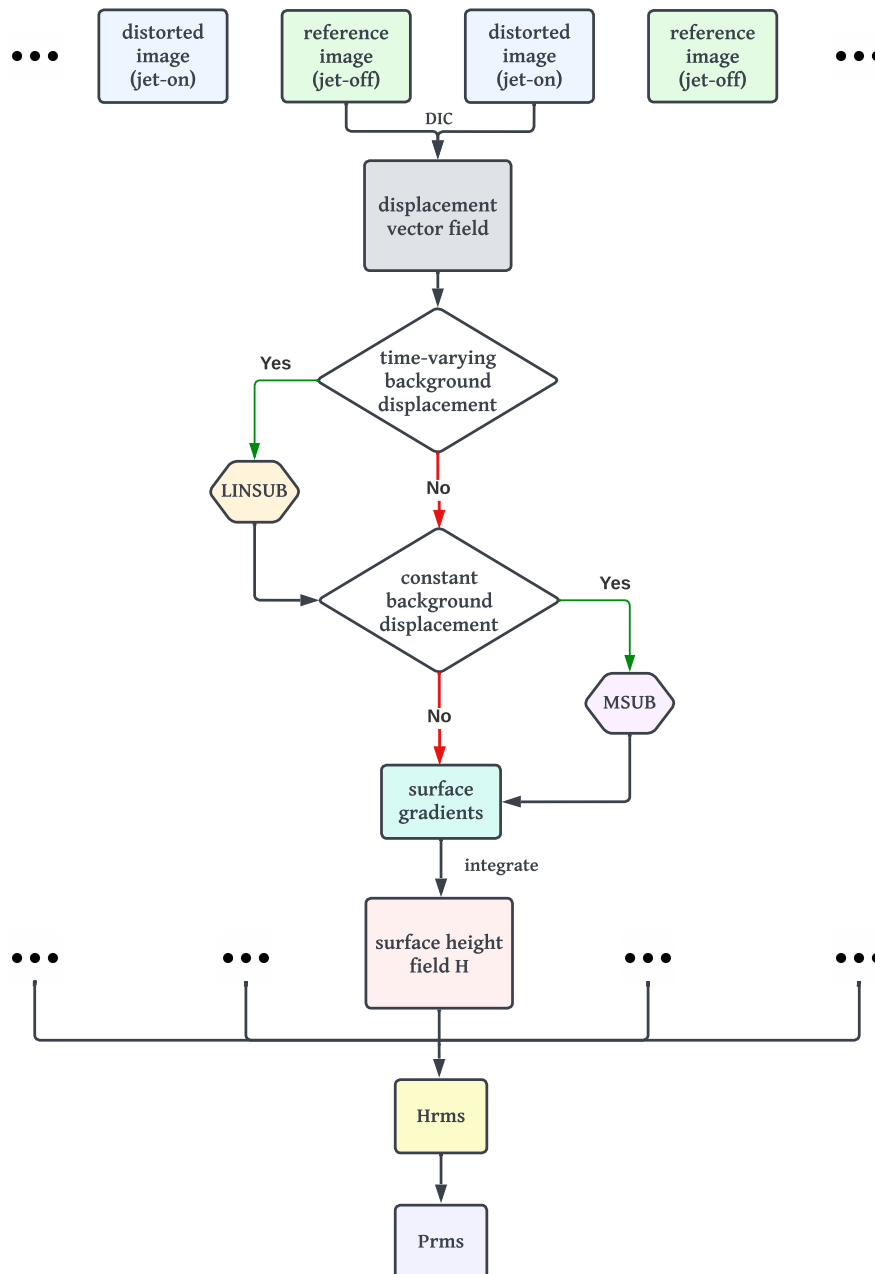


Figure A.1: FSSS processing and post-processing flow chart with extended steps

Removing background gradient (LINSUB)

In a few cases, there is a significant background gradient in the displacement field. This presents itself as corners with largely positive or negative displacements connected by a smooth gradient as shown in Figure A.2. The horizontal displacement field suggests that dots on the left side of the plate moved towards the right while those on the right side moved towards the left as also shown by the arrows in the vector field in Figure A.3. It was first hypothesized that this is due to the movement of the coating plate on its support structure when impacted by the jet. This has been observed in previous experiments according to personal communication with Greidanus [3] for the case of a much larger coating plate that displaced under its weight. In the current case, a backward movement of the

coating plate would result in an apparent inward movement of the dots. For the current case, there was a maximum backward plate movement of 0.24 mm or around 3.5 pixels according to the following calculation:

$$\tan(\theta) = \frac{L/2}{h_{cd}} = \frac{L/2 - \delta y}{h'_{cd}}, \quad (\text{A.1})$$

where δy is the background horizontal displacement of the dot pattern which is 0.03 mm at the bottom left and bottom right corners of the FOV in the worst case, h_{cd} is the distance from the camera to the dot pattern without plate movement and h'_{cd} is the distance from the camera to the dot pattern assuming plate movement. This level of plate movement is not improbable.

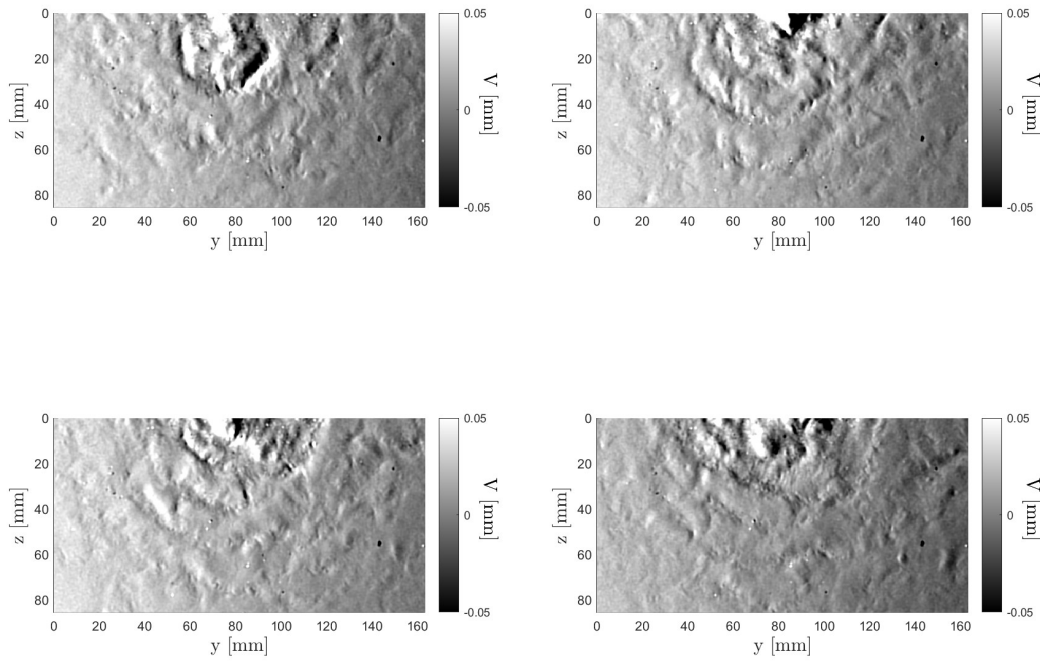


Figure A.2: Displacement field of several subsequent snapshots demonstrating background gradient varying in time, duration between two snapshots $\Delta T = 0.02\text{s}$

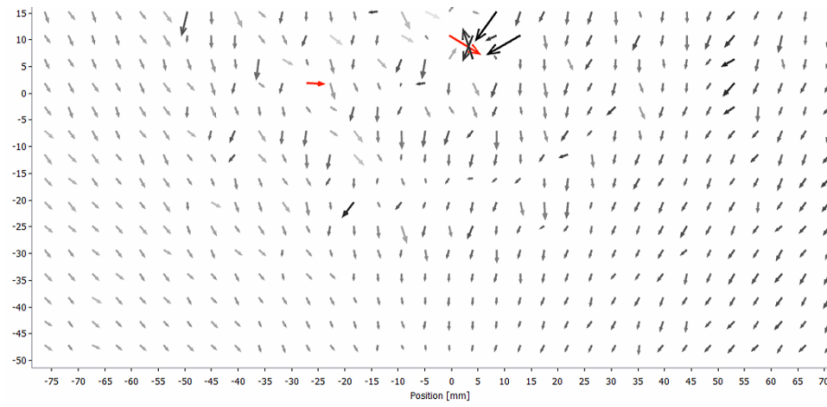


Figure A.3: Example of displacement vectors with background gradient

The plate structure was mounted to the top of the tank at around 27cm above the coating plate, so the only probable movement when a sufficiently strong force is applied in the streamwise direction is swinging backward while tilting forward, as was observed when pushing the plate with a finger. However, upon further examination of the vector field in Figure A.3, the arrows along both the upper and bottom edges of the field point downwards. This would suggest the plate moved downward which is not possible if the plate had swung backward. In addition, the arrows near the bottom edge of the plate have a magnitude smaller than the arrows in the corners at the top of the field of view (centre of the plate) where the downward displacement is not affected by the jet impact, which would not have been the case if the plate swung around the pivot point backward or forward. As shown in Figure A.4 where α and β are equal angles resulting from the potential swinging of the plate, due to geometry, a point near the bottom edge of the plate would appear to have a larger upwards movement (L_B) than a point near the top edge of the plate (L_A). All in all, the arrows point towards a movement where the plate moved backwards while tilting backward around the bottom edge, which is improbable.

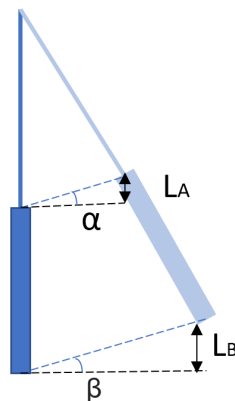


Figure A.4: Geometry of a plate swinging backward around a pivot point, α equals to β as the dot pattern can be assumed to be in the same plane as the aluminum structure, $L_B > L_A$

Although it is not possible to conclude what caused this phenomenon without further testing, what is certain is that the background gradient appears to vary from snapshot to snapshot as shown in Figure A.2. This seems to correspond to the unsteadiness of the jet. Another characteristic of the background gradient is that it worsens with increasing jet velocity, as the background gradient is more significant

for the higher jet velocity cases, as shown in Figure A.5. This points towards a physical phenomenon and corroborates the plate-movement hypothesis as for the high jet velocity cases, the jet is more likely to exert enough forces to cause a larger displacement of the coating plate.

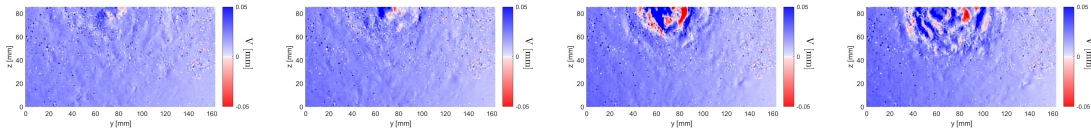


Figure A.5: Displacement fields showing the worsening of background gradient as the jet velocity is increased

Once the cause of this background gradient is proven in future experiments, it can be compensated for with a custom LINSUB algorithm that subtracts the linear fit of the displacement field to obtain the fluctuating signal only:

$$V = V - V_1(y, z), \quad (\text{A.2})$$

$$W = W - W_1(y, z), \quad (\text{A.3})$$

where $V_1(y, z)$ and $W_1(y, z)$ are the linear fits of the displacement fields.

It is assumed that this would not have an effect on the root-mean-square value of any of the key variables as the movement of the coating plate results in a mean change which manifests itself as a linear gradient across the y and z direction on the coating plate. This is made visible in Figure A.6, as the one-directional displacement field (V , W) along a horizontal/vertical line can be shown to be a linear trend plus fluctuations. After integration, the linear trend would appear as a parabolic shape in the surface topology, masking the wave structures caused by the pressure fluctuations. Therefore, it must be removed for accurate reconstruction of the coating surface. The linear trends can be extracted through a planar fit over the 2D horizontal and vertical displacement fields as shown in Figure A.6 and subtracted from the original displacement fields. After this subtraction (LINSUB), the background gradient has been removed without any impact on the fluctuations, as shown in Figure A.7.

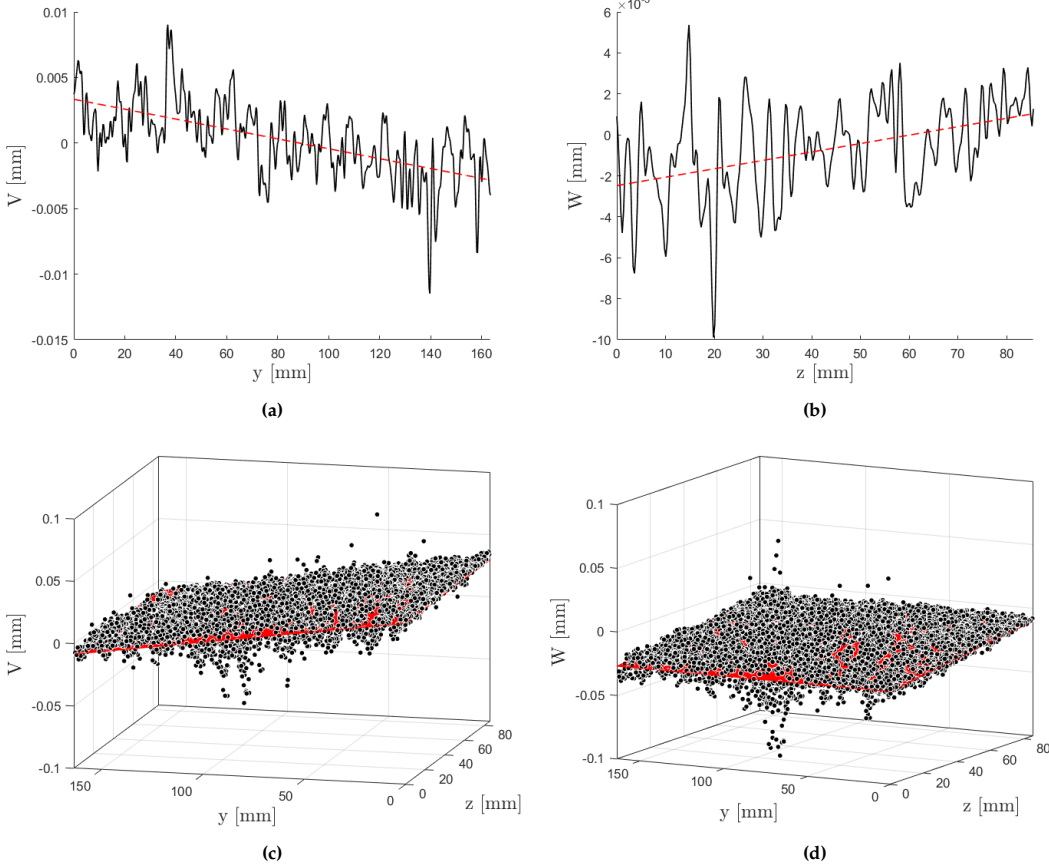


Figure A.6: Linear fit of one line of the a) horizontal and b) vertical displacement field and 2D linear plane fit of the c) horizontal and d) vertical displacement field

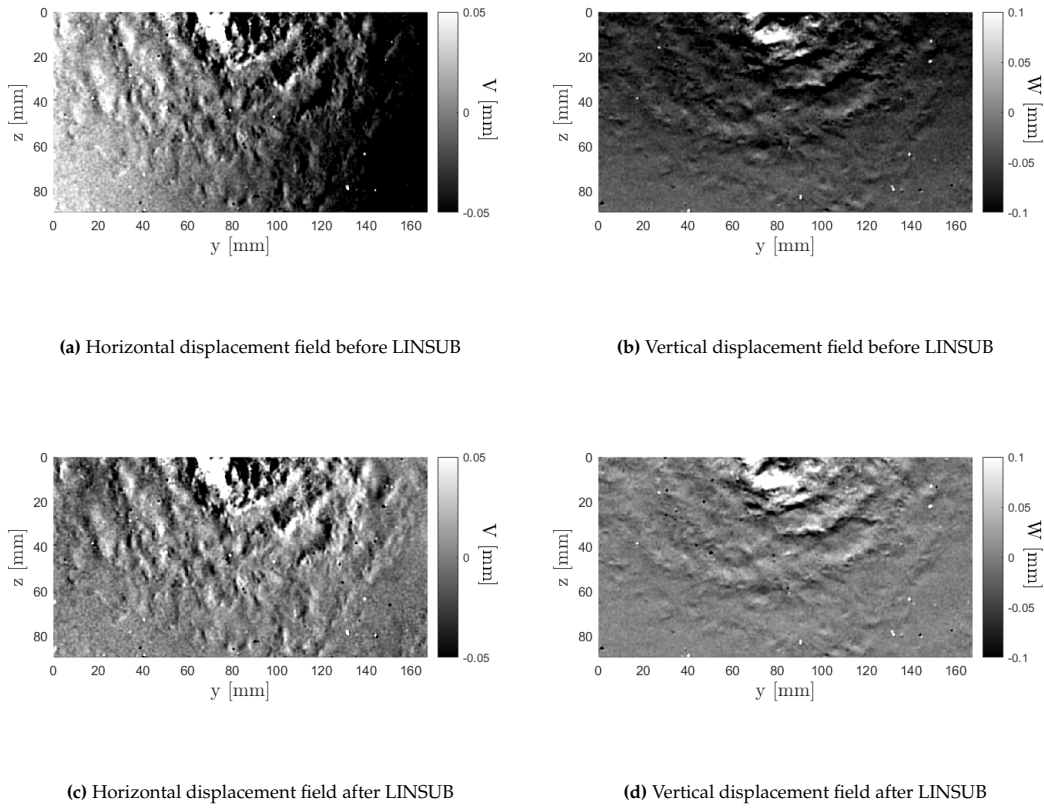


Figure A.7: Effect of the LINSUB operation

Ensemble mean subtraction (MSUB)

In some cases, the LINSUB operation reveals a background inhomogeneity in the displacement field that is constant with time, which interferes with the true displacement. This can be removed using the MSUB operation which subtracts the ensemble mean of all the snapshots from each individual snapshot:

$$V'_i = V_i - \frac{1}{N} \sum_{i=1}^N V_i, \quad (\text{A.4})$$

$$W'_i = W_i - \frac{1}{N} \sum_{i=1}^N W_i. \quad (\text{A.5})$$

This operation can only be performed when the background vector field does not vary significantly from snapshot to snapshot, for example, after LINSUB has already been applied. Otherwise, the ensemble mean could deviate significantly from the true background inhomogeneity, resulting in under-subtraction or over-subtraction. Figure A.8 demonstrates the effect of the LINSUB and MSUB operations when applied subsequently.

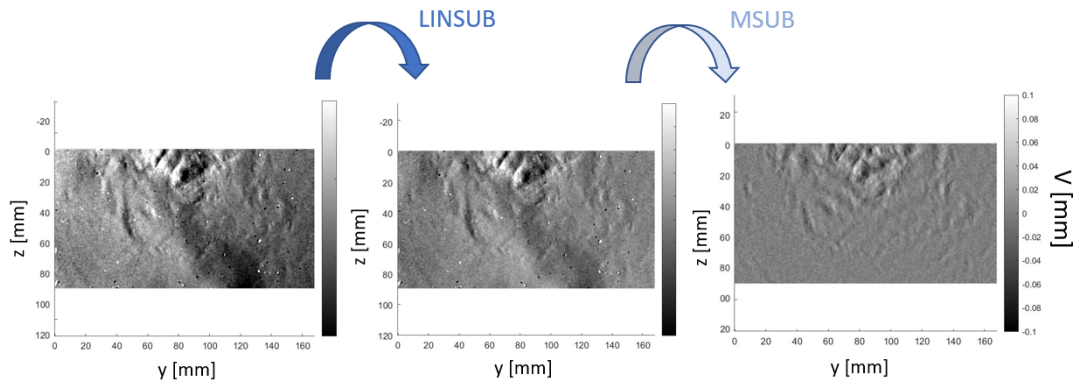


Figure A.8: Effect of subsequent LINSUB and MSUB operations

A.2. Pressure sensor calibration curves

Figure A.9 shows the pressure-voltage calibration curves of the sensors used and their linear fits.

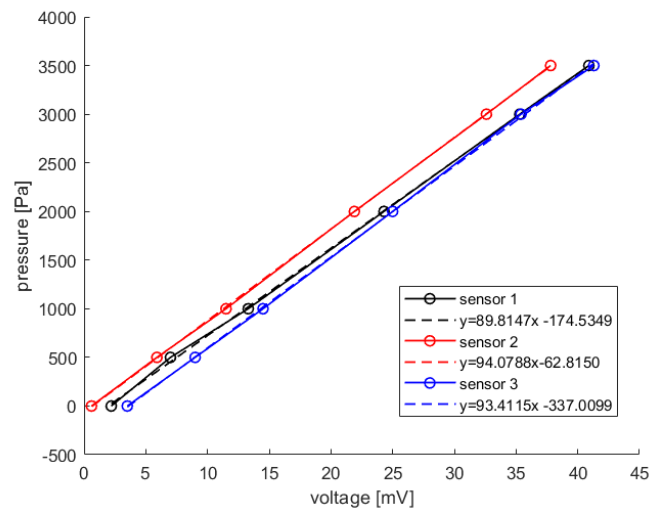


Figure A.9: Calibration curves of the pressure sensors, corresponded by colours

A.3. Frequency analysis

A dot product was performed on the subsequent displacement fields and a fast Fourier transform is then applied to extract the dominant frequencies.

The single-sided amplitude spectra for the horizontal and vertical displacement fields are shown in Figure A.10 and A.11, respectively. For the horizontal displacement fields, a fixed frequency component at around 4.5 Hz and 11.5 Hz are present in all cases. The amplitudes of the fixed frequency components show non-monotonic trends with increasing jet velocity. In addition, there is a dominant peak between 20 Hz to 25 Hz that reduces in frequency as the jet exit velocity is increased from $u_e = 3.41$ m/s to $u_e = 4.84$ m/s. However, this component also reduces steadily in frequency as the jet exit velocity is decreased from $u_e = 2.65$ m/s to $u_e = 2.19$ m/s. This component appears as a double peak with a

constant spacing of around 1Hz for all except the two cases with the highest jet velocities.

The fixed frequency components remain for the vertical displacement fields while the variant frequency component is no longer evident. An additional fixed frequency at 10 Hz appears for the vertical displacement fields.

Time-resolved data is required to correspond the peaks to coating structures with confidence.

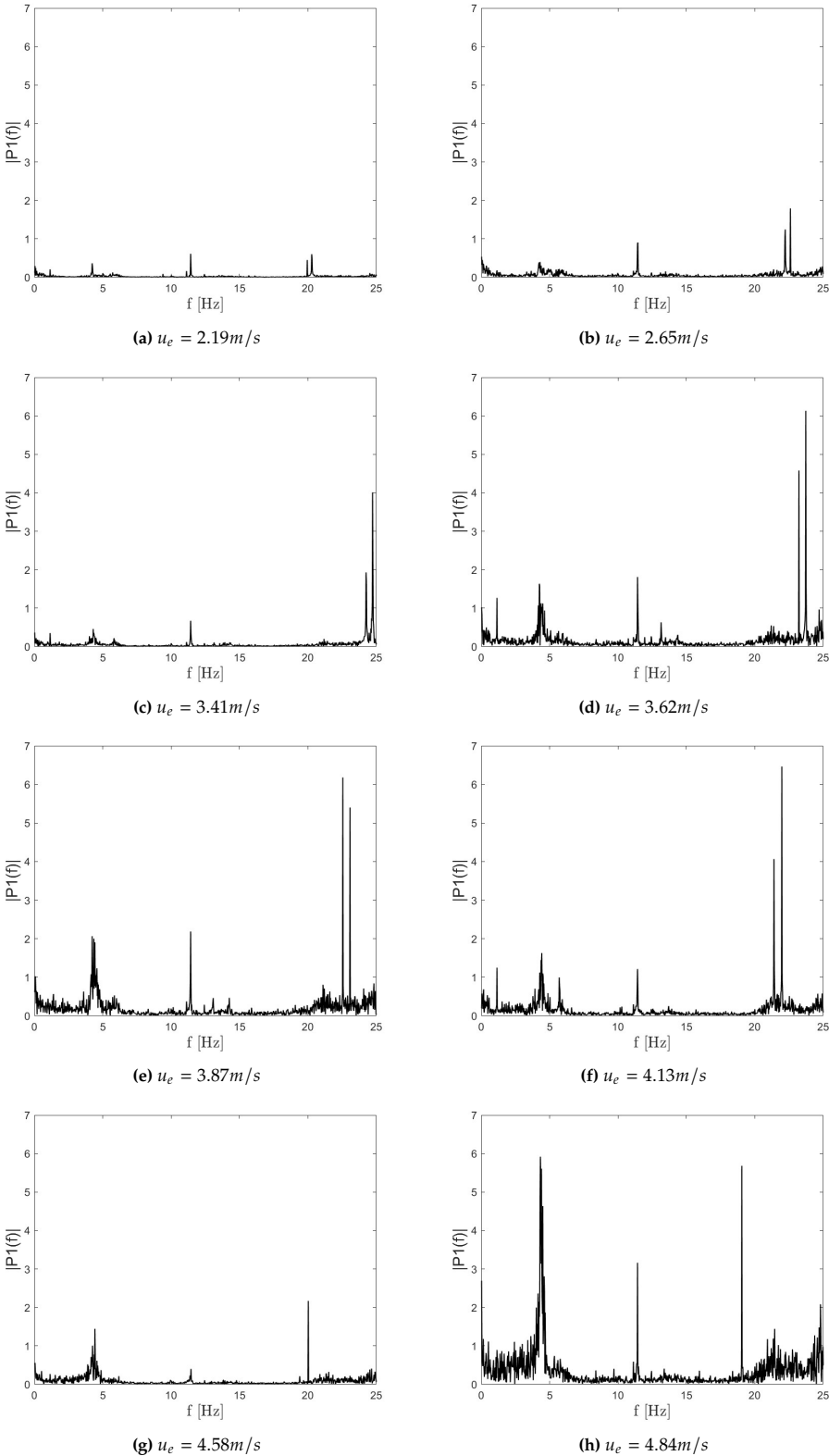


Figure A.10: Single-sided amplitude spectra of the horizontal displacement field V

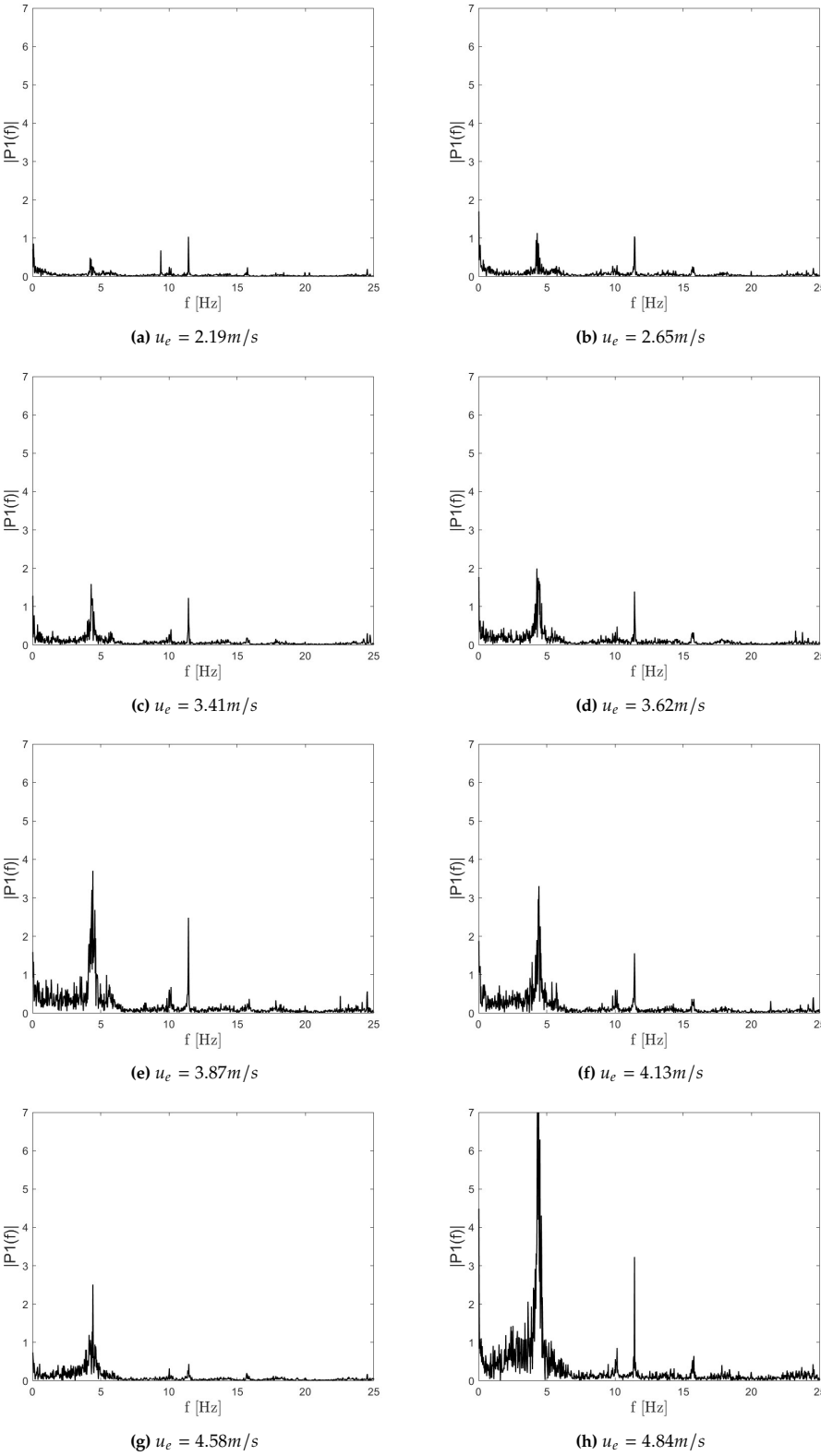


Figure A.11: Single-sided amplitude spectra of the vertical displacement field W

References

- [1] M. O. Kramer. "Boundary layer stabilization by distributed damping". In: *Journal of the American Society for Naval Engineers* 72.1 (1960), pp. 25–34. doi: 10.1111/j.1559-3584.1960.tb02356.x.
- [2] C. Zhang et al. "Deformation of a compliant wall in a turbulent channel flow". In: *Journal of Fluid Mechanics* 823 (2017), pp. 345–390. doi: 10.1017/jfm.2017.299.
- [3] A. J. Greidanus. "Turbulent shear flow over complex surfaces - An experimental study". PhD dissertation. TU Delft, 2020.
- [4] M. J. Morris et al. "Aerodynamic applications of pressure sensitive paint". In: *AIAA Journal* 31.3 (1993), pp. 419–425. doi: 10.2514/3.11346.
- [5] M. K. Quinn, L. Yang, and K. Kontis. "Pressure-Sensitive Paint: Effect of Substrate". In: *Sensors* 11.12 (2011), pp. 11649–11663. ISSN: 1424-8220. doi: 10.3390/s111211649.
- [6] B. W. van Oudheusden. "PIV-based pressure measurement". In: *Measurement Science and Technology* 24.3 (Jan. 2013), p. 032001. doi: 10.1088/0957-0233/24/3/032001.
- [7] M. Gad-El-Hak, R. F. Blackwelder, and J. J. Riley. "On the interaction of compliant coatings with boundary-layer flows". In: *Journal of Fluid Mechanics* 140 (1984), pp. 257–280. doi: 10.1017/S0022112084000598.
- [8] H. O. G. Benschop et al. "Deformation of a linear viscoelastic compliant coating in a turbulent flow". In: *Journal of Fluid Mechanics* 859 (2019), pp. 613–658. doi: 10.1017/jfm.2018.813.
- [9] M.O. Kramer. "The dolphin's secret". In: *J Am Soc Nav Engrs* 7 (1961), 73:103. doi: 10.1016/S0376-0421(01)00020-3.
- [10] F.W. Puryear. "Boundary layer control - drag reduction by use of compliant coatings". In: (1962).
- [11] M. Gad-el-Hak. "Compliant coatings for drag reduction". In: *Progress in Aerospace Sciences* 38 (Jan. 2002), pp. 77–99. doi: 10.1016/S0376-0421(01)00020-3.
- [12] P. W. Carpenter. "Status of Transition Delay Using Compliant Walls". In: *Viscous Drag Reduction in Boundary Layers*. 1990, pp. 79–113. doi: 10.2514/5.9781600865978.0079.0113.
- [13] P. W. Carpenter. "Current status of the use of wall compliance for laminar-flow control". In: *Experimental Thermal and Fluid Science* 16.1 (1998), pp. 133–140. ISSN: 0894-1777. doi: 10.1016/S0894-1777(97)10016-4.
- [14] Dennis M. Bushness, Jerry N. Hefner, and Robert L. Ash. "Effect of Compliant Wall Motion on Turbulent Boundary Layers". In: *Physics of Fluids* 20.10 (1977), S31–S48. doi: 10.1063/1.861756.
- [15] T.B. Benjamin. "Fluid flow with flexible boundaries". In: Görtler H. (eds) *Applied Mechanics*. Springer, 1966. doi: 10.1007/978-3-662-29364-5_11.
- [16] K.-S Choi et al. "Turbulent drag reduction using compliant surfaces". In: *Proceedings of The Royal Society A: Mathematical, Physical and Engineering Sciences* 453 (Oct. 1997), pp. 2229–2240. doi: 10.1098/rspa.1997.0119.

- [17] F. W. Boggs and E. R Hahn. "Performance of compliant skins in contact with high velocity flow in water". In: *Proceedings: Joint Army-Navy-Air Force Conference on Elastomer Research and Development*. 1962. Chap. 2.
- [18] O. O. Ivanov et al. "The influence of compliant coatings on skin friction in the turbulent boundary layer". In: *Journal of Physics: Conference Series* 894 (Oct. 2017), p. 012036. doi: 10.1088/1742-6596/894/1/012036.
- [19] J. H. Duncan. "The response of an incompressible, viscoelastic coating to pressure fluctuations in a turbulent boundary layer". In: *Journal of Fluid Mechanics* 171 (1986), pp. 339–363. doi: 10.1017/S0022112086001477.
- [20] P. R. Bandyopadhyay et al. "Experiments on the effects of aging on compliant coating drag reduction". In: *Physics of Fluids* 17.8 (2005), p. 085104. doi: 10.1063/1.2008997.
- [21] P. Krehl and S. Engemann. "August Toepler — The first who visualized shock waves". In: *Shock Waves* 5 (1995), pp. 1–18. doi: 10.1007/BF02425031.
- [22] G. S. Settles. "Toepler's Schlieren Technique". In: *Schlieren and Shadowgraph Techniques: Visualizing Phenomena in Transparent Media*. Berlin, Heidelberg: Springer Berlin Heidelberg, 2001, pp. 39–75. ISBN: 978-3-642-56640-0. doi: 10.1007/978-3-642-56640-0_3.
- [23] G. S. Settles. "Shadowgraph Techniques". In: *Schlieren and Shadowgraph Techniques: Visualizing Phenomena in Transparent Media*. Berlin, Heidelberg: Springer Berlin Heidelberg, 2001, pp. 143–163. ISBN: 978-3-642-56640-0. doi: 10.1007/978-3-642-56640-0_6.
- [24] S. Dalziel, G. Hughes, and B. Sutherland. "Whole-field density measurements by 'synthetic schlieren'". In: *Experiments in Fluids* 28 (Jan. 2000), pp. 322–335. doi: 10.1007/s003480050391.
- [25] F. Klinge and M. L. Riethmuller. "Local density information obtained by means of the Background Oriented Schlieren(BOS) method". In: 2002.
- [26] M. Raffel. "Background-oriented schlieren (BOS) techniques". In: *Experiments in Fluids* 56 (Mar. 2015), pp. 1–17. doi: 10.1007/s00348-015-1927-5.
- [27] G. E. Elsinga et al. "Assessment and Application of Quantitative Schlieren Methods: Calibrated Color Schlieren and Background Oriented Schlieren". In: *Experiments in Fluids* 36 (Feb. 2004), pp. 309–325. doi: 10.1007/s00348-003-0724-8.
- [28] J. Kurata et al. "Water surface measurement in a shallow channel using the transmitted image of a grating". In: *Review of Scientific Instruments* 61.2 (1990), pp. 736–739. doi: 10.1063/1.1141487. eprint: <https://doi.org/10.1063/1.1141487>.
- [29] F. Moisy, M. Rabaud, and K. Salsac. "A synthetic Schlieren method for the measurement of the topography of a liquid interface". In: *Experiments in Fluids* 46 (June 2009), pp. 1021–1036. doi: 10.1007/s00348-008-0608-z.
- [30] M. Raffel et al. *Particle Image Velocimetry: A Practical Guide*. Jan. 2007. ISBN: 978-3-540-72307-3. doi: 10.1007/978-3-540-72308-0.
- [31] F. T. Charruault et al. "A dot tracking algorithm to measure free surface deformations". In: 2018.
- [32] Shiyong Yao et al. "An experimental study of a turbulent jet impinging on a flat surface". In: *International Journal of Heat and Mass Transfer* 83 (Apr. 2015), pp. 820–832. doi: 10.1016/j.ijheatmasstransfer.2014.12.026.
- [33] Benoit Cushman-Roisin. *Environmental Fluid Mechanics*. Jan. 2013.
- [34] F. Moisy. *Random dot pattern for Synthetic Schlieren or Background-Oriented Schlieren*. <http://www.fast.u-psud.fr/~moisy/ml/misc/makebospattern.m>. 2008.

-
- [35] C. Kähler, C. Cierpka, and S. Scharnowski. “On the uncertainty of digital PIV and PTV near walls”. In: *Experiments in Fluids* 52 (June 2012), pp. 1641–1656. DOI: [10.1007/s00348-012-1307-3](https://doi.org/10.1007/s00348-012-1307-3).